Design and Optimization of Optical Devices Using Artificial Intelligence Techniques

Seyedmohammad Mirjalili

A Thesis

In the Department

of

Electrical and Computer Engineering

Presented in Partial Fulfillment of the Requirements

For the Degree of

Doctor of Philosophy (Electrical and Computer Engineering) at

Concordia University

Montreal, Quebec, Canada

June 2021

CONCORDIA UNIVERSITY
SCHOOL OF GRADUATE STUDIES

This is to certify that the thesis prepared

By: Seyedmohammad Mirjalili

Entitled: Design and Optimization of Optical Devices Using Artificial Intelligence Techniques

and submitted in partial fulfillment of the requirements for the degree of

Doctor Of Philosophy (Electrical and Computer Engineering)

complies with the regulations of the University and meets the accepted standards with respect to originality and quality.

Signed by the final examining committee:

Dr. Gosta Grahne	Chair
Dr. Bora Ung	External Examiner
Dr. Arash Mohammadi	External to Program
Dr. Yousef R. Shayan	Examiner
Dr. Steve Shih	Examiner
Dr. M Zahangir Kabir	Thesis Supervisor (s)
Dr. Pablo Bianucci	

Approved by

Dr. Wei-Ping Zhu, Graduate Program Director

August 17, 2021

Date of Defence

Dr. Mourad Debbabi, Dean of Gina Cody School of Engineering and Computer Science

Abstract

Design and Optimization of Optical Devices Using Artificial Intelligence Techniques

Seyedmohammad Mirjalili, Ph.D.

Concordia University, 2021

Over the last decade, there has been a growing interest in utilizing novel photonic and optical devices for a diverse range of applications. For the next generation of wireless communication networks, the development of new and optimal optical devices is inevitable. Existing optical network infrastructure cannot meet the stringent requirements of next-generation data networks (such as a 1000-fold increase in bandwidth demand, very low latency, better spectral and energy efficiency, etc.). In other words, the physical layer of the communication network must be revolutionized to provide the proper foundation for these emerging technologies.

Optical networks are based on propagating light. Light propagation in realistic settings is usually a complicated phenomenon. When it comes to the context of optical devices and its propagation in the new devices, the complexity of the problem becomes much higher. In other words, the relations between the light propagation characteristics and the structural parameters of the new devices are mostly unknown. Therefore, the conventional method for designing such devices in the absence of a clear analytic description is usually based on a trial and error process. This method has many disadvantages, being time-consuming, inefficient, and the designed device is usually far from an optimized one. Also, the designing process needs intensive human involvement.

Therefore, to fill this gap, we have utilized artificial intelligence (AI) techniques to design, analyze, and optimize several different optical devices. More specifically, we have proposed several optimization frameworks for designing orbital angular momentum (OAM) fibers, large mode area photonic crystal (PhC) fibers, waveguide-based LP_{01} to LP_{0m} mode converter, PhC filters, PhC sensors, and PhC-enhanced light-emitting diodes (LEDs). In all of these devices, we are dealing with a complicated system in which the relationships between the structural parameters and the output performance merit factors are very complicated. Such problems have a long simulation runtime, so it is not viable to employ an exhaustive optimization algorithm, which evaluates all of the possible combinations of the parameters to find the optimal one. Therefore, we consider our problem as a black box and use the AI optimization algorithm to find the optimal solution. Eventually, the proposed optimization frameworks open up an effective way to design high-performance optical devices for a diverse range of applications and pave the way for the development of next-generation optical devices for next-generation optical networks.

Acknowledgments

I would like to express my gratitude and appreciation to my supervisors Dr. M Zahangir Kabir and Dr. Pablo Bianucci. This dissertation would have been impossible without their guidance, continuous support, and encouragement throughout my studies and research. Also, I cannot be thankful enough to my colleagues, family, friends, and those who contributed to the successful completion of my studies at Concordia University. My research was supported by the Natural Sciences and Engineering Research Council of Canada (NSERC), the B2X Doctoral Research fellowship from the Fonds de Recherche du Québec - Nature et Technologies (FRQNT), the NSERC CREATE training program in Pervasive and Smart Wireless Applications for the Digital Economy (PERSWADE) program, Concordia University Public Scholars program, and Doctoral Fellowship from Gina Cody School of Engineering and Computer Science.

Detail on Author Contributions

Several chapters of the thesis are based on published articles. A description of the contribution of each author is given here.

Chapter 4 [1]: Design optimization of OAM fibers using the grey wolf optimizer

SM Mirjalili: Conceptualization, Methodology, Software, Writing, Visualization. **H Taleb:** Methodology. **MZ Kabir:** Supervision. **P Bianucci:** Methodology, Writing, Supervision.

Chapter 5 [2]: Optimization Frameworks for Designing Photonic Crystal Filters

SM Mirjalili: Conceptualization, Methodology, Software, Writing, Visualization. **B Merikhi:** Methodology, Visualization. **SZ Mirjalili:** Methodology, Writing. **M Zoghi:** Methodology, Visualization. **S Mirjalili:** Conceptualization, Methodology, Supervision.

Chapter 6 [3]: Radiation Pattern Design of Photonic Crystal LED optimized by using Multi-objective Grey Wolf Optimizer

B Merikhi: Methodology, Software, Writing. **SM Mirjalili:** Conceptualization, Methodology, Software, Writing, Visualization. **M Zoghi:** Methodology, Visualization. **SZ Mirjalili:** Methodology, Writing. **S Mirjalili:** Conceptualization, Methodology, Supervision.

Appendix A [4]: Optimal Design of Large Mode Area Photonic Crystal Fibers Using The Multi objective Gray Wolf Optimization Technique

K Rashidi: Conceptualization, Methodology, Software, Writing, Visualization. **SM Mirjalili:** Conceptualization, Methodology, Software, Writing, Visualization. **H Taleb:** Conceptualization, Methodology, Supervision. **D Fathi:** Conceptualization, Methodology, Supervision.

Appendix B [5]: Design Optimization of a Waveguide-Based LP_{01} to LP_{0m} Mode Converter

H Mellah: Conceptualization, Methodology, Software, Writing, Visualization. **SM Mirjalili:** Conceptualization, Methodology, Software, Writing, Visualization. **X Zhang:** Supervision.

Appendix C [6]: Optimization Framework for Designing Photonic Crystal Sensors

MJ Safdari: Methodology, Software, Writing. **SM Mirjalili:** Conceptualization, Methodology, Software, Writing, Visualization. **P Bianucci:** Conceptualization, Writing, Supervision. **X Zhang:** Supervision.

Table of Content

List of Figures

List of Tables

List of Abbreviations

AI	Artificial intelligence
BER	Bit-Error-Rate
CM	Constraint Module
EMA	Effective Mode Area
ER	Extraction Ratio
FDTD	Finite-Difference Time-Domain
FEM	Finite Element Method
FM	Fundamental Mode
FMF	Few-Mode Fiber
GA	Genetic Algorithm
GWO	Gray Wolf Optimizer
HOM	Higher-Order Mode
IL	Insertion Loss
LCF	Leakage Channel Fiber
LCP	Left Circularly Polarized
LED	Light-Emitting Diode
LMA	Large Mode Area
LP	Linearly Polarized
MDM	Mode-Division Multiplexing
MIMO	Multiple-Input-Multiple-Output
MMF	Multi-Mode Fiber
MMI	Multimode Interference
MOPSO	Multi-Objective Particle Swarm Optimization
MSSA	Multi-objective Salp Swarm Algorithm
NA	Numerical Aperture
NFL	No-Free-Lunch
OAM	Orbital Angular Momentum
OM	Optimizer Module
PCF	Photonic Crystal Fiber
PEC	Perfect Electric Conductor
PF	Purcell Factor
PhC	Photonic Crystal
PLC	Planar Lightwave Circuits
PM	Parameter Module
PML	Perfectly Matched Layer
PP	Polarization Purity
PPF	Polarization Purity Factor
PSO	Particle Swarm Optimization
PWE	Plane Wave Expansion
Q	Quality factor
RCF	Ring Core Fiber
RCP	Right Circularly Polarized

SDM	Space Division Multiplexing
SMF	Single Mode Fiber
SOI	Silicon-On-Insulator
SSA	Salp Swarm Algorithm
TDM	Time-Division Multiplexing
TE	Transverse Electric
TM	Transverse Magnetic
WDM	Wavelength-Division Multiplexing

Chapter 1: Introduction

1.1 Problem statement and motivation of the research

During the last decade, there has been a growing interest in utilizing novel photonic and optical devices for a diverse range of applications. As a general statement, light propagation is usually considered as a complicated phenomenon. When it comes to the context of its propagation in optical devices, the complexity of the problem becomes much higher. More specifically, the relations between the light propagation characteristics and the structural parameters of the new devices cannot be expressed analytically. Therefore, to fill this gap, we have proposed several frameworks, which do not require a priori knowledge of the light propagation in a device, to design, analyze, and optimize a couple of optical devices.

1.2 The methodology

Due to the complex interplay between light and matter in optical devices with dimensions of a few wavelengths of light, finding an analytical equation that describes the relationship between the structural parameters and the device output performance is usually very challenging and requires many simplifications. Therefore, the conventional method for designing such devices in the absence of a clear analytic description is usually based on a trial and error process. This method has many disadvantages, being time-consuming, inefficient (as the designed device is usually far from an optimized one), and the design process needs intensive human involvement.

An alternative method for designing such devices is to utilize Artificial intelligence (AI) techniques to compensate for the lack of analytical equations. The first step is to formulate the device design process in a way that is amenable for an optimizer. The second step is utilizing an AI-based optimizer to find the optimum designs. This method intelligently encompasses the process of finding the relationship between the structural parameters and the device outputs.

Most real-world problems, including the problems considered in this thesis, have a large number of difficulties, which makes finding analytical solutions for them very challenging. Such problems are also costly (have long simulation runtime), so it is not viable to employ an exhaustive optimization algorithm, which evaluates all of the possible combinations of the parameters to find the optimal one. The literature shows that heuristics are reliable tools in this situation because they find a reasonably good solution in a reasonable time. One issue with them is that they are stochastic and require specific heuristic information for different problems. Meta-heuristics have been proposed to alleviate this drawback and ensure that we can consider our problem as a black box and use the optimization algorithm to find the optimal solution.

It is worth mentioning here that meta-heuristic optimization techniques belong to the family of stochastic approaches and benefit from a number of advantages including simplicity, flexibility, and inexpensive computational cost as compared to deterministic approaches. These advantages make them highly suitable for real-world engineering design problems, including the problems investigated in this thesis.

Another difficulty that comes up again and again in engineering design problems is multi-objectivity. There are usually multiple, often conflicting, objectives in real-world problems, so applying a multi-objective formulation allows for exploration of the behavior of the problems across a range of design parameters and operating conditions.

Another key concept in the optimization of real-world problems is robustness. Robust

optimization deals with finding the optimal designs that are not sensitive to probable uncertainties. Among different types of uncertainties, perturbations in the design parameters can be considered as the most common ones in engineering problems. In this type, the design parameters might fluctuate after the determination of the optimal solution(s), mostly due to the imprecisions of the manufacturing process. The presence of uncertainties, obviously, increases the difficulty of optimization problems.

1.3 Areas where optical device optimization can be applied

1.3.1 Optical data communication

Time-division multiplexing (TDM) and wavelength-division multiplexing (WDM) are two mature technologies which are used in current fiber-optic communication systems. TDM is a technique where optical channels are combined, transmitted together, and separated again based on different arrival times. WDM multiplexes a number of optical channels onto a single optical fiber by using different wavelengths of laser light. These techniques enable bidirectional communications over a strand of fiber and multiplication of capacity. Similarly, multiplexing multiple orthogonal fiber modes enables high-capacity optical communication. This technique is known as mode-division multiplexing (MDM). Therefore, the future of fiber-optic communication systems will be based on a mixture of TDM, WDM, and MDM.

Specifically, for the next generation of wireless communication networks (like 5G and 6G) and beyond, the development of new and optimal optical devices is of great importance. In other words, the physical layer of the communication network should be improved and revolutionized to provide the proper foundation for these emerging technologies [7]. The existing network infrastructure should evolve to meet the stringent requirements of next-generation of data communication networks such as the explosive growth of 1000 times in bandwidth demand, very low latency of a few ms, ten times growth in spectral efficiency, energy efficiency, etc., [8]. Recently, data transmission based on the orbital angular momentum (OAM) of light has been proposed to increase the capacity of optical fibers [1], [9], [10] A light beam that carries the OAM is also known as twisted light.

Although space division multiplexing (SDM) is an alternative technology that offers an opportunity to multiply the carrying capacity of the optical fiber, in the case of OAM modes, the capacity increase can be accomplished without the added burden of complex multiple-input-multiple-output (MIMO) digital signal processing. In order to take advantage of OAM, a new set of optical components such as the OAM beam generators, fibers, multiplexers, demultiplexers, etc., are needed. These components should be available as commercial products rather than just to be tested in scientific laboratories.

The need for simpler MIMO processing in the receiver of data communication based on OAM modes enables information transmission in optical communications with a high capacity. Generation of OAM modes, modulation of OAM modes, the transmission of OAM modes with minimal dispersion, and detection and demultiplexing of OAM mode are all timely topics in the field of optical MDM.

Research into twisted light has suggested that light waves could carry huge quantities of data through optical fibers. According to preliminary tests, this technology has proven a capacity to transfer up to 2.5 terabits of data per second which is equal to 66 DVDs or 320 Gigabytes per second [11]. On the other hand, research into twisted wave multiplexing in the radio and millimeter wavelengths has been shown that a data communication speed of 32 gigabits per

second can be achieved over the air [12]. Recently, the Nippon Telegraph and Telephone Corporation (NTT) has successfully demonstrated the world's first 100Gbps wireless transmission using this technology that already surpasses the upcoming 5G wireless communication standard [13].

1.3.2 Photonic Crystal (PhC) devices

A photonic crystal (PhC) is a structure with a spatially periodic refractive index. PhC structures show bandgaps in their spectral transmission performance. By creating defects in the PhC lattice, some leaky modes will be generated in the bandgap region. In other words, these leaky modes provide the opportunity to manipulate the transmitted light [14]. To date, Photonic Crystal devices have become popular because they cover a wide range of applications.

The use of a leaky mode to implement optical filters is one of the most standard applications of PhC structures. This leaky mode provides a very narrow bandpass filter that could be used in a wide range of applications. In this thesis, we examined PhC fibers, PhC filters, PhC sensors, and PhC-enhanced light-emitting diodes (LEDs).

The main problem inherent with the use of such devices is how to model the internal propagation of light. In other words, finding an analytical equation describing the relationship between the structural parameters and the device output performance is usually very challenging, and in many cases it is impossible. The complexity of the relationship between the structural parameters and the device output performance prevents researchers from proposing analytic methods to design such devices.

1.4 Research Objectives

In this thesis, we aim to investigate the design process of a number of different optical devices. After that, we formulate the design process in a way that the problem is considered as a black-box and then we use an AI optimization algorithm to find the optimal solution(s). The optical devices which are examined in this thesis are as follows:

- Orbital angular momentum (OAM) fibers
- PhC filters
- PhC-enhanced light-emitting diodes (LEDs)
- Large mode area photonic crystal (PhC) fibers
- Waveguide-based LP_{01} to LP_{0m} mode converter
- PhC sensors

1.5 Organization of thesis

In chapter 2, we explain the basic concepts of electromagnetism and the role of AI algorithms in device design optimization. In the next chapter, two well-known nature-inspired AI optimizers called Gray Wolf Optimizer (GWO) and Salp Swarm Algorithm (SSA) are explained. In chapters 4 to 6 and appendixes A to C, we provide frameworks for design optimization of OAM fibers, PhC filters, PhC-enhanced light-emitting diodes (LEDs), large mode area PhC fibers, waveguide-based LP_{01} to LP_{0m} mode converter, PhC sensors. Eventually, chapter 7 concludes the thesis and provides some topics for future works.

Chapter 2: Background

2.1 Basic concepts of electromagnetism

In order to simulate the propagation of light in optical devices, we start with Maxwell's equations. These sets of equations govern almost all the light propagation behaviors in both free space and dielectric waveguides. In 1870, James Maxwell proposed them and we can see that they became one of the most significant foundations of science in our modern world [15]. With the combination of Gauss's law, Faraday's law, and Ampere's circuit law, Maxwell's equations are written as a set of linear partial differential equations as follows:

$$\begin{aligned} \nabla \cdot \mathbf{D} &= \rho, \\ \nabla \cdot \mathbf{B} &= 0, \\ \nabla \times \mathbf{E} &= -\frac{\partial \mathbf{B}}{\partial t}, \\ \nabla \times \mathbf{H} &= \mathbf{J_c} + \frac{\partial \mathbf{D}}{\partial t} \end{aligned} \tag{2-1}$$

Where **H** is the magnetic field, **E** is the electric field, **B** is magnetic flux density, and **D** is the electric displacement field. ρ and $\mathbf{J_c}$ represent the free charge and current density in the medium. The symbols ∇· and ∇× indicate the divergence and the curl operator, respectively. In this thesis, we will be working on structures made with dielectric materials and no free charges or currents. Therefore, ρ=0 and $\mathbf{J_c}$=0.

In addition, the electric (magnetic) and electric displacement (magnetic flux density) fields are connected through the constitutive relations that can be expressed as follows:

$$\begin{aligned} \mathbf{D} &= \varepsilon_0 \varepsilon_r \mathbf{E} = \varepsilon \mathbf{E} \\ \mathbf{B} &= \mu_0 \mu_r \mathbf{H} = \mu \mathbf{H} \end{aligned} \tag{2-2}$$

In these relations, ε_0 and μ_0 are the electric permittivity and magnetic permeability of free space. They are related to the speed of light in vacuum as $c_0 = 1/\sqrt{\mu_0 \varepsilon_0} = 2.998 \times 10^8\ [m/s]$. The parameters ε_r and μ_r are the relative permittivity and relative permeability of the material, both of which characterize the linear electro-magnetic properties of the medium. We have μ_r=1 for non-magnetic materials. ε_r is a scalar for isotropic materials. In this case, $\varepsilon_r = n^2$, where n is the refractive index of the material.

2.1.1 Wave equations

Applying the curl operator to the last two Maxwell's equations and considering the identity $\nabla \times \nabla \times \boldsymbol{E} \equiv \nabla \cdot (\nabla \cdot \boldsymbol{E}) - \nabla^2 \boldsymbol{E}$, where ∇·**E**=0, the desired wave equation for a current- and charge-free homogeneous medium takes the following form [16].

$$\begin{aligned} \left(\nabla^2 - \mu\varepsilon \frac{\partial^2}{\partial t^2}\right)\mathbf{E} = 0 \\ \left(\nabla^2 - \mu\varepsilon \frac{\partial^2}{\partial t^2}\right)\mathbf{H} = 0 \end{aligned} \tag{2-3}$$

The same derivation can be obtained for the magnetic field H, and thus we can arrive to the second equation. In a Cartesian coordinate system, the Laplace operator takes the form of $\nabla^2 = \partial_x^2 + \partial_y^2 + \partial_z^2$. Using the time-harmonic ansatz $e^{-i\omega t}$ for the electromagnetic field, wave equations can be written compactly as follows:

$$\begin{aligned}(\nabla^2 + k_0^2 n^2)\mathbf{E} &= 0 \\ (\nabla^2 + k_0^2 n^2)\mathbf{H} &= 0\end{aligned} \tag{2-4}$$

where ω is the angular frequency and $k_0 = \omega/c_0$ is the wavenumber in a vacuum. These equations are called Helmholtz equations as well [17]. Given the spatial distribution of the refractive index of a given device, the behaviour of classical electromagnetic waves in it can be described by solving these equations.

2.2 The role of AI algorithms in device design optimization

We define optimization of device design as finding the values for the device structural parameters (typically physical dimensions, but these could also include other parameters such as refractive indices), which result in the best output performance. Most of the time we do not know the relation between the structural parameters and device output performance, so we cannot do an analytic analysis of the device performance to optimize it. A simple way to optimize the design is a trial-and-error approach to find a high-performance device design. While this may result in acceptable performance, it does not guarantee that there are better possible values for the parameters. Another method is to sweep the whole parameter search space to find the best design(s). Usually, optical devices have many structural parameters and vast search spaces. The number of possible combinations of the parameters is huge, so a very large number of simulations is required. Thus, even if a simulation takes a small amount of time to run, the required time to perform the whole search becomes unsurmountable. The proposed method for solving this problem is to utilize AI algorithms to find the best value for the structural parameters. These algorithms give us a way to find optimized designs reducing the number of required simulations. More specifically, metaheuristics algorithms such as Particle Swarm Optimization (PSO) [18], [19], Genetic Algorithm (GA) [20], Grey Wolf Optimizer (GWO) [21], Salp Swarm Algorithm (SSA) [22], and so on are highly suitable to be used. These algorithms consider the problem of device design as a black box (objective function) and try to find the maximum or minimum of the output merit factor(s). The maximum or minimum of the objective function corresponds to the best device design. Therefore, with a much smaller number of simulations, affordable with current processors, the best design(s) can be found. A flowchart of how an AI algorithm solves the problem of finding the best value for the structural parameters is shown in Figure 2-1.

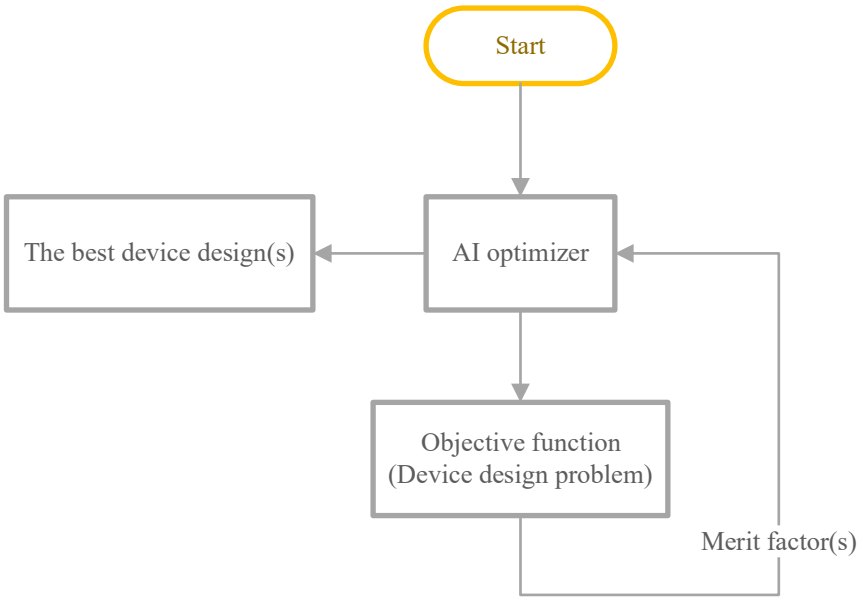

Figure 2-1: Flowchart of how an AI algorithm solves the problem of finding the best value for the structural parameters.

The source codes of a wide range of metaheuristics optimization algorithms that have been developed by us are publicly available in [23]. In the next chapter, as examples, Gray Wolf Optimizer (GWO) [21], [24] and Salp Swarm Algorithm (SSA) [22] are explained to show how metaheuristics optimization algorithms solve the problem of optical devices design.

Chapter 3: Nature-Inspired Optimizers

3.1 Gray Wolf Optimizer (GWO)

In this section, the inspiration of the GWO is first discussed. Then, the mathematical model is provided. This section is based on the paper published in the Journal of Advances in Engineering Software [21].

3.1.1 3.1. Inspiration

The Grey wolf (Canis lupus) belongs to the Canidae family. Grey wolves are considered apex predators, meaning that they are at the top of the food chain. Grey wolves mostly prefer to live in a pack. The group size is 5-12 on average. Of particular interest is that they have a very strict social dominance hierarchy, as shown in Figure 3-1.

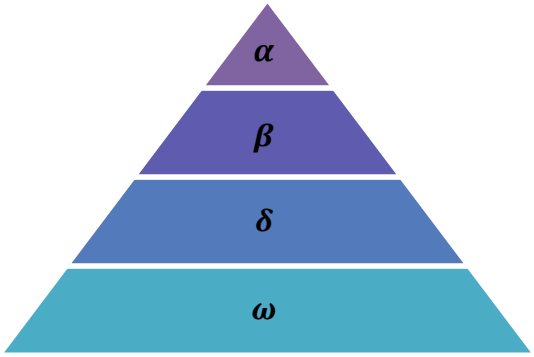

Figure 3-1 Hierarchy of grey wolf (dominance decreases from top-down)

The leaders are a male and a female, called alphas. The alpha is mostly responsible for making decisions about hunting, sleeping place, time to wake, and so on. The alpha's decisions are dictated to the pack. However, some kind of democratic behavior has also been observed, in which an alpha follows the other wolves in the pack. In gatherings, the entire pack acknowledges the alpha by holding their tails down. The alpha wolf is also called the dominant wolf since his/her orders should be followed by the pack [25]. The alpha wolves are only allowed to mate in the pack. Interestingly, the alpha is not necessarily the strongest member of the pack but the best in terms of managing the pack. This shows that the organization and discipline of a pack is much more important than its strength.

The second level in the hierarchy of grey wolves is beta. The betas are subordinate wolves that help the alpha in decision-making or other pack activities. The beta wolf can be either male or female, and he/she is probably the best candidate to be the alpha in case one of the alpha wolves passes away or becomes very old. The beta wolf should respect the alpha but commands the other lower-level wolves as well. It plays the role of an advisor to the alpha and discipliner for the pack. The beta reinforces the alpha's commands throughout the pack and gives feedback to the alpha.

The lowest ranking grey wolf is the omega. The omega plays the role of scapegoat. Omega wolves always have to submit to all the other dominant wolves. They are the last wolves that are allowed to eat. It may seem the omega is not an important individual in the pack, but it has been observed that the whole pack faces internal fighting and problems in case of losing the omega. This is due to the venting of violence and frustration of all wolves by the omega(s). This assists in satisfying the entire pack and maintaining the dominance structure. In some cases, the omega

is also the babysitter in the pack.

If a wolf is not an alpha, beta, or omega, he/she is called subordinate (or delta in some references). Delta wolves have to submit to alphas and betas, but they dominate the omega. Scouts, sentinels, elders, hunters, and caretakers belong to this category. Scouts are responsible for watching the boundaries of the territory and warning the pack in case of any danger. Sentinels protect and guarantee the safety of the pack. Elders are the experienced wolves who used to be alpha or beta. Hunters help the alphas and betas when hunting prey and providing food for the pack. Finally, the caretakers are responsible for caring for the weak, ill, and wounded wolves in the pack.

In addition to the social hierarchy of wolves, group hunting is another interesting social behavior of grey wolves. According to Muro *et al.* [26], the main phases of gray wolf hunting are as follows:

- Tracking, chasing and approaching the prey
- Pursuing, encircling, and harassing the prey until it stops moving
- Attack towards the prey

These steps are shown in Figure 3-2.

Figure 3-2 Hunting behavior of grey wolves: (A) chasing, approaching, and tracking prey (B-D) pursuing, harassing, and encircling (E) stationary situation and attack [26].

This hunting technique and the social hierarchy of grey wolves are mathematically modeled in order to design GWO and perform optimization.

3.1.2 Mathematical model and algorithm

In this subsection, the mathematical models of the social hierarchy, tracking, encircling, and attacking prey are provided. Then the GWO algorithm is outlined.

Social hierarchy:

In order to mathematically model the social hierarchy of wolves when designing GWO, we consider the fittest solution as the alpha (α). Consequently, the second and third-best solutions are named beta (β) and delta (δ), respectively. The rest of the candidate solutions are assumed to be omega (ω). In the GWO algorithm, the hunting (optimization) is guided by α, β, and δ. The ω wolves follow these three wolves.

Encircling pray:

As mentioned above, grey wolves encircle prey during the hunt. In order to mathematically model encircling behavior, the following equations are proposed:

$$\vec{D} = |\vec{C}.\overrightarrow{X_p}(t) - \vec{X}(t)| \tag{3-1}$$

$$\vec{X}(t+1) = \overrightarrow{X_p}(t) - \vec{A}.\vec{D} \tag{3-2}$$

where t indicates the current iteration, $\vec{A}$ and $\vec{C}$ are coefficient vectors, $\overrightarrow{X_p}$ is the position vector of the prey, and $\vec{X}$ indicates the position vector of a grey wolf.

The vectors $\vec{A}$ and $\vec{C}$ are calculated as follows:

$$\vec{A}= 2\vec{a}.\overrightarrow{r_1}- \vec{a} \tag{3-3}$$

$$\vec{C} = 2.\overrightarrow{r_2} \tag{3-4}$$

Where components of $\vec{a}$ are linearly decreased from 2 to 0 over the course of iterations and r_1, r_2 are random vectors in [0,1].

To see the effects of equations (3-1) and (3-2), a two-dimensional position vector and some of the possible neighbors are illustrated in Figure 3-3 (a). As can be seen in this figure, a grey wolf in the position of (X,Y) can update its position according to the position of the prey (X*, Y*). Different places around the best agent can be reached with respect to the current position by adjusting the value of $\vec{A}$ and $\vec{C}$ vectors. For instance, (X*-X, Y*) can be reached by setting $\vec{A} = (1,0)$ and $\vec{C} = (1,1)$. The possible updated positions of a grey wolf in 3D space are depicted in Figure 3-3 (b). Note that the random vectors r_1 and r_2 allow wolves to reach any position between the points illustrated in Figure 3-3. So a grey wolf can update its position inside the space around the prey in any random location by using equations (3-1) and (3-2).

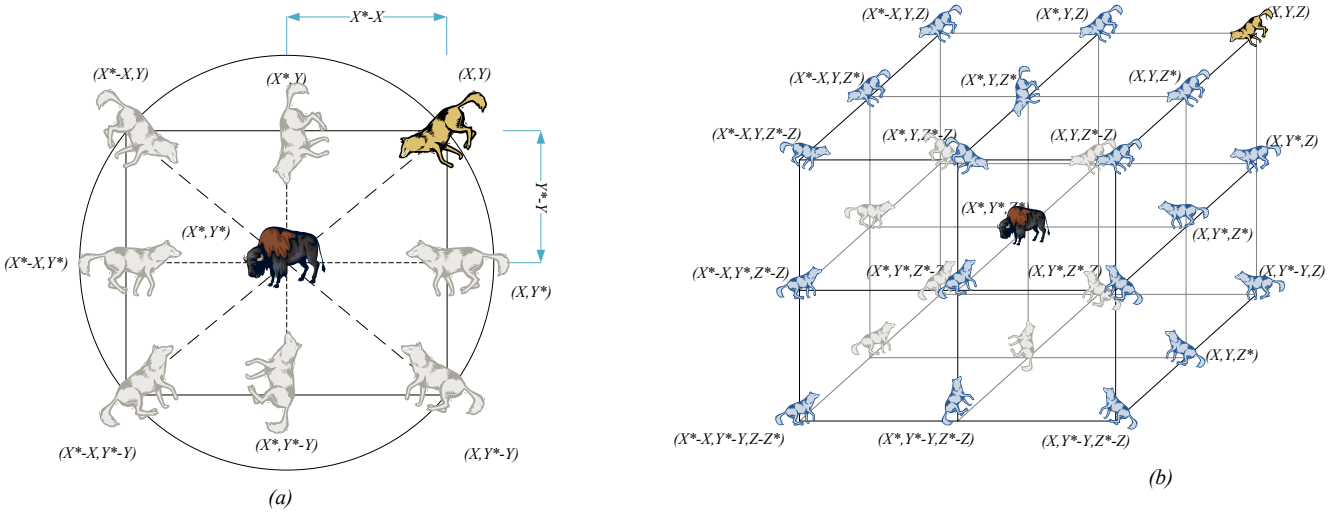

Figure 3-3 2D and 3D position vectors and their possible next locations

The same concept can be extended to a search space with n dimensions, and the grey wolves will move in hyper-cubes (or hyper-spheres) around the best solution obtained so far.

Hunting:

Grey wolves have the ability to recognize the location of prey and encircle them. The hunt is usually guided by the alpha. The beta and delta might also participate in hunting occasionally. However, in an abstract search space, we have no idea about the location of the optimum (prey). In order to mathematically simulate the hunting behavior of grey wolves, we suppose that the alpha (best candidate solution) beta and delta have better knowledge about the potential location of prey. Therefore, we save the first three best solutions obtained so far and oblige the other search agents (including the omegas) to update their positions according to the position of the best search agent. The following formulas are proposed in this regard.

$$\overrightarrow{D_\alpha} = |\vec{C}_1.\overrightarrow{X_\alpha} - \vec{X}|, \overrightarrow{D_\beta} = |\vec{C}_2.\overrightarrow{X_\beta} - \vec{X}|, \overrightarrow{D_\delta} = |\overrightarrow{C_3}.\overrightarrow{X_\delta} - \vec{X}| \tag{3-5}$$

$$\overrightarrow{X_1} = \overrightarrow{X_\alpha} - \vec{a}_1.\left(\overrightarrow{D_\alpha}\right), \overrightarrow{X_2} = \overrightarrow{X_\beta} - \overrightarrow{a_2}.\left(\overrightarrow{D_\beta}\right), \overrightarrow{X_3} = \overrightarrow{X_\delta} - \overrightarrow{a_3}.\left(\overrightarrow{D_\delta}\right) \tag{3-6}$$

$$\vec{X}(t+1) = \frac{\overrightarrow{X_1} + \overrightarrow{X_2} + \overrightarrow{X_3}}{3} \tag{3-7}$$

Figure 3-4 shows how a search agent updates its position according to alpha, beta, and delta in a 2D search space. It can be observed that the final position would be in a random place within a circle, which is defined by the positions of alpha, beta, and delta in the search space. In other words, alpha, beta, and delta estimate the position of the prey, and other wolves update their positions randomly around the prey.

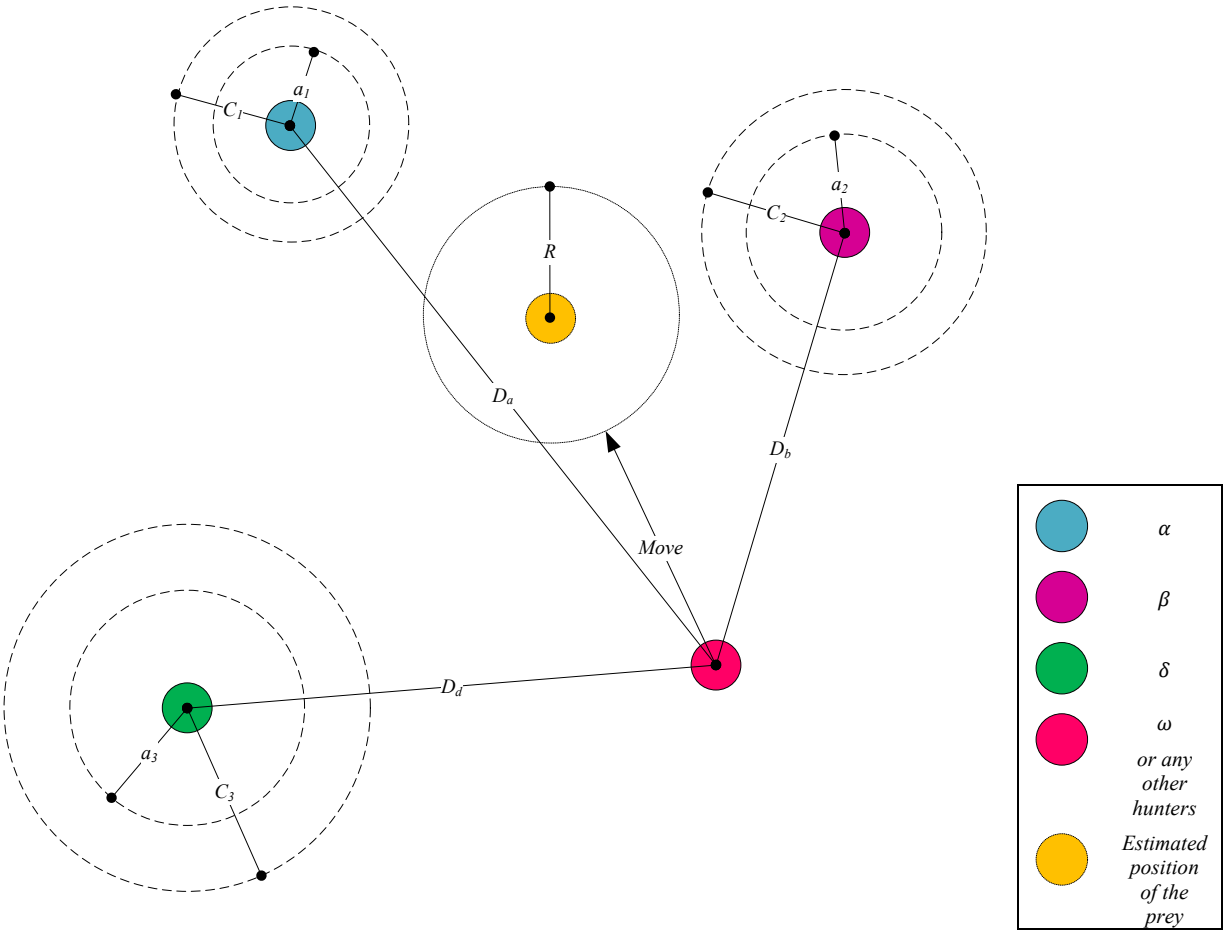

Figure 3-4 Position updating in GWO

Attacking prey (exploitation):

As mentioned above, the grey wolves finish the hunt by attacking the prey when it stops moving. In order to mathematically model approaching the prey, we decrease the value of $\vec{a}$. Note that the fluctuation range of $\vec{A}$ is also decreased by $\vec{a}$. In other words $\vec{A}$ is a random value in the interval [*-2a,2a*] where *a* is decreased from 2 to 0 over the course of iterations. When random values of $\vec{A}$ are in [-1,1], the next position of a search agent can be in any position between its current position and the position of the prey. Figure 3-5 (a) shows that |A|<1 forces the wolves to attack towards the prey.

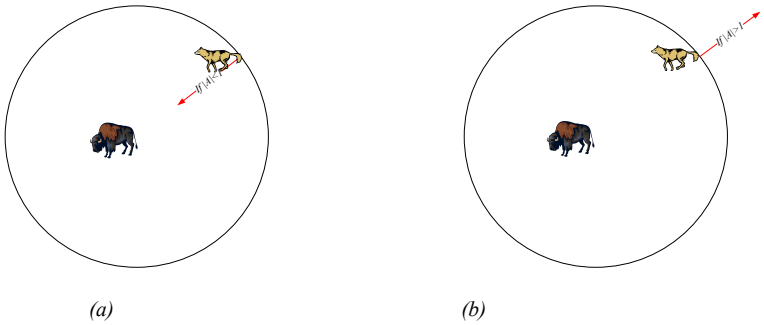

Figure 3-5 Attacking prey versus searching for prey

With the operators proposed so far, the GWO algorithm allows its search agents to update their position based on the location of the alpha, beta, and delta; and attack towards the prey. However, the GWO algorithm is prone to stagnation in local solutions with these operators. It is true that the encircling mechanism proposed shows exploration to some extent, but GWO needs more operators to emphasize exploration.

Search for prey (exploration):

Grey wolves mostly search according to the position of the alpha, beta, and delta. They diverge from each other to search for prey and converge to attack prey. In order to mathematically model divergence, we utilize $\vec{A}$ with random values greater than 1 or less than -1 to oblige the search agent to diverge from the prey. This emphasizes exploration and allows the GWO algorithm to search globally. Figure 3-5(b) also shows that |A|>1 forces the grey wolves to diverge from the prey to hopefully find a fitter prey. Another component of GWO that favors exploration is $\vec{C}$. As may be seen in Equation (3-4), the $\vec{C}$ vector contains random values in [0, 2]. This component provides random weights for prey in order to stochastically emphasize ($C>1$) or deemphasize ($C<1$) the effect of prey in defining the distance in Equation (3-1). This assists GWO to show a more random behavior throughout optimization, favoring exploration, and local optima avoidance. It is worth mentioning here that C is not linearly decreased in contrast to A. We deliberately require C to provide random values at all times in order to emphasize exploration not only during initial iterations but also final iterations. This component is very helpful in case of local optima stagnation, especially in the final iterations.

The C vector can also be considered as the effect of obstacles to approaching prey in nature. Generally speaking, the obstacles in nature appear in the hunting paths of wolves and in fact, prevent them from quickly and conveniently approaching prey. This is exactly what the vector C does. Depending on the position of a wolf, it can randomly give the prey a weight and make it harder and farther to reach for wolves or vice versa.

To sum up, the search process starts with creating a random population of grey wolves (candidate solutions) in the GWO algorithm. Over the course of iterations, alpha, beta, and delta wolves estimate the probable position of the prey. Each candidate solution updates its distance from the prey. The parameter a is decreased from 2 to 0 in order to emphasize exploration and exploitation, respectively. Candidate solutions tend to diverge from the prey when $|\vec{A}|>1$ and converge towards the prey when $|\vec{A}|<1$. Finally, the GWO algorithm is terminated by the satisfaction of an end criterion.

The pseudo code of the GWO algorithm is presented in Figure 3-6.

```
Initialize the grey wolf population X_i (i = 1, 2, ..., n)
Initialize a, A, and C
Calculate the fitness of each search agent
X_α=the best search agent
X_β=the second best search agent
X_δ=the third best search agent
while (t < Max number of iterations)
    for each search agent
            Update the position of the current search agent by equation (3-6)
    end for
    Update a, A, and C
    Calculate the fitness of all search agents
    Update X_α, X_β, and X_δ
    t=t+1
end while
return X_α
```

Figure 3-6 Pseudocode of the GWO algorithm

To see how GWO is theoretically able to solve optimization problems, some points may be noted:

- The proposed social hierarchy assists GWO to save the best solutions obtained so far over the course of the iteration
- The proposed encircling mechanism defines a circle-shaped neighborhood around the solutions which can be extended to higher dimensions as a hyper-sphere
- The random parameters A and C assist candidate solutions to have hyper-spheres with different random radii
- The proposed hunting method allows candidate solutions to locate the probable position of the prey
- Exploration and exploitation are guaranteed by the adaptive values of a and A
- The adaptive values of parameters a and A allow GWO to smoothly transition between exploration and exploitation
- With decreasing A, half of the iterations are devoted to exploration ($|A| \geq 1$) and the other half are dedicated to exploitation ($|A| < 1$)
- The GWO has only two main parameters to be adjusted (a and C)

There are possibilities to integrate mutation and other evolutionary operators to mimic the whole life cycle of grey wolves. However, we have kept the GWO algorithm as simple as possible, with the fewest operators to be adjusted.

3.2 Salp Swarm Algorithm (SSA): A Bio-inspired Optimizer for Engineering Design Problems

3.2.1 Inspiration

This section is based on the paper published in the Journal of Advances in Engineering Software [22]. Salps belong to the family of Salpidae and have a transparent barrel-shaped body. Their tissues are highly similar to jellyfishes. They also move very similar to jellyfish, in which the water is pumped through the body as propulsion to move forward [27]. The shape of a salp is shown in Figure 3-7(a).

The biological research about this creature is in its early milestones, mainly because their living environments are extremely difficult to access, and it is really difficult to keep them in laboratory environments. One of the most interesting behaviors of salps, which is of interest in this chapter, is their swarming behavior. In deep oceans, salps often form a swarm called the salp chain. This chain is illustrated in Figure 3-7(b). The main reason for this behavior is not very clear yet, but some researchers believe that this is done for achieving better locomotion using rapid coordinated changes and foraging [28].

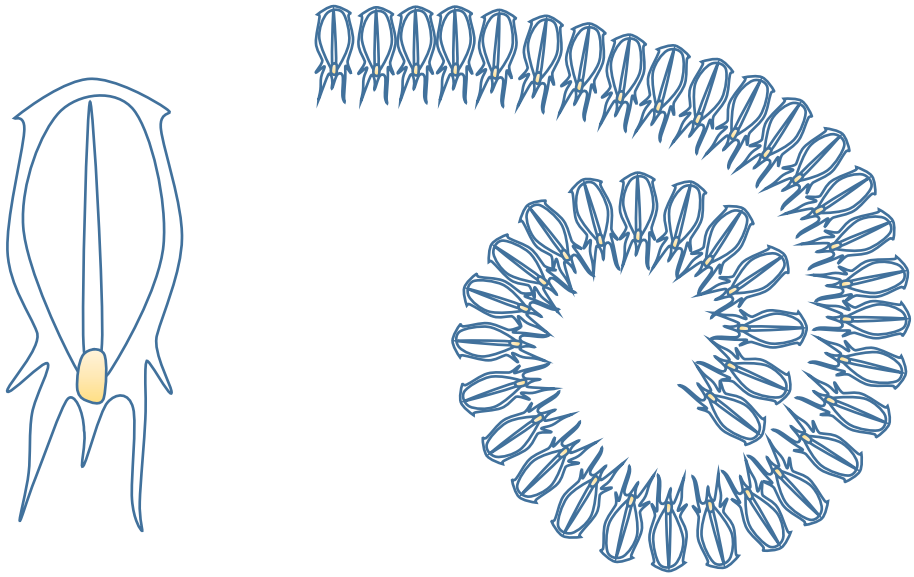

Figure 3-7 (a) individual salp, (b) swarm of salps (salps chain)

3.2.2 Proposed mathematical model for moving salp chains

There is little in the literature to mathematically model the swarming behaviors [29] and the population of salps [30]. We proposed the first mathematical model of salp swarms for solving optimization problems, while swarms of bees, ants, and fishes have been widely modeled and used for solving optimization problems [22]. This subsection explains the first model of salp chains in the literature for the purpose of solving optimization problems.

To mathematically model the salp chains, the population is first divided into two groups: leader and followers. The leader is the salp at the front of the chain, whereas the rest of the salps are considered as followers. As the name of these salps implies, the leader guides swarm, and the followers follow each other (and leader directly or indirectly).

Similar to other swarm-based techniques, the position of salps is defined in an *n*-dimensional search space where *n* is the number of variables of a given problem. Therefore, the position of all salps is stored in a two-dimensional matrix called *x*. It is also assumed that there is a food source called *F* in the search space as the swarm's target.

To update the position of the leader, the following equation is proposed:

$$x_j^1 = \begin{cases} F_j + c_1\left(\left(ub_j - lb_j\right)c_2 + lb_j\right) & c_3 \geq 0 \\ F_j - c_1\left(\left(ub_j - lb_j\right)c_2 + lb_j\right) & c_3 < 0 \end{cases} \tag{3-8}$$

where x_j^1 shows the position of the first salp (leader) in the *j-th* dimension, F_j is the position of the food source in the *j-th* dimension, ub_j indicates the upper bound of *j-th* dimension, lb_j indicates the lower bound of *j-th* dimension, c_1, c_2, and c_3 are random numbers.

Eq. (3-8) shows that the leader only updates its position with respect to the food source. The coefficient c_1 is the most important parameter in SSA because it balances exploration and exploitation defined as follows:

$$c_1 = 2e^{-\left(\frac{4l}{L}\right)^2} \tag{3-9}$$

where *l* is the current iteration and *L* is the maximum number of iterations.

The parameter c_2 and c_3 are random numbers uniformly generated in the interval of [0,1]. In fact, they dictate if the next position in *j-th* dimension should be towards positive infinity or negative infinity as well as the step size.

To update the position of the followers, the following equations is utilized (Newton's law of motion):

$$x_j^i = \frac{1}{2}at^2 + v_0 t \tag{3-10}$$

were $i \geq 2$, x_j^i shows the position of *i-th* follower salp in *j-th* dimension, *t* is time, v_0 is the initial speed, and $a = \frac{v_{final}}{v_0}$ where $v = \frac{x - x_0}{t}$.

Because the time in optimization is iteration, the discrepancy between iterations is equal to 1, and considering $v_0 = 0$, this equation can be expressed as follows:

$$x_j^i = \frac{1}{2}\left(x_j^i + x_j^{i-1}\right) \tag{3-11}$$

where $i \geq 2$ and x_j^i shows the position of *i-th* follower salp in *j-th* dimension. With Eqs. (3-8) and (3-11), the salp chains can be simulated.

3.2.3 Swarm simulation

In order to see the effects of the above mathematical model proposed, a simulation is done in this subsection. Twenty salps are randomly placed on a search space with stationary or moving

sources of food. The position of the salp chains and history of each salp are drawn in Figure 3-8 to Figure 3-11. Note that the blue point in the figures shows the position of the food source, and the darkest filled circle is the leading salp. The follower salps are colored with a grey-based on their position in the salp chain with respect to the leader. Inspecting the behaviour of salp chain over nine consecutive iterations in Figure 3-8 and Figure 3-10, it may be observed that the swarm can be formed and moved using the equation proposed effectively right after the first iteration. Also, it can be seen that the leading salp changes its position around the food source and follower salps gradually follow it over the course of iterations. The same model has been utilized for both simulations and the merits of the model proposed in both 2D and 3D spaces are evident in Figure 3-8 and Figure 3-10. It can be stated that the model is able to show the same behavior in an *n*-dimensional space.

Figure 3-8 and Figure 3-11 show the position history of salps around stationary and mobile food sources in 2D and 3D space after 100 iterations. The points searched around the stationary food source show that the salps effectively move around the search space. The distribution of points is reasonable and shows that the model proposed is able to explore and exploit the space around the stationary food source. Also, Figure 3-9 and Figure 3-11 show that the mathematical model proposed it requires salps in the salp chain to chase a moving food source. The distribution of the points searched around the start point is higher than the endpoint. This is due to the c_1 parameter, which controls exploration and exploitations. These findings evidence that the model of the salp chain movement is able to explore and exploit the space around both stationary and mobile food sources.

3.2.4 Single-objective Salp Swarm Algorithm (SSA)

The mathematical model for simulating salp chains cannot be directly employed to solve optimization problems. In other words, there is a need to tweak the model a little bit to make it applicable to optimization problems. The ultimate goal of a single-objective optimizer is to determine the global optimum. In the SSA swarm model, follower salps follow the leading salp. The leading salp also moves towards the food source. If the food source is replaced by the global optimum, therefore, the salp chain automatically moves towards it. However, the problem is that the global optimum of optimization problems is unknown. In this case, it is assumed that the best solution obtained so far is the global optimum and assumed as the food source to be chased by the salp chain.

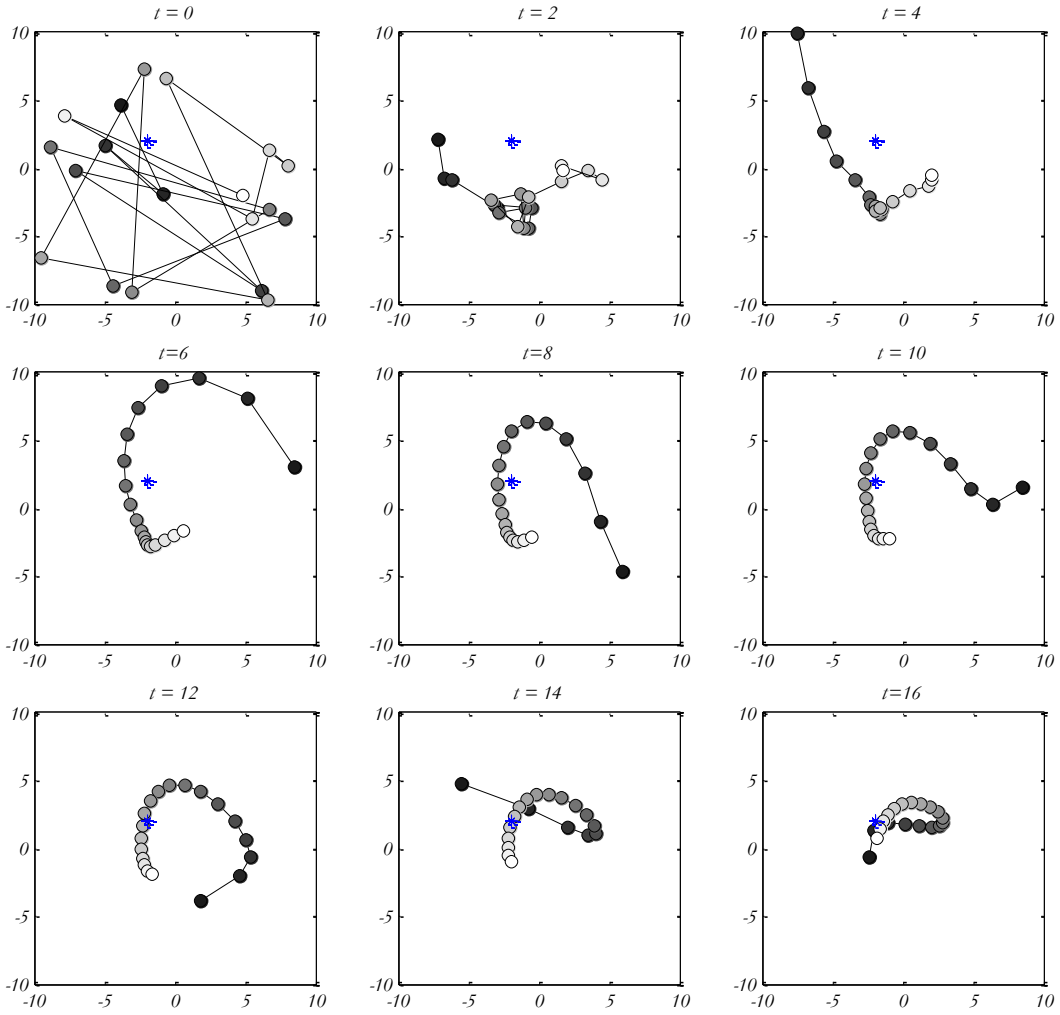

Figure 3-8 Slap chain movement around a stationary source of food in a 2D space.

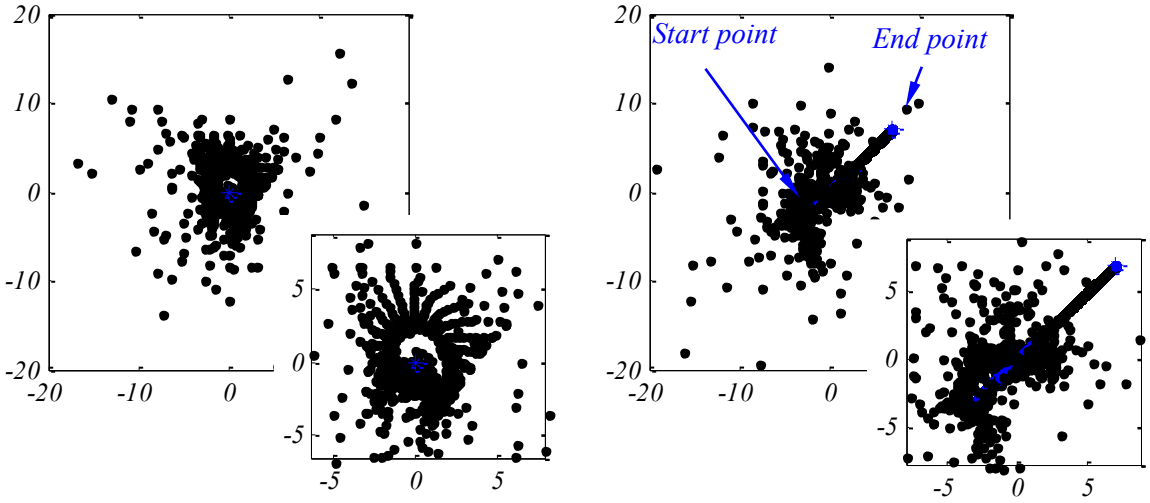

Figure 3-9 Search history around stationary and mobile food sources in a 2D space after 100 iterations.

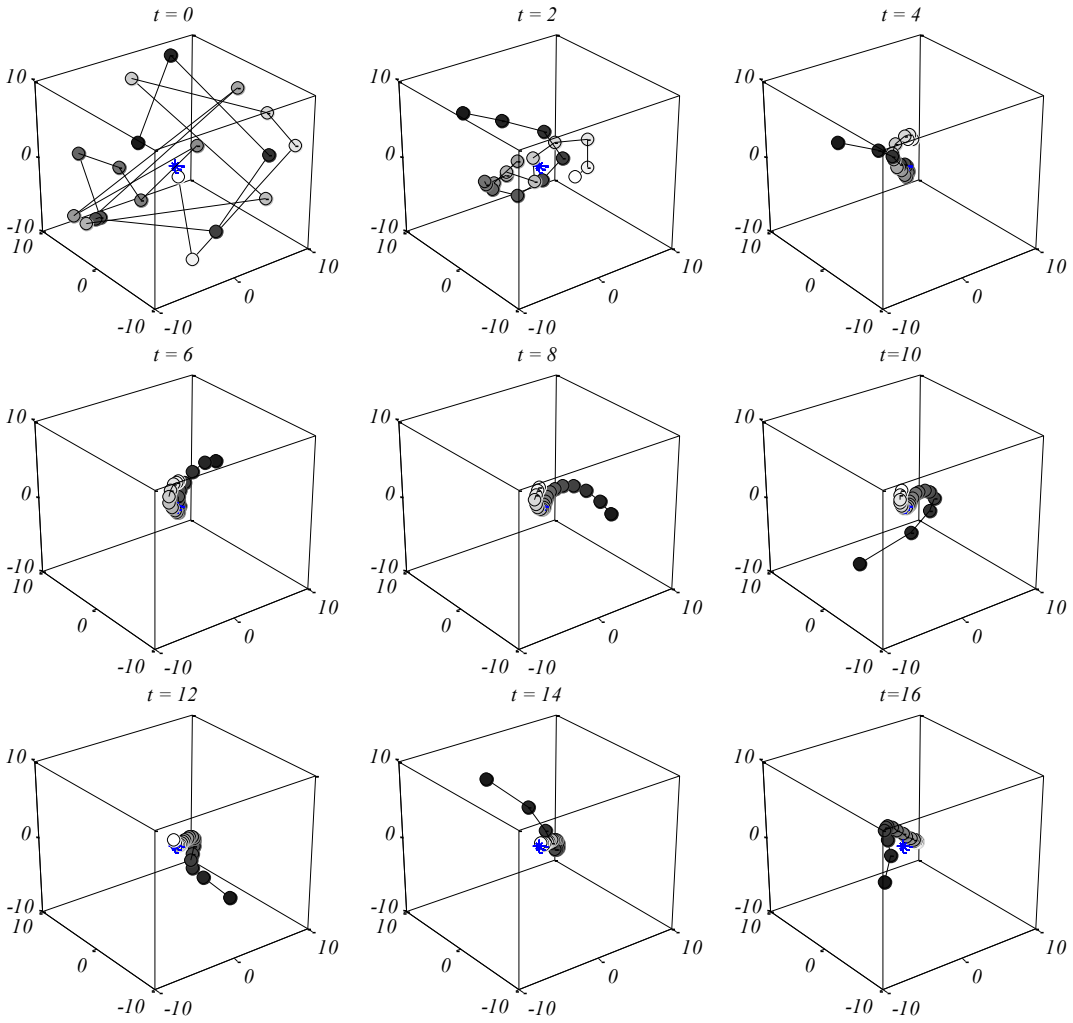

Figure 3-10 Slap chain movement around a stationary source of food in a 3D space.

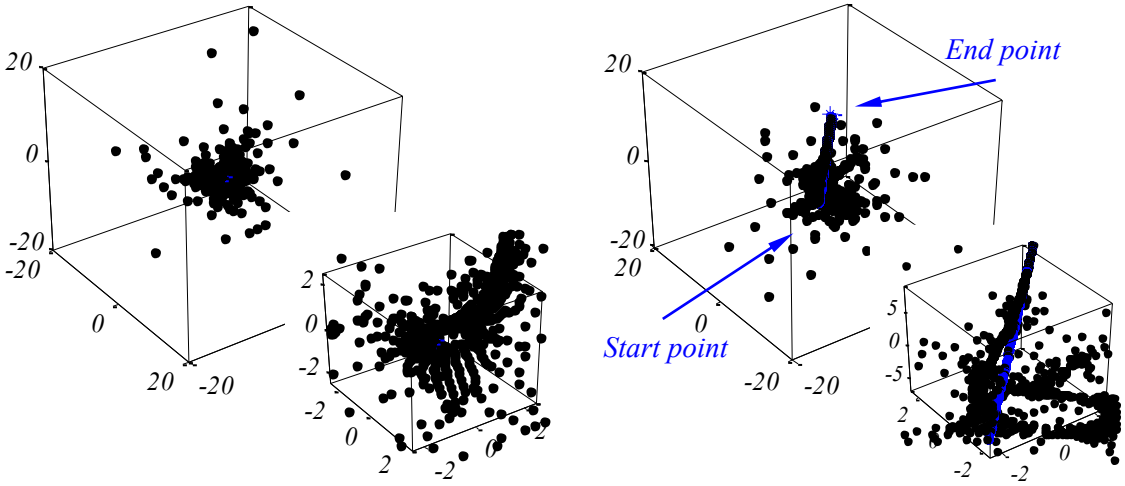

Figure 3-11 Search history around stationary and mobile food sources in a 3D space after 100 iterations.

The pseudo-code of the SSA algorithm is illustrated in Figure 3-12. This figure shows that the SSA algorithm starts approximating the global optimum by initiating multiple salps with random positions. It then calculates the fitness of each salp, finds the salp with the best fitness, and assigns the position of the best salp to the variable F as the source food to be chased by the salp chain. Meantime the coefficient c_1 is updated using Eq. (3-9). For each dimension, the position of leading salp is updated using Eq. (3-8) and the position of follower salps is updated utilizing Eq. (3-11). If any of the salps goes outside the search space, it will be brought back on the boundaries. All the above steps except initialization are iteratively executed until the satisfaction of an end criterion.

```
Initialize the salp population x_i (i = 1, 2, ..., n) considering ub and lb
while (end condition is not satisfied)
Calculate the fitness of each search agent (salp)
F=the best search agent
Update c_1 by Eq. (3.9)
    for each salp (x_i)
        if (i==1)
            Update the position of the leading salp by Eq. (3.8)
        else
            Update the position of the follower salp by Eq. (3.11)
        end
    end
    Amend the salps based on the upper and lower bounds of variables
end
return F
```

Figure 3-12 Pseudo code of the SSA algorithm.

It should be noted that the food source will be updated during optimization because the salp chain is very likely to find a better solution by exploring and exploiting the space around it. The simulations in subsection 3.2.3 show that the salp chain modeled is able to chase a moving food source. Therefore, the salp chain has the potential to move towards the global optimum that changes over the course of iterations. To see how the proposed salp chain model and SSA algorithm are effective in solving optimization problems, some remarks are listed as follows:

- SSA algorithm saves the best solution obtained so far and assigns it to the food source variable, so it never gets lost even if the whole population deteriorates.
- SSA algorithm updates the position of the leading salp with respect to the food source only, which is the best solution obtained so far, so the leader always explores and exploits the space around it.
- SSA algorithm updates the position of follower salps with respect to each other, so they move gradually towards the leading salp.
- Gradual movements of follower slaps prevent the SSA algorithm from easily stagnating in local optima.
- Parameter c_1 is decreased adaptively over the course of iterations, so the SSA algorithm first explores the search space and then exploits it.
- SSA algorithm has only one main controlling parameter (c_1).
- SSA algorithm is simple and easy to implement.

These remarks make the SSA algorithm theoretically and potentially able to solve single-objective optimization problems with unknown search spaces. The adaptive mechanism of SSA

allows this algorithm to avoid local solutions and eventually finds an accurate estimation of the best solution obtained during optimization. Therefore, it can be applied to both unimodal and multimodal problems. The above-mentioned advantages potentially allow SSA to outperform recent algorithms. However, this cannot be guaranteed for all optimization problems according to the No-Free-Lunch (NFL) theorem, which stated that none of such algorithms are able to solve all optimization problems [31].

3.2.5 Multi-objective Salp Swarm Algorithm (MSSA)

The solution for a multi-objective problem is a set of solutions called the Pareto optimal set. The SSA algorithm is able to drive salps towards the food source and updates it over the course of iterations. However, this algorithm is not able to solve multi-objective problems, mainly due to the following two reasons:

- SSA only saves one solution as the best solution, so it cannot store multiple solutions as the best solutions for a multi-objective problem.
- SSA updates the food source with the best solution obtained so far in each iteration, but there is no single best solution for multi-objective problems.

This first issue is tackled by equipping the SSA algorithm with a repository of food sources. This repository maintains the best non-dominated solutions obtained so far during optimization and is very similar to the archives in Multi-Objective Particle Swarm Optimization (MOPSO) [32]. The repository has a maximum size to store a limited number of non-dominated solutions. During optimization, each salp is compared against all the repository residents using the Pareto dominance operators. If a salp dominates a solution in the repository, they have to be swapped. If a salp dominates a set of solutions in the repository, they all should be removed from the repository, and the salp should be added in the repository. If at least one of the repository residents dominates a salp in the new population, it should be discarded straight away. If a salp is non-dominated in comparison with all repository residents, it has to be added to the archive.

These rules can guarantee that the repository always stores the non-dominated solutions obtained so far by the algorithm. However, there is a special case where the repository becomes full and a salp is non-dominated in comparison with the repository residents. Of course, the easiest way is to randomly delete one of the solutions in the archive and replace it with the non-dominated salp. A wiser way is to remove one of the similar non-dominated solutions in the repository. Since *a posteriori* multi-objective algorithm should be able to find uniformly distributed Pareto optimal solutions, the best candidate to remove from the archive is the one in a populated region. This approach improves the distribution of the archive residents over the course of iterations.

To find the non-dominated solutions with populated neighbourhood, the number of neighbouring solutions with a certain maximum distance is counted and assumed. This distance is defined by $\vec{d} = \frac{\overrightarrow{max} - \overrightarrow{min}}{repository\ size}$ where *max* and *min* are two vectors for storing maximum and minimum values for every objective, respectively. The repository with one solution in each segment is the best case. After assigning a rank to each repository resident based on the number of neighboring solutions, a roulette wheel is employed to choose one of them. The more number of neighboring solutions (the larger rank number) for a solution, the higher probability of removing it from the repository. An example of this repository update mechanism is illustrated in Figure 3-13. Note that the neighborhood should be defined for all the solutions, but only four of

the non-dominated solutions are investigated in this figure.

As mentioned above, the second issue when solving multi-objective problems using SSA is the selection of the food source because there is more than one best solution in a multi-objective search space. Again, the food source can be chosen randomly from the repository. However, a wiser way is to select it from a set of non-dominated solutions with the least crowded neighborhood. This can be done using the same ranking process and roulette wheel selection employed in the repository maintenance operator. The main difference is the probability of choosing the non-dominated solutions. In the archive maintenance, the solutions with a higher rank (crowded neighborhood) are more likely to be chosen. By contrast, the less populated neighborhood (the lower rank number) for a non-dominated solution in the repository, the higher probability of being selected as the food source. In Figure 3-13, for instance, the non-dominated solutions in the middle with no neighboring solution have the highest probability of being chosen as the food source. After all, the pseudo-code of the Multi-objective Salp Swarm Algorithm (MSSA) is shown in Figure 3-14.

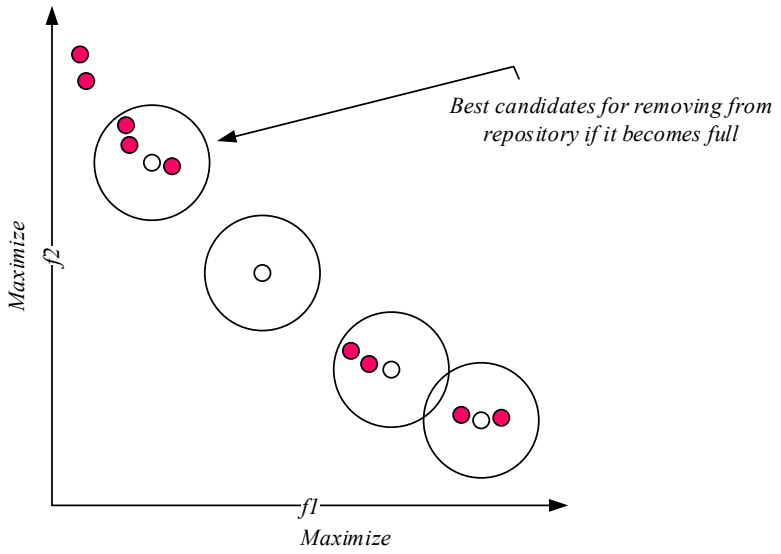

Figure 3-13 Update mechanism of the repository when it is full.

Figure 3-14 shows that the MSSA algorithm first initializes the population of salps with respect to upper bounds and lower bourns of variables. This algorithm then calculates the objective values for each salp and finds the non-dominated ones. The non-dominated solutions are added to the archive if the repository is not full. If the repository is full, the repository maintenance is run to delete the solutions with a crowded neighborhood. In this step, the solutions are first ranked and then selected using a roulette wheel. After removing enough number of repository residents, the non-dominated salps can be added to the repository. After updating the repository, a food source is selected from the non-dominated solutions in the repository with the least crowded neighborhood. Similarly, to the archive maintenance, this is done by ranking the solutions and employing a roulette wheel. The next step is to update c_1 using Eq. (3-9) and update the position of leading/follower salps using either Eq. (3-8) or Eq. (3-11). If during the process of updating the position, a salp goes outside of the boundaries, it will be brought back on the boundary. Finally, all the above steps except initialization are repeated until the satisfaction of an end condition.

To see how effective the MSSA algorithm is, some comments are:

- The non-dominated solutions obtained so far are stored in a repository, so they never get lost even if the entire population deteriorates in an iteration.
- The solutions with the crowded neighborhood are discarded every time the repository maintenance is called, which results in improving the coverage of non-dominated solutions across all objectives.
- A food source is selected from the list of non-dominated solutions with the least number of neighboring solutions, which leads the search towards the less crowded regions of the Pareto optimal front obtained and improves the coverage of solutions found.
- MSSA inherits the operators of SSA due to the use of a similar population division (leading and follower salps) and position updating process.
- MSSA algorithm has only two main controlling parameters (c_1 and archive size).
- MSSA algorithm is simple and easy to implement.

These comments show that the MSSA algorithm is logically able to find accurate Pareto optimal solutions with high distribution across all objectives.

```
Initialize the salp population x_i (i = 1, 2, ..., n) considering ub and lb
while (end criterion is not met)
    Calculate the fitness of each search agent (salp)
    Determine the non-dominated salps
    Update the repository considering the obtained non-dominated salps
    if the repository becomes full
        Call the repository maintenance procedure to remove one repository resident
        Add the non-dominated salp to the repository
    end
    Choose a source of food from repository: F=SelectFood(repository)
    Update c_1 by Eq. (3-9)
    for each salp (x_i)
        if (i==1)
            Update the position of the leading salp by Eq. (3-8)
        else
            Update the position of the follower salp by Eq. (3-11)
        end
    end
    Amend the salps based on the upper and lower bounds of variables
end
return repository
```

Figure 3-14 Pseudo code of the MSSA algorithm.

Chapter 4: Design optimization of OAM fibers using the grey wolf optimizer

4.1 Introduction

This chapter is based on the paper published in the Journal of Applied Optics [1]. The demand for higher capacity in optical fiber communication systems is ever-increasing. Recently, Mode Division Multiplexing (MDM) schemes have attracted much attention as a path to increase the transmission capacity beyond the nonlinear Shannon limit inherent in conventional single-mode fiber [33]. MDM uses a set of spatially orthogonal modes as independent optical channels to transmit the data. Those modes are supported modes of a multi-mode fiber. In conventional MDM systems, linearly polarized (LP) modes are utilized since they are easily excited and detected instead of using true vector modes [34]. A number of papers in the literature explored MDM implementations based on LP modes of weakly-guiding multi-mode fibers [35]–[42]. An important concern with LP modes in weakly-guiding multi-mode fibers is that they easily couple to each other, since their neighboring guided modes have a very similar effective indices. As a result, the cross-talk level between channels can be significant. Therefore, a complex multiple-input multiple-output (MIMO) processing is required on the receiver side to extract each channel.

Recently, the use of orbital angular momentum (OAM) modes has been proposed for MDM systems [43]–[48]. OAM modes are also orthogonal to each other. Typically, an OAM mode has a helical phase front and is characterized by a topological charge (l) indicating how many phase rotations are there over the field distribution plane. The difference between LP modes and OAM modes is that LP modes are made from a superposition of multiple degenerate vector modes; however, circularly-polarized OAM modes are themselves a single degenerate vector mode. This degenerate mode can be $EH_{l-1,m}$ or $HE_{l+1,m}$ where l is the topological charge and m is the radial number [49]. Since those OAM modes are made from one degenerate mode, it is possible to engineer the fiber and to achieve enough effective index separation between the OAM modes and other fiber modes. This situation makes the OAM modes more stable and robust to perturbations. As a result, we can simplify or eliminate complex MIMO processing, which is an essential part of MDM systems based on LP modes. OAM modes can exist on typical multi-mode fibers but they are unstable and easily couple into LP modes because $EH_{l-1,m}$ and $HE_{l+1,m}$ modes in such fibers are nearly degenerate (i.e. they have a very close mode effective index). Hence, those modes are strongly coupled to each other as they transmit through the fiber [43]. Therefore, to take advantage of OAM modes, it is necessary to design a new type of optical fiber in which the modal degeneracies between the aforementioned vector modes have been lifted.

The most popular fiber structure supporting OAM modes is a ring core fiber (RCF) with a high refractive index contrast [33]. This structure can increase the differences between the effective indices (Δn_{eff}) of $EH_{l-1,m}$ and $HE_{l+1,m}$ modes. In the literature, there are a number of works focused on designing OAM fibers. For example, some designs of step-index RCFs were introduced to achieve OAM modes with topological charge (l) of 1 and 2 [50]. Other fiber structures such as inverse parabolic index fibers [51], RCFs with graded-index [52], photonic crystal (PhC) fibers [53], and trench-assisted index fibers [54] can increase Δn_{eff} and mitigate mode mixing.

Having an abrupt refractive index change that coincides with a large amplitude of the transverse mode field and its gradient can strongly break the degeneracy of the fiber modes [55]. Hollow-core RCFs with an air-filled inner cladding provide a very high refractive index contrast at the interface of their ring core and inner air cladding. Therefore, such fibers are one of the most

promising fiber designs supporting a large number of high-quality OAM modes [56]–[60].

In spite of the diversity in proposed OAM fiber designs, there is still an urgent need for a comprehensive framework for designing such fibers. Usually, this kind of design has been done by using computer simulations coupled with a trial-and-error approach. This method is not efficient, requiring intensive human involvement and, more importantly, without any guarantees that the obtained design is optimal.

In [33], an initial systematic optimal fiber design method using the particle swarm optimization algorithm has been proposed, where some criteria derived from total system requirements have been considered for designing OAM fibers. This method can address the basic requirements of OAM fiber design, but it still needs to be improved to become more accurate, time-efficient, and to better include other OAM fiber requirements. That work considered some performance merit factors and combined them in a way that allows the use of a single-objective optimization approach. However, this is not ideal. The problem of designing OAM fibers is intrinsically a multi-objective problem, and the actual solutions for such problems is a set of optimal solutions. Solving such a problem with the single objective approach is able to find just one of the optimal designs. Hence, it is necessary to formulate the OAM fiber design problem as a multi-objective optimization problem and to utilize proper multi-objective algorithms.

Previously, we have used the same approach and utilized artificial intelligence techniques to design a few optimized optical devices such as optical modulators [61], large mode area PhC fibers [4], PhC filters [2], [62], [63], PhC liquid sensors [6], PhC low bend loss waveguides [64], PhC LED [3], [65], waveguide-based LP_{01}–LP_{0m} mode converters [5], and PhC slow-light waveguides [66]–[75][76]. Also, other research groups followed the same approach for the optimization of bend-insensitive optical fiber [77], fiber amplifiers [78], and grating couplers [79].

In this chapter, firstly, we propose a new problem formulation of the single-objective optimization approach for designing OAM fibers. Then as a case study, we solve the problem of designing an RCF. Later, we change the problem formulation into a multi-objective form and then utilize a multi-objective optimizer algorithm to solve it. Then, we perform a proper comparative study to discuss the advantages of the new problem formulations. It should be noted that the main criterion to have a high-performance OAM fiber is to have a large number of supported OAM modes with very high mode purities. Furthermore, the effective index separation between the OAM modes and the other fiber modes should be larger than 1e-4. In addition, a minimum acceptable bending loss should be considered.

The rest of the chapter is organized as follows. We explain the structure of OAM fibers, then explain the basic concept, and go through the details of the OAM fiber design process in section 4.2. In section 4.3, the proposed optimization frameworks for designing OAM fibers are elaborated. The results of utilizing the proposed frameworks for designing a case study OAM fiber are provided in section 4.4. Eventually, section 4.5 concludes the work.

4.2 OAM fiber Structure and Related Issues

Typically, OAM modes have a doughnut-shaped intensity profile. Therefore, it is rational to expect that the refractive index profile of the fiber cross-section should follow a similar pattern. RCFs in which the ring section has a higher refractive index provide a more convenient medium for OAM mode transmission. The step-index RCF is shown in Figure 4-1.

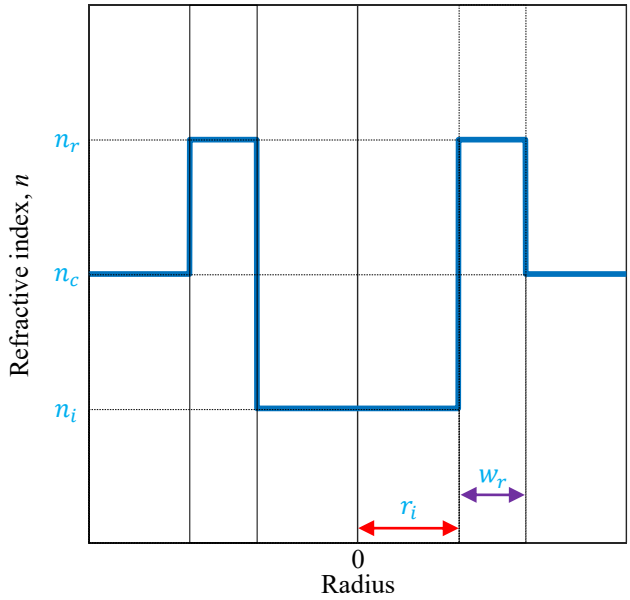

Figure 4-1 Cross-section refractive index profile of a step-index RCF.

Since our objective is to provide a fair comparative study, we use the same material for the fiber structure, as it is used in [33]. Also, we design the OAM fiber for the wavelength range of the C-band (from 1530 to 1565 nm). Therefore, the inner cladding can be either air ($n_i = 1$) or silica doped with fluorine (F) ($1 \leq n_i \leq 1.394$). The ring section is made of fused silica doped with germanium dioxide (GeO_2) ($1.447 \leq n_r \leq 1.4839$). The outer cladding is made of fused silica (SiO_2) with $n_c = 1.444$ @ $\lambda = 1.55$ µm. Also, we assume that the inner cladding radius can have a value in the range of 1.5 µm $\leq r_i \leq 14$ µm. The ring width can be in the range of 1.5 µm $\leq w_r \leq 6$ µm. The outer cladding diameter is considered to have a standard value of 125 µm.

To evaluate the performance of OAM fibers and to calculate their modal characteristics, we use the finite element method (FEM) [4]. Each OAM fiber structure supports a number of confined modes. Some of them can be used as the guided modes of the fiber. Therefore, a guided mode should have some specific characteristics as explained in the following.

Each mode has a mode profile and an effective index value. The effective index is a complex number in which the real part is associated to the propagation properties of the mode and the imaginary part is related to the loss coefficient. After each simulation, we sort the modes based on the real value of their effective refractive index.

As mentioned earlier, an OAM mode in the optical fiber results from a combination of two vector modes. In other words, we should look for every two consecutive modes generating an $OAM_{l,m}$ modes, where l is the topological charge and m is how many concentric rings are in the mode intensity profile. $OAM_{l,m}$ modes with $|l| > 1$ are expressed with the following equations [56].

$$OAM^{\pm}_{\pm l,m} = HE^{even}_{l+1,m} \pm jHE^{odd}_{l+1,m} \tag{4-1}$$

$$OAM^{\mp}_{\pm l,m} = EH^{even}_{l-1,m} \pm jEH^{odd}_{l-1,m} \tag{4-2}$$

where the superscript sign indicates the circular polarization direction and the sign of l shows the phase rotation direction. In OAM modes, the polarization and phase rotation of the modes are

interpreted as the spin and orbit of the modes. The spin and orbit of an OAM mode can be aligned or anti-aligned. Therefore, equation (4-1) shows the spin-orbit aligned and equation (4-2) indicates the spin-orbit anti-aligned mode.

The two groups of $HE_{l+1,m}$ and $EH_{l-1,m}$ modes are often degenerate. They have almost the same effective indices, resulting in mode mixing and the generation of the LP modes group. Interestingly, the step-index RCF of Figure 4-1 can break down the degeneracy of some $HE_{l+1,m}$ and $EH_{l-1,m}$ mode groups. Therefore, in the case that Δn_{eff} is high enough, the two obtained OAM modes of equations (4-1) and (4-2) will not interact anymore, and hence there will be no mode mixing. Note that each OAM mode obtained from equations (4-1) or (4-2) provides two channels (spin-orbit aligned and anti-aligned cases) for data communication. These two channels have crosstalk and require the use of a simple 2×2 MIMO to undo crosstalk within each channel.

The minimum acceptable Δn_{eff}, which is necessary to mitigate significant mode coupling, varies based on the target transmission configuration. The conventional minimum value of Δn_{eff} is 1e-4 [80]. This value is experimentally obtained and represents a threshold above which the modal crosstalk among OAM modes can be suppressed to a value lower than -10 dB after >1-km long transmission [59].

In addition to the necessity of having a minimum Δn_{eff} of 1e-4 between the OAM modes to the other fiber modes, another consideration should be taken into account. If adjacent mode groups ($HE_{l+1,m}$ to $HE_{l,m}$ or $EH_{l,m}$ to $EH_{l-1,m}$) are not sufficiently separated, bend-enabled mode coupling can cause significant inter-group crosstalk. Generally, the mode groups need to be separated by an effective index difference on the order of 1e-3 to suppress this mode coupling [81]. We refer to this effective index difference as $\Delta n_{eff\,g}$, and we have chosen a threshold of 0.7e-3.

In each optical fiber, there can be many OAM modes, but only a few of them may satisfy the requirements of the target transmission configuration. The main objective of the whole optimization process is to increase the number of eligible OAM modes which will satisfy the targeted requirements for data communication.

To organize the process of finding legitimate OAM modes for the application of data communication, we propose the following algorithm. After each simulation run, we sort the obtained fiber modes based on the real value of their effective index. We look for pairs of consecutive modes which may generate an OAM mode. Then, for each pair, we compute the linear combination $Mode_i+j*Mode_{i+1}$ (i is the mode number in the sorted order of the first mode in the pair) and then check whether the result is an OAM mode or not. After that, we calculate $|l|$ and m of the OAM modes. The next step is to filter out the obtained OAM modes and select some of them suitable for carrying data.

The $OAM_{l,m}$ modes with radial order m greater than one are difficult to generate and excite because they have a complex modal distribution [33]. Besides, the $OAM_{l,m}$ mode with $|l|=1$ is prone to experience a wide pulse spreading because of the parasitic effects of the TM_{01} and TE_{01} modes [82]. The $OAM_{l,m}$ mode with $l=0$ can be used for data communication; however, higher-order modes ($|l|>0$) provide more clear scalability advantages [47]. Depending on the requirements of the target transmission configuration, these modes can be filtered out from the last selected OAM modes. In this work, we consider $OAM_{l,m}$ modes with $m=1$ and $|l|>0$ as data-carrying OAM modes.

Typically, generating linear and circular polarized vector modes is prevalent, since the generation of arbitrarily polarized vector modes is quite challenging. This work will focus on the

generation of circularly polarized OAM modes.

We can define a number of merit factors to evaluate the quality of OAM modes. The Δn_{eff} (effective index separation) between the OAM mode and adjacent fiber modes should be very high, with a minimum acceptable value of 1e-4. The bending loss of the OAM modes should be very low with a maximum acceptable value of 0.0001 dB/m (@ 30 mm bending radius and λ=1565 nm) [33], [83]. In this work, we consider the bending loss as a criterion for selecting the OAM modes.

In order to quantify the OAM character of a mode, and its polarization properties, we calculate mode purity, polarization purity (PP), and polarization purity factor (PPF) for each mode.

The purity of an OAM mode is quantitatively calculated by using Fourier transform concepts. An OAM mode has a periodic dependence on the azimuthal angle ϕ. Therefore, the Fourier conjugate of ϕ is the OAM spectrum. To calculate how much a prospective OAM mode overlaps with an ideal OAM mode, we need to calculate the corresponding Fourier coefficient A_l. To calculate the coefficient A_l, first, we need to take a set of sampling data points (sampling phase $\psi(\varphi)$) from the middle of the doughnut-shaped section of the OAM mode in the range of $\varphi=[0\ 2\pi]$. The Fourier relationship between the sampling phase $\psi(\varphi)$ and the OAM spectrum A_l is given by equation (4-3) [84].

$$A_l = \frac{1}{2\pi}\int_0^{2\pi} \psi(\phi)\, e^{-il\phi} d\phi \tag{4-3}$$

The PP of a mode refers to how much its polarization deviates from perfect circular polarization [85], [86]. It is defined by the ratio of how much power of the mode belongs to the right circularly polarized (RCP) ideal OAM mode and to the left circularly polarized (LCP) one (equation (4-4)).

$$PP(dB) = 10log\left|\frac{P_{RCP}}{P_{LCP}}\right| = 20log\left|\frac{A_{+l}}{A_{-l}}\right| \tag{4-4}$$

The *PPF* of an OAM mode reflects its degree of circular polarization and has a value between 0 and 1 (equation (4-5)) [33].

$$PPF = \left(1 - e^{-\frac{PP}{\sigma}}\right)^w \tag{4-5}$$

where σ and w are tuning factors. The *PPF* has been proposed to transform the *PP* into a number that can be used to qualify acceptable levels of *PP*. Usually, the signal quality degradation is very important when polarization crosstalk ($\frac{1}{PP}$) is in the range of -10 dB to -30 dB [87]. For example, in the case of moderate quadrature-amplitude modulation (QAM) levels (<256), the bit-error-rate (BER) penalty is negligible as long as the crosstalk level is less than -30 dB. On the other hand, the BER is unacceptably high when crosstalk is around -10 dB, even for more robust modulations such as quadrature phase-shift keying (QPSK) [33]. Considering $\sigma=5$ and $w=30$, the *PPF* yields a curve that varies almost linearly with the *PP* in the range of 10 dB to 30 dB and saturates outside this range [33]. Assuming a minimum acceptable *PP* for OAM modes equals to 10 dB, the corresponding *PPF* value is 0.013. For other applications, the tuning factors σ and *w* should be

modified with respect to the acceptable levels of *PP*.

In order to evaluate the performance of the OAM fibers, we require to simulate at least four wavelengths (λ) over the entire working bandwidth. Also, we should verify that each OAM mode remains valid over the entire bandwidth. Based on the defined merit factors for OAM fibers, the overall objective of the optimization process is to increase the number of supported OAM modes, Δn_{eff}, and *PPF*.

In the next section, we will introduce the proposed optimization frameworks for designing OAM fibers.

4.3 Optimization frameworks for designing OAM fibers

As mentioned before, the objective of this chapter is to provide comprehensive optimization frameworks to maximize the number of supported OAM modes, *PPF*, and Δn_{eff} of OAM fibers. In addition, the proposed frameworks must be constructed to work independently without human involvement. The first step is to define the general expression for the cross-section refractive index profile of the OAM fiber. Subsequently, the framework automatically finds corresponding optimal values for the structural parameters. The proposed frameworks are divided into three main modules, as shown in Figure 4-2. These three modules are explained as follows:

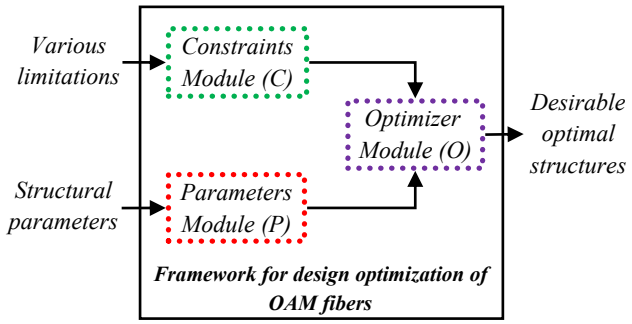

Figure 4-2 Proposed design optimization framework for designing OAM fibers.

A. Parameters Module (P)

Usually, there are several structural parameters for any optical device. Therefore, the structural parameters which need to be optimized should be defined in this module. In the case of the OAM fiber shown in Figure 4-1 r_i, w_r, n_i, and n_r are the corresponding structural parameters. The P module for this problem is given by:

$$P: \vec{x} = [r_i, w_r, n_i, n_r] \tag{4-6}$$

B. Constraints Module (C)

In this module, all of the considerations involved in the design of an OAM fiber should be addressed. Hence, for the structure shown in Figure 4-1 two sets of constraints are considered. The first set (C_1) is the available range of structural parameters. Any additional manufacturing limitations can be added to this set. The second set (C_2) involves the requirements of the target transmission configuration. The C module for designing OAM fiber of Figure 4-1 is given by:

$C = [C_1, C_2]$,

$\boldsymbol{C_1}$: (structural parameters $range$)
$1.5\ \mu m \leq r_i \leq 14\ \mu m$,
$1.5\ \mu m \leq w_r \leq 6\ \mu m$,
$1 \leq n_i \leq 1.394$,
$1.447 \leq n_r \leq 1.4839$ (4-7)

$\boldsymbol{C_2}$: ($for\ each\ OAM\ mode$)
$\Delta n_{eff} > 1e-4$,
$\Delta n_{eff\ g} > 1e-3$,
$Bending\ loss > 0.0001$ dB/m,
$PPF > 0.013$

C. Optimizer Module (O)

In this module, the objective function and an optimizer must be identified. The whole process of OAM fiber design should be formulated and considered in the objective function as shown in Figure 4-3. After that, the optimizer is connected to the objective function and looks for the optimal design(s) using an iterative process. We aim to maximize the number of supported OAM modes, *PPF*, and Δn_{eff} of OAM fibers. Note that there is a range of values for *PPF* and Δn_{eff} since these are wavelength-dependent quantities for each OAM mode. Therefore, we average the values of *PPF* and Δn_{eff} over the wavelength span of interest to come to a number that represents the overall quality of each OAM mode. After that, again, we calculate the average values of Avg(*PPF)* and Avg(Δn_{eff}) for all of the OAM modes to finally come up with a single value for each merit factor.

The first way to solve this multiple objective problem is to combine the different merit factors into a combined one, and use a single-objective optimization algorithm. Therefore, we can use $Cost = O_1 * O_2 * O_3$ where O_1 is the number of supported OAM modes, O_2=*mean(PPF)*, and O_3=*mean*(Δn_{eff}). Note that we consider the number of supported modes to be equal to the number of *EH* or *HE* modes which satisfy the conditions mentioned earlier. Using the more usual convention, this would correspond to twice the number of supported OAM modes (or the number of OAM channels).

The single-objective optimizer will be trying to maximize the *Cost*, which means that a high-performance OAM fiber design will be achieved.

The problem of solving such problems with the single-objective optimization approach is that we will lose many designs meeting the requirements, since the actual answer for the OAM fiber design problem is a set of optimal designs. The single-objective algorithm finds only one of these. To solve the problem with a multi-objective optimization approach, we consider O_1, O_2, and O_3 as three independent objectives and we apply a multi-objective optimization algorithm. The algorithm will find the Pareto optimal set of solutions which represent the best trade-offs among the objectives [73].

For the optimization work, several single- and multi-objective metaheuristic optimization algorithms can be used [21], [22], [24], [88]–[91]. We choose the Grey Wolf Optimizer (GWO) [21], [24], [91] since this algorithm has proved its performance in various fields of engineering

[92]. This algorithm simulates the collaboration and leadership of gray wolves when they want to hunt prey. One additional property of this algorithm is that it can explore the search space without being stuck in local minima [92]. This is very useful since the problem of designing OAM fibers is complicated [92].

We have designed an algorithm to manage the evaluation of OAM fibers and to calculate the merit factors, as shown in Figure 4-3. In this flowchart, firstly, a candidate OAM fiber design is evaluated @ $\lambda = 1.55$ μm. If the structure provides one or more OAM modes, the rest of the calculations will be done. Otherwise, the rest of the simulations/calculations are bypassed. By doing so, the process of evaluating a candidate OAM fiber design will be sped up. In [33], the authors use two FEM simulations for evaluating each candidate design. For sure, two simulations are not enough to calculate the behavior of Δn_{eff} over the entire bandwidth. We found out that four simulations or more over the entire bandwidth are required to evaluate the structures properly. Since FEM simulations are computationally expensive, we added two yes/no condition sections in the flowchart (Figure 4-3) to avoid unnecessary simulations. The second condition is added because sometimes a selected mode reaches the cutoff wavelength. Hence, it is necessary to verify that the selected modes are available over the entire working bandwidth.

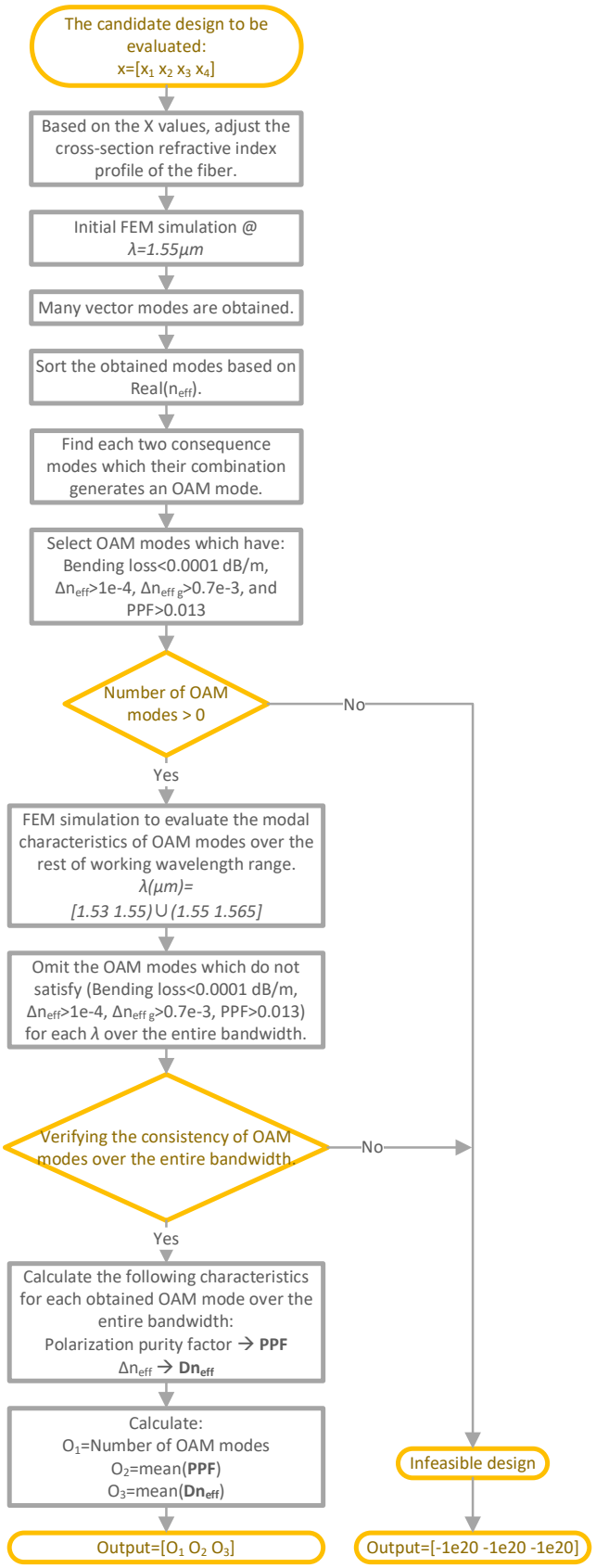

Figure 4-3 Flowchart of the objective function for the design optimization of OAM fibers.

In the case that a candidate design cannot satisfy first or second yes/no condition, the rest of the calculations are skipped. Since the objective function should have a set of values for its output in each point in the search space, a set of values should be assigned for such cases (infeasible designs). We consider a value of -1e20 for each merit factor, which is much worse than that of a normal valid design.

In the next section, we solve the problem of OAM fiber design with single- and multi-objective optimization approaches and provide a comparative study.

4.4 Results and discussion

After the proper set up of the modules, the framework was ready to design OAM fibers.

a) Single-objective optimization approach:

To solve the problem with a single-objective optimization algorithm, we used the single-objective version of GWO with 30 artificial grey wolves and up to 200 iterations. Artificial grey wolves start searching for the best solution from random positions in the search space. Through an iterative process, each artificial grey wolf updates its position until they reach the maximum iteration value. The maximum of 200 iterations is high enough so that we can be confident that the best solution (or a solution near it) has been found. The history of GWO searching is shown as a convergence curve in Figure 4-4. Also, the effective indices (n_{eff}) and the effective index differences (Δn_{eff}) as a function of wavelength over the bandwidth are also shown in Figure 4-5a and 5b. In the effective index differences graph (Figure 4-5b), we show the effective index distance between the different found modes. The graph shows that the optimized design has no modes with effective indices closer than 1e-4, even for pairs of modes with the same OAM order (solid lines), and that the distances to modes with different OAM order (dashed lines) are always larger than 2e-4, with mostly larger than 1e-3.

The obtained optimal structural parameters and corresponding output merit factors are shown in Table 4-1. In this table, we also show some of the obtained designs during the search. The final optimal design was found at the 107th iteration, which maximized *Cost* value. The designs obtained in iterations 7 and 55 show a higher number of supported OAM modes than that of the final optimal designs. Since the algorithm just considers the overall *Cost* value, it finally reached a design that shows the highest *Cost* value. This conflicting behavior among the output merit factors shows that this problem is intrinsically a multi-objective problem.

To justify the obtained design, we compare it with the best design of [33] since both have the same material in their structures. We have obtained 14 OAM modes; however, 4 modes are obtained in [33]. In this work, we do not sacrifice or dismiss any condition. With a more proper problem formulation, we could reach a better design.

Although the obtained result is satisfactory, the problem can be solved with a more comprehensive approach. As it has already been mentioned, this problem is a multi-objective problem and its actual solution is a set of optimal solutions. The single-objective optimizer can find only one of these optimal solutions. Therefore, we are more interested in solving the problem with a multi-objective approach.

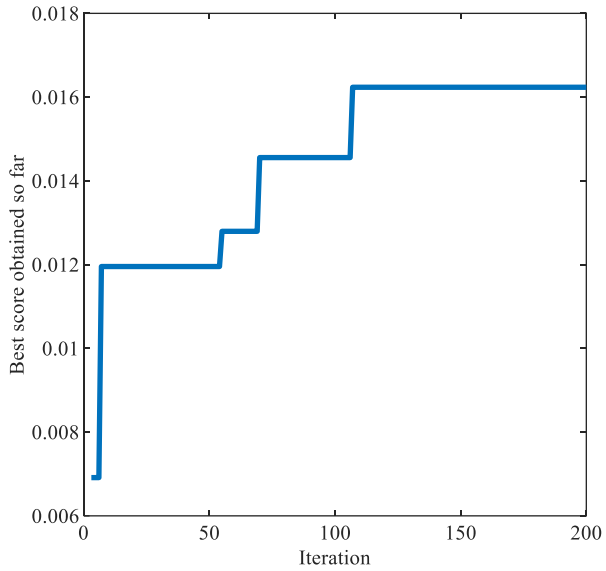

Figure 4-4 Convergence curve of single-objective GWO optimization.

Table 4-1: Properties of obtained structures by single-objective GWO

Structural parameters						Output merit factors			
Iter	r_i *(μm)*	w_r *(μm)*	n_i	n_r	*# of OAMs*	*Avg (PPF)*	*Avg* (Δn_{eff})	*Cost*	$\|l\|$
3	8.587	2.653	1.139	1.484	8	0.999	9.00E-04	6.90E-03	3 3 4 4 5 5 6 6
7	14	1.589	1.394	1.484	18	0.997	7.00E-04	1.20E-02	3 4 4 5 5 6 6 7 7 8 8 9 9 10 10 11 11 12
55	12.432	2.271	1.278	1.484	17	0.976	8.00E-04	1.27E-02	3 4 4 5 5 6 6 7 7 8 8 9 9 10 10 11 11
70	9.438	1.985	1.266	1.484	14	0.996	1.00E-03	1.46E-02	3 3 4 4 5 5 6 6 7 7 8 8 9 9
107	8.567	2.238	1	1.484	14	0.998	1.20E-03	1.62E-02	3 3 4 4 5 5 6 6 7 7 8 8 9 9

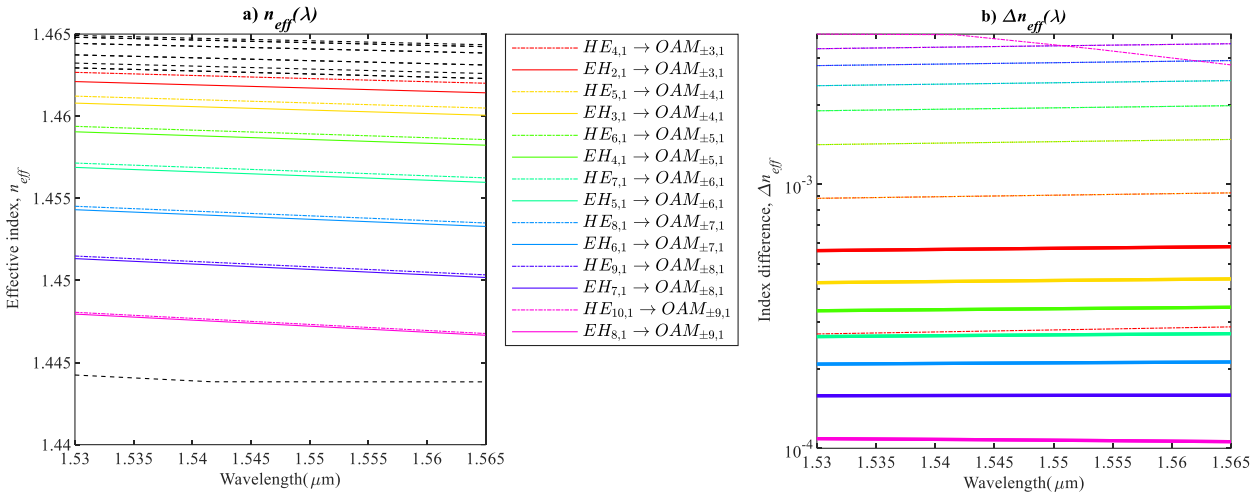

Figure 4-5 a) Effective indices (*neff*) as a function of wavelength over the C-band of optimal design obtained by single-objective GWO. The colored lines show the selected modes and the black dashed lines are other fiber modes. b) Effective index differences (*Δneff*) as a function of wavelength over the C-band of optimal design obtained by single-objective GWO. The solid lines correspond to the difference for modes with the same OAM order, and that the dashed lines correspond to the distance between OAM modes to other OAM or fiber modes.

b) Multi-objective optimization approach:

The O_1, O_2, and O_3 figures of merit show conflicting behavior (for instance, when O_1 increases O_3 decreases). Hence, it means that the problem of designing OAM fibers is intrinsically multi-objective. For this section, we used the multi-objective version of GWO (MGWO) with 30 artificial grey wolves and up to 200 iterations. In general, these algorithms start searching from random positions. In order to make the searching process easier and faster, the optimal design and some of the decent designs obtained by GWO in the previous section were fed to the MGWO as initial guesses. Finally, the optimization ended with 48 optimal designs. The search history of the MGWO and the Pareto front (Pareto optimal solution) is depicted in Figure 4-6 and 4-7. As it can be seen from the figures, a wide range of optimal designs are obtained, which are suitable for specific applications. Some of the obtained designs having a high number of supported OAM modes are shown in Table 4-2. All of the obtained designs have a very high *Avg(PPF)*. This is because of selecting proper modes and optimizing the structure to maximize *Avg(PPF)* as well as the other merit factors. In order to examine the performance of the obtained optimal designs in detail, we selected two optimal designs from Table 4-2 which are the best designs in terms of the number of supported OAM modes and $Avg(\Delta n_{eff})$. The effective indices (n_{eff}) and the effective index differences (Δn_{eff}) as a function of the wavelength of those two designs are shown in Figure 4-8.

The next step after finding the set of optimal solutions is to select an optimal design which is the best match with the requirements of the target transmission configuration. That is to say, we select the design with the trade-off best matched to the configuration between the performance merit factors. For example, in a case where we need 28 channels (14 OAM modes) and Δn_{eff} >1e-4, first, we remove from consideration any designs with less than 14 supported OAM modes. Since for all of the designs the condition of Δn_{eff} >1e-4 is satisfied, we just need to sort the rest of the designs with respect to *Avg(PPF)*. The optimal design with the highest *Avg(PPF)* is the best choice for this example.

The proposed method in this study can find a wide range of high-performance optimal designs.

The advantage of the proposed method is that we can easily define a new complex cross-section refractive index profile for an OAM fiber and let the optimizer find a wide range of optimally designed structures without human intervention. Finally, this method opens up a new way of designing high-performance OAM fibers for any target transmission configuration.

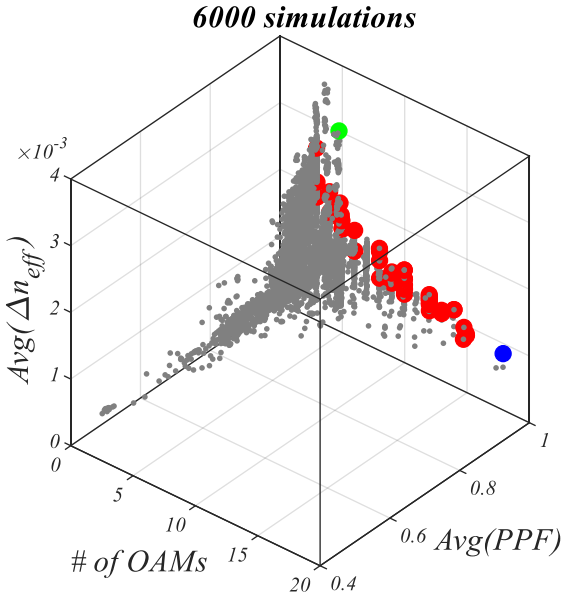

Figure 4-6 Search history of multi-objective GWO with some marked designs. The gray points are the evaluated designs during the search and the colorful points are the final optimal designs. The blue and green points represent the best designs in terms of the number of supported OAM modes and *Avg(Δneff)*, respectively.

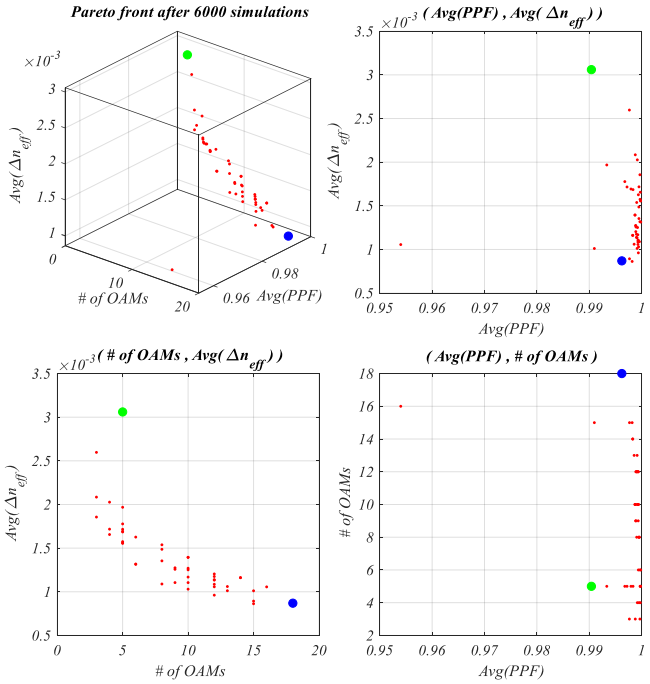

Figure 4-7 Pareto optimal solution of multi-objective GWO with some marked designs.

Table 4-2: Properties of obtained structures by multi-objective GWO

	label	Structural parameters				Output merit factors			
No.		r_i (μm)	w_r (μm)	n_i	n_r	# of OAMs	Avg (PPF)	Avg(Δn_{eff})	$\|l\|$
1	Blue	11.04	2.182	1.147	1.481	18	0.996	9.00E-04	2 3 4 4 5 5 6 6 7 7 8 8 9 9 10 10 11 11
2		9.532	2.252	1	1.484	16	0.991	1.10E-03	1 3 4 4 5 5 6 6 7 7 8 8 9 9 10 10
3		10.943	2.189	1.207	1.482	16	0.986	9.00E-04	2 3 4 4 5 5 6 6 7 7 8 8 9 9 10 10
4		8.972	1.95	1.224	1.484	15	0.991	1.00E-03	2 3 3 4 4 5 5 6 6 7 7 8 8 9 9
5		11.112	2.322	1.197	1.484	15	0.998	9.00E-04	3 4 4 5 5 6 6 7 7 8 8 9 9 10 10
6		8.567	2.238	1	1.484	14	0.998	1.20E-03	3 3 4 4 5 5 6 6 7 7 8 8 9 9
7		8.567	2.238	1	1.484	14	0.998	1.20E-03	3 3 4 4 5 5 6 6 7 7 8 8 9 9
8		8.553	2.096	1.186	1.484	13	0.999	1.10E-03	2 3 3 4 4 5 5 6 6 7 7 8 8
9		9.277	1.917	1.112	1.483	13	0.996	1.00E-03	3 4 4 5 5 6 6 7 7 8 8 9 9
10		7.795	2.038	1.128	1.484	12	0.999	1.20E-03	3 3 4 4 5 5 6 6 7 7 8 8
11		8.243	2.227	1.119	1.484	12	0.999	1.20E-03	3 3 4 4 5 5 6 6 7 7 8 8
12		8.459	2.133	1.202	1.484	12	0.999	1.10E-03	3 3 4 4 5 5 6 6 7 7 8 8
13		8.516	2.052	1.224	1.484	12	0.999	1.10E-03	3 3 4 4 5 5 6 6 7 7 8 8
14		8.623	2.225	1.091	1.484	12	0.998	1.10E-03	3 3 4 4 5 5 6 6 7 7 8 8
15		8.727	2.341	1.132	1.484	12	0.999	1.10E-03	3 3 4 4 5 5 6 6 7 7 8 8
16		8.792	1.964	1.164	1.48	12	0.999	1.00E-03	3 3 4 4 5 5 6 6 7 7 8 8
17	Green	1.702	3.127	1.338	1.484	5	0.988	3.10E-03	1 3 3 4 4

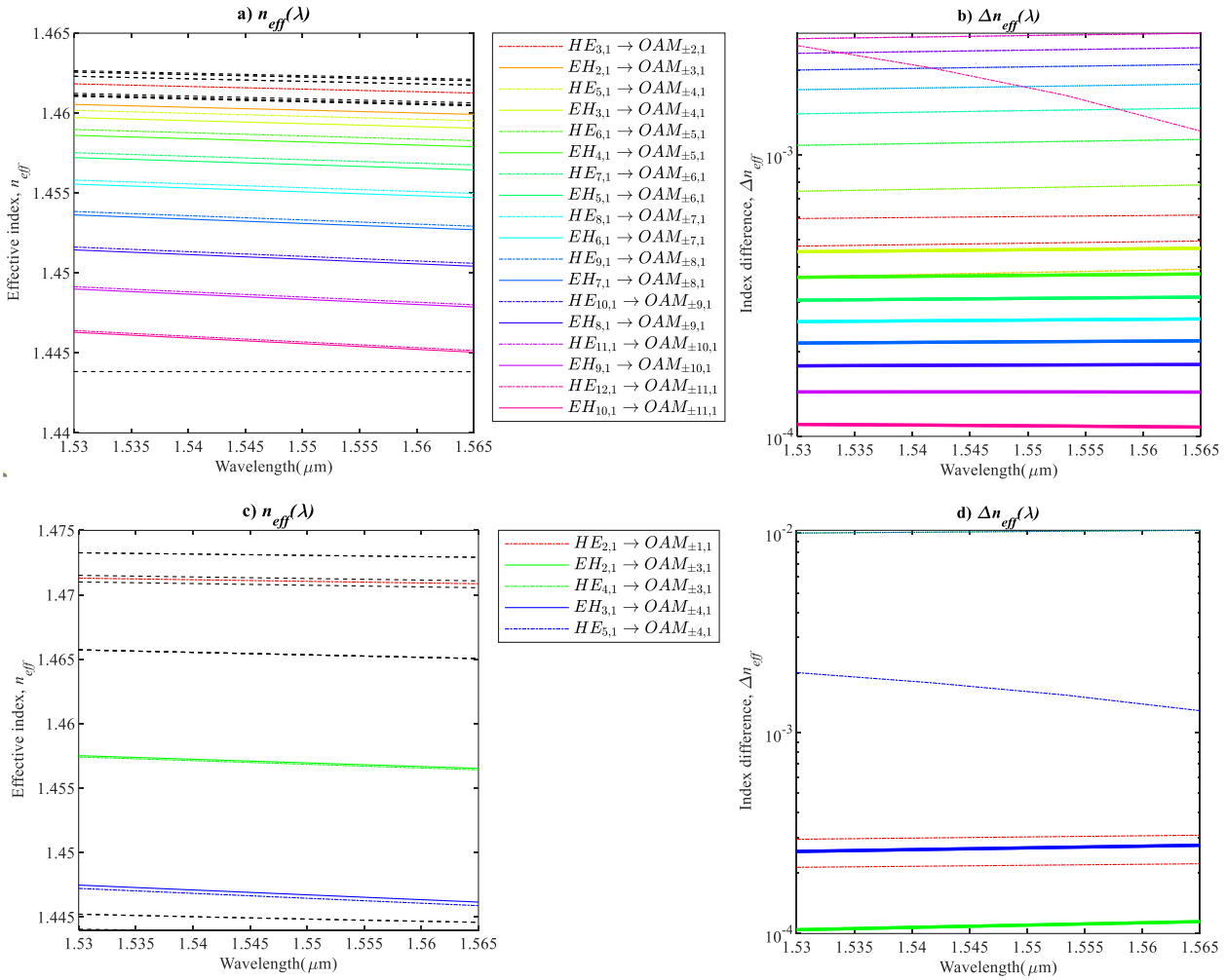

Figure 4-8 a, b) *neff(λ)* and *Δneff(λ)* of the best designs in terms of the number of supported OAM modes (marked with blue color in Figures 4-6 and 4-7). c, d) *neff(λ)* and *Δneff(λ)* of the best designs in terms of *Avg(Δneff)* (marked with green color in Figures 4-6 and 4-7).

4.5 Conclusion

In summary, we have presented a case study on the design of an OAM fiber using frameworks involving single- and multi-objective optimization algorithms. The proposed frameworks can effectively design the cross-section refractive index profile of a newly introduced OAM fiber and optimize the design for any target transmission configuration. No human intervention, simplicity, and straightforward implementation are the advantages of the proposed framework. Moreover, manufacturing constraints and other merit factors can be added to the frameworks in a straightforward fashion. In addition, various optimization algorithms can be easily used to achieve a wide range of optimal designs. Eventually, the proposed framework opens up an effective way of designing high-performance OAM fibers for any target transmission configuration and paves the way for the development of optical communication systems based on OAM-modulation.

Chapter 5: Optimization Frameworks for Designing Photonic Crystal Filters

5.1 Introduction

This chapter is based on the paper published in the Journal of Applied Optics [2]. Recently, Photonic Crystal (PhC) devices attract much attention due to their wide range of applications. The phenomenon of the bandgap of PhC structures and the results of the defect creation in such structures provide the opportunity to manipulate the light for specific purposes. The behavior of light propagation and the modeling of the internal process in such structures are usually very challenging tasks. In addition, such devices are usually designed by human involvement in tedious non-systematics efforts due to the complexity of the relationship between the device output performance and its structural parameters, a large number of structural parameters, and the lack of the analytical method for designing devices [93]–[98].

The focus of this chapter is on PhC filters. PhC ring resonator [99]–[101], PhC cavity [102], and PhC filter based on defect mode [103] are some of the prominent types of such devices. As mentioned above, such devices are usually designed with tedious non-systematics efforts. The main gap in the literature is the lack of a comprehensive and automatic method for designing PhCs filters.

The aim of this chapter is to propose a framework as a steppingstone to fill this gap which assists researchers in designing every kind of PhCs filter considering all issues in optical filters. Our proposed solution to this problem is the use of artificial intelligence techniques to bypass discovering the relationship between the outputs and the structural parameters.

This approach has been followed in the literature as maximizing Quality factor (Q) of PhC cavity [104]–[106], minimizing of bend loss of PhC waveguide [107], designing PhC notch-filter [108], slow light characteristic optimization of PhC waveguides [66]–[71], [109], and PhC LEDs designing [65].

In this chapter, we proposed a novel multi-objective optimization framework for designing any kind of PhC filter. The aim of this framework is to design such devices with considering and handling all the issues in the optical filters designing process. Parameters, Constraints, and Optimizer module are the main parts of this framework. All of the concepts are presented with an example of designing a new six channels Wavelength Division Multiplexer (WDM) with regard to the WDM standard defined by ITU-T Recommendation G.694.2 [103]. Six channels with 20nm channel spacing from 1490~1590nm window are considered in this standard. Also, the maximum deviation of central channel wavelength from the standard defined channel center must not be more than 2nm.

5.2 PhC filter Structure and Related Issues

A leakage mode is generated in the photonic bandgap by introducing defects in a photonic crystal lattice. This leakage mode guides a narrowband of spectral wavelength. Therefore, such structures can be utilized as narrow band filters.

Achieving desirable optical PhC filters is mainly done by designing structural parameters of the defects. It is obvious that the flexibility to manipulate the light of PhC filters is directly related to the pattern and the shape of the defect region. The more rods involved in defect region, the more flexible the PhC filter structure, and the more complexity and difficulty for designing such

structures.

WDM is a bunch of optical filters, which can be assumed as a popular application of optical filters. In this work, we aim to design PhC filters for applications in WDM. The proposed layout of the WDM is shown in Figure 5-1. In order to simplify the process of designing the WDM, we design each filter cell separately. To do so, it is necessary to minimize the effects of adjacent filters. Therefore, in order to minimize such effects, we considered large enough spaces (5 rods) between every two adjacent filters. It is worth mentioning here that the propagation of the electromagnetic wave (light) in such devices follows a complicated behavior. Therefore, the waveguide region must be considered in addition to the filter cell to prepare the similar situation in which the filter cell works (in WDM). In other words, the effect of adjacent filters in WDM must be considered while designing each filter. Hence, if the waveguide region is not considered, the final designed PhC filter will not work properly in its place in the WDM. The final filter cell for separately designing is shown in Figure 5-2.

The PhC lattice consists of pillars of $In_{0.53}Al_{0.16}Ga_{0.31}As$ in air background with the square array pattern. For an incident wavelength at 1.55 μm, the refractive index of $In_{0.53}Al_{0.16}Ga_{0.31}As$ rods is 3.19. The radius of rods of this structure is considered as R=0.185a [103]. The reason for selecting this value is reaching the maximum photonic band gape. Therefore, wider photonic bandgap provides wider operational window of wavelength to be filtered. For the simulation of this device Finite-Difference Time-Domain (FDTD) simulator will be used. Since the optimization process requires an extremely large number of function evaluations (simulations) and 3D simulation is computationally very expensive, it is not reasonable to use 3D FDTD simulations. Instead, 2D FDTD simulations with effective index method [110] and effective period method [111] provide very fast and accurate simulations which reduce the required resources by 2–3 orders of magnitude. The effective period method uses the effective index method in its internal process, so it is a more sophisticated method to estimate actual simulation with 2D simulation.

In the effective period method, the actual value of refractive index will be utilized in 2D simulations. The only thing that is necessary to be modified is the period of the lattice as follows [111]:

$$a_{eff} = \frac{n_{eff}}{n_{bulk}} a \tag{5-1}$$

where a_{eff} is the effective period, n_{eff} indicates the effective index which is calculated by effective index method of [110], n_{bulk} signifies the refractive index of bulk, and a shows the period or lattice constant.

The height of the rods is considered as 400 nm, which gives $n_{eff} = 2.89$. Since the central normalized frequency of photonic bandgap placed on 0.389, the lattice constant is $a = 0.389 * 1550 = 603\ nm$. As such, $a_{eff} = \frac{2.89}{3.19} * 603 = 546\ nm$. Overall, the device simulations will be done by considering the actual value of refractive indexes and a_{eff} of $546\ nm$ during 2D FDTD simulations.

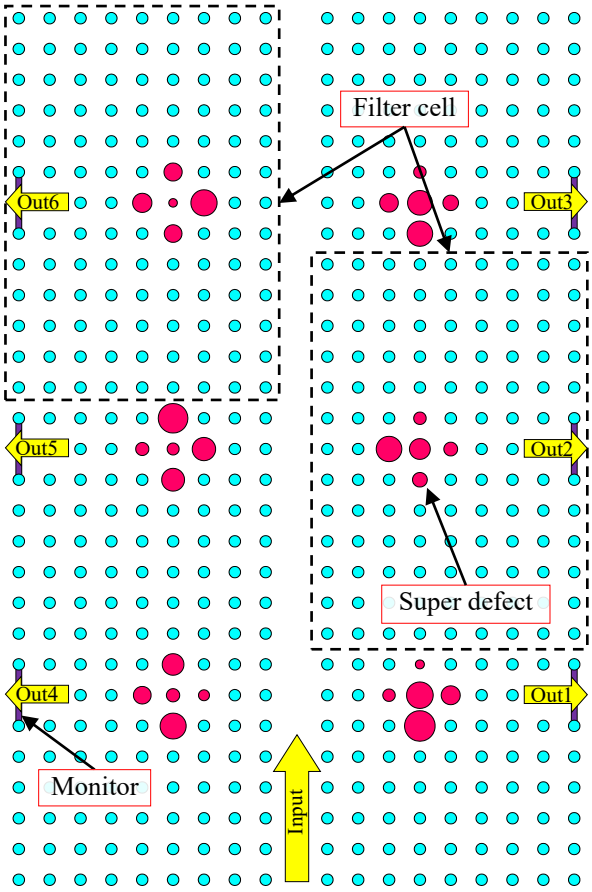

Figure 5-1 The proposed WDM layout.

The output spectral transmission performance of a sample case is calculated by FDTD simulation for TM-polarization (the electric filed parallels the rod axis) and shown in Figure 5-3. In order to prepare the PhC filter designing problem for multi-objective optimization, three merit factors are defined as follows [62]:

- Amp_c indicates the maximum amplitude of filter output in channel range
- Amp_s represents the maximum amplitude of filter output in the WDM working bandwidth (1480-1600nm) outside the channel region.
- *Deviation* represents as the absolute value of subtraction of central wavelength of the output filter peak (λ_C) to the defined central wavelength of channel (λ_O) ($Deviation = |\lambda_C - \lambda_O|$).

Amp_c, Amp_s and *Deviation* are illustrated in Figure 5-3.

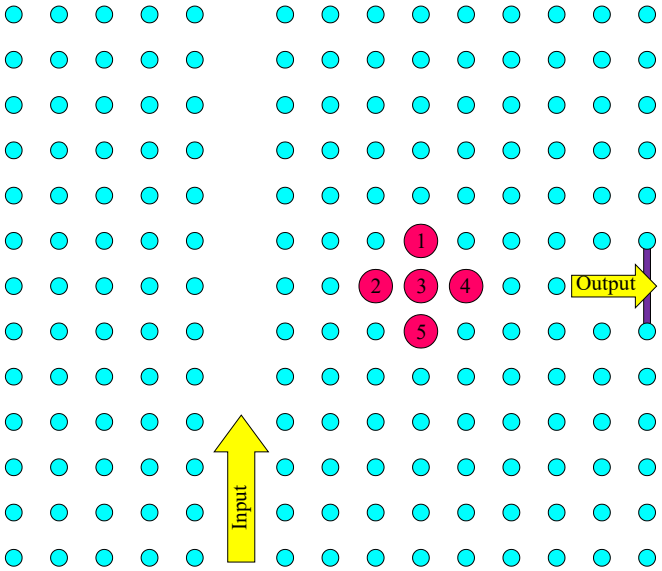

Figure 5-2 Proposed PhC filter according to super defect structure with waveguide. The radii of defect rods considered as the structural parameters.

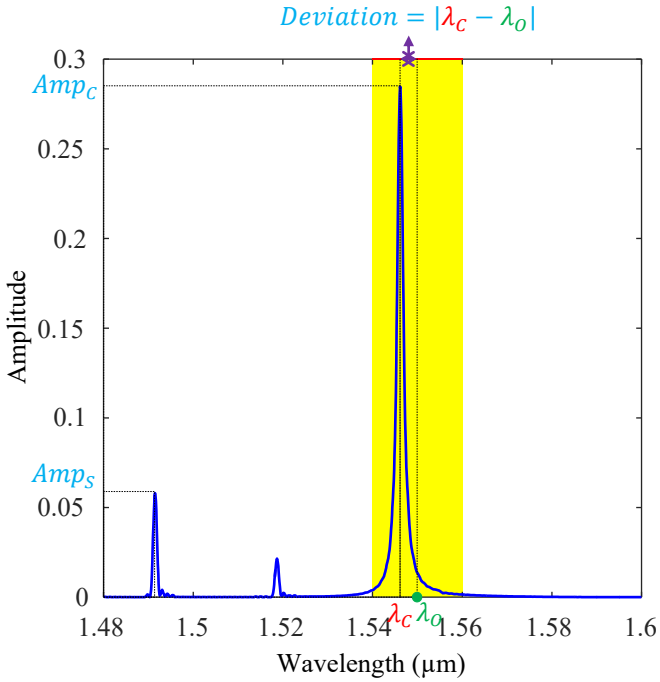

Figure 5-3 The output spectral transmission performance of a sample case of PhC filter.

5.3 Single- and multi-objective optimization frameworks for designing PhC filters

The main idea of obtaining optimal PhC filter designs is to propose a PhC filter structure in which Amp_c is maximized while Amp_s and *Deviation* are minimized. Due to the complexity of the relationship between the merit factors and structural parameters, proposing analytical methods for designing such devices is very difficult, and in some cases, it is almost impossible to achieve. This is the reason why we develop a multi-objective framework which finds optimum PhC filters without human involvement. This framework consists of three main modules as follows (Figure 5-4):

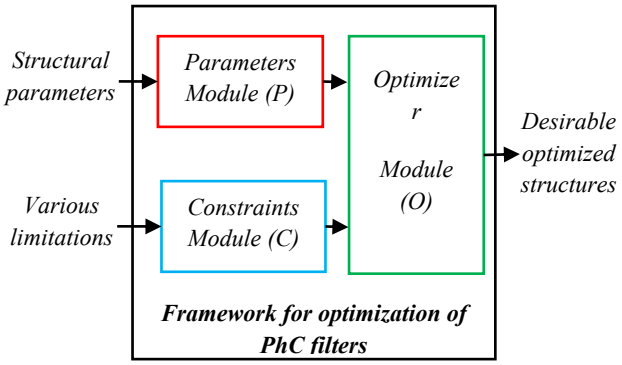

Figure 5-4 Proposed single- and multi-objective optimization frameworks for designing PhC filters.

A. Parameters Module (P)

In this module structural parameters are defined and handled. In other words, all of the structural parameters, which the best values for them will be found, must be identified in this module. The P modules for this super defect PhC filter (Figure 5-2) is as follows:

$$P: \vec{x} = \left[\frac{R_1}{a}, \frac{R_2}{a}, \frac{R_3}{a}, \frac{R_4}{a}, \frac{R_5}{a}\right] \tag{5-2}$$

B. Constraints Module (C)

Most of the issues in the process of PhC filter designing are considered in this module. Three groups of constraints are considered here to address such issues: parameters range (C_1), Amp_s limitation (C_2), and Deviation limitation (C_3). The first set of constraints indicates the manufacturing limitations and structural parameters ranges, the second constraint is for legitimating narrow band filtering operations, and the third constraint is applied for handling Deviation safe interval. The C module for the proposed super defect filter cell (Figure 5-2) is as follows:

$$\begin{gathered} C = [C_1, C_2, C_3], \\ C_1: 0 \le \frac{R_1}{a}, \dots, \frac{R_5}{a} \le 0.5, \\ C_2: Amp_s < Amp_c\,, \\ C_3: Deviation \le 2\ nm \end{gathered} \tag{5-3}$$

C. Optimizer Module (O)

Two components should be identified for O module: objective functions and optimizer. The objective function for the single objective optimizer is the combination of the merit factors as $Objective = \frac{Amp_C}{Amp_S + Deviation}$ [62]. The optimizer should maximize this aggregated objective function in order to achieve a high performance PhC filter. Optimization with respect to this objective causes some issues described in the next section.

The objective functions for the multi-objective optimizer are Amp_c, Amp_s and *Deviation*. The optimizer should find the PhC filter structures in which Amp_c is maximized while Amp_s and *Deviation* are minimized.

Diverse optimization techniques can be used in the optimizer component [22], [89], [90]. We

choose the single and multi-objective version of the Grey Wolf Optimizer (GWO) algorithm for the optimizer [21], [24], [91]. This algorithm mimics the leadership and social behavior of grey wolves in nature and proves its performance in different fields of engineering. Our main motivation to choose this algorithm is the high local optima avoidance. Since the problem investigated in this work has a large number of variables, the search space is very difficult to explore and there is a lot of local solutions.

Note that multi-objective problems have more than one objective function. Due to the nature of such problems, there is no single solution for them. Instead, a set of optimal solutions called the Pareto-optimal set is the answer of multi-objective problems, representing the best trade-offs between multiple objectives [73].

5.4 Results and discussion

After setting up each module, the single- and multi-objective frameworks are ready to optimize the structures of the proposed PhC filter. Technically speaking, the optimizer systematically checks different possible combination of variables in order to achieve high performance design(s).

Single objective optimization scheme:

The aim of this optimization process is to maximize the $Objective = \frac{Amp_C}{Amp_S+Deviation}$. As the Amp_C increases and the Amp_S+$Deviation$ decreases, $Objective$ increases. To achieve a high performance PhC filter, therefore, optimizer simply considers $Objective$ as the objective function and tries to find its maximum value.

We utilized single-objective version of GWO with 24 artificial gray wolves during the 400 iterations to approximate the global optimum for this problem. The results of GWO are shown in Table 5-1. In this table Q represents the quality factor and calculates as $Q = \lambda_0/\Delta\lambda$. The high value of Qs indicates that the optimal design satisfies the conventional merit factor (Q) as well as our merit factors ($Objective$). The convergence curve and the output spectral transmission performance of the PhC filters of Table 5-1 are shown in Figure 5-5 and Figure 5-6.

Convergence curve is a very common tool to qualitatively present results of a single-objective optimization algorithm. This curve shows that the best design is found up to an iteration. In other words, GWO starts searching for the best design with random initialization. In iteration 1, it found a design with Objective=0.198. It continued searching to find a better design. During iterations 2 to 23, GWO did not find a better design in terms of Objective. In iteration 24, a design with Objective=0.242 has been found. Therefore, GWO continues searching until the iteration 197. In that iteration a design with Objective=7.014 was found. After that, between iteration 198 to 400, no better design has found. It shows that we can be confident that the best design with respect to merit factor of Objective has found. If you wonder why the convergence curve remains constant for a certain number of iteration, this is because of the stochastic nature of GWO and other similar algorithms. The random changes in the solutions periodically increase to avoid entrapping of the algorithm in local solutions. For search space with many local solutions, such techniques never show a constant drop or climb in the convergence curve.

Table 5-1 Properties of obtained structures during single-objective optimization

Iter	R_1	R_2	R_3	R_4	R_5	Amp_c	Amp_s	$D(nm)$	*Objective*	*Q*
1	105	237	205	236	64	0.176	0.0017	0.886	0.198	1017
24	9	197	204	168	267	0.1	0.0023	0.409	0.242	678
25	85	243	195	272	101	0.197	0.0019	0.257	0.759	1018
49	146	141	272	52	56	0.144	0.0089	0.028	3.911	957
197	142	147	168	20	57	0.202	0.0008	0.028	7.014	1163

Unit of R_x is *nm*.

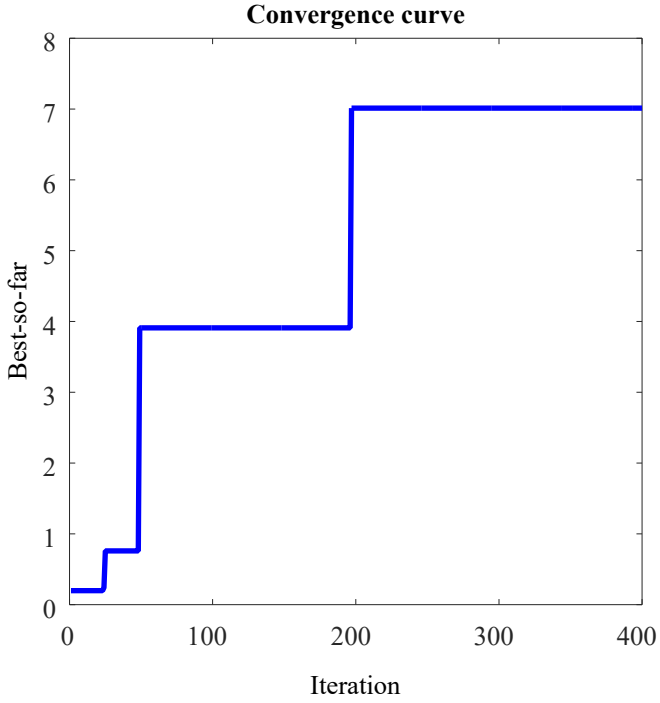

Figure 5-5 Convergence curve of single-objective optimization of the PhC filter.

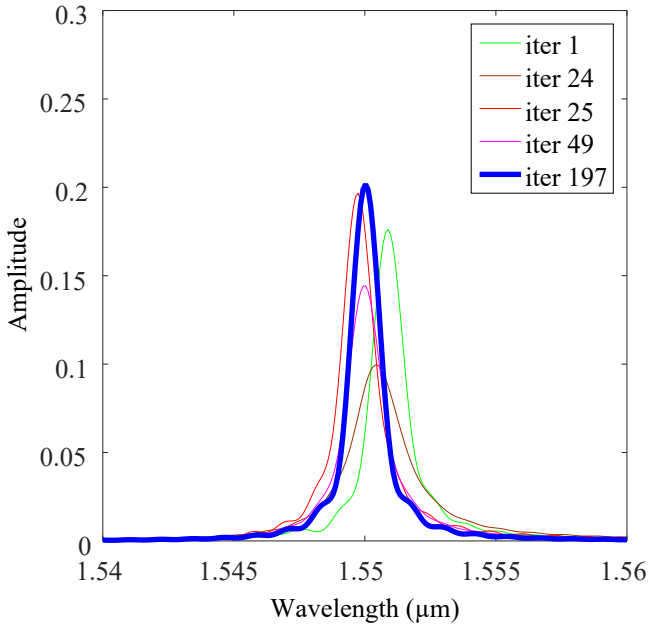

Figure 5-6 The output spectral transmission performance of the PhC filter designs of Table 5-1.

Multi objective optimization scheme:

The conflicting behavior of the Amp_c, Amp_s and *Deviation* shows that this problem is intrinsically multi-objective. As mentioned before, there is no single solution for a multi-objective problem, therefore a set of optimum solutions representing the best trade-offs between multiple objectives is the answer to these problems. Combining these merit factors and solving the problem with the single objective optimization approach results in finding only a member of the set of optimal solutions. It is worth mentioning here that all the members of the set of optimal solutions are the best optimal designs and no one is better than others when considering multiple objectives. A good analogy is to purchase a laptop. Two objectives would be performance and price. A laptop that has high performance but more expensive is not better than a laptop with low performance but cheap. If we consider either performance or price, we can say one of those laptops are better. However, both laptops are good when considering two objectives. It is worth noting here that a laptop of low performance and expensive is definitely worse than the other two. Further explanation about the set of optimum solutions is provided in the next paragraph.

Multi-objective version of GWO with 72 artificial gray wolves and 200 iterations are utilized here to find the set of optimum solutions. MOGWO managed to find 54 optimal designs at the end of optimization process. The search history of multi objective optimization and Pareto front (Pareto optimal solution) are depicted in Figure 5-7 and 5-8. In order to justify these results, the characteristics of some of the designs presented in Figure 5-7 and 5-8 are shown in Table 5-2 and their output spectral transmission performances are plotted in Figure 5-9. The comparison of the Pareto optimal solutions (Figure 5-8) and the optimal design which was found by-single objective approach indicates that the optimization with respect to a single objective approach results in loosing of many decent designs which are suitable for specific applications. The high value of Qs of the designs also indicates that the obtained designs satisfy the conventional merit factor (Q).

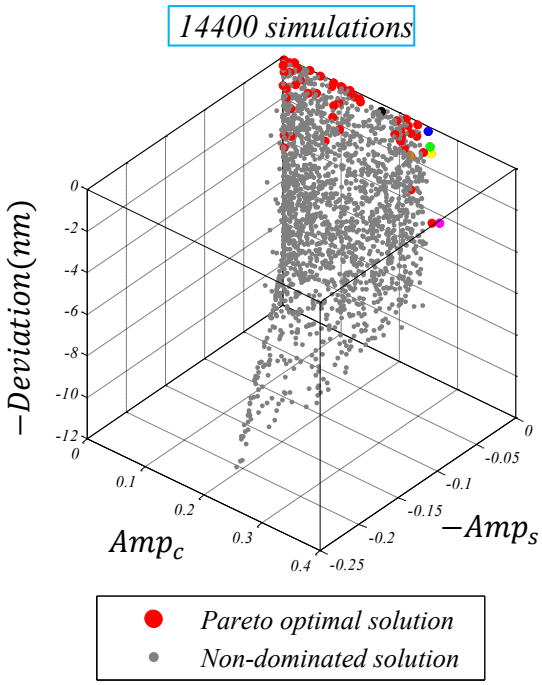

Figure 5-7 Search history of multi objective optimization with some marked designs.

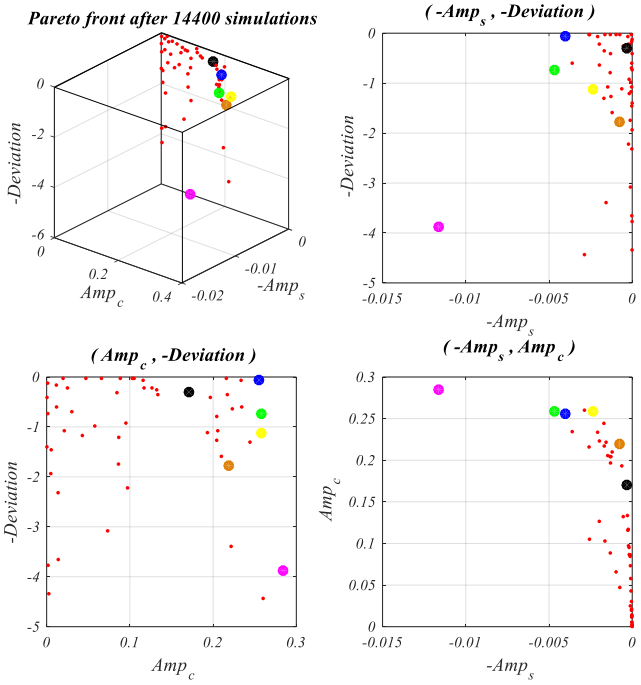

Figure 5-8 The Pareto front (Pareto optimal solution) of multi objective optimization approach with some marked designs.

Table 5-2 Optimum structures of multi-objective optimization approach which are marked in Figure 5-7 and 5-8.

Label	R_1	R_2	R_3	R_4	R_5	Amp_c	Amp_s	$D(nm)$	Q
S1	168	174	119	180	47	0.285	0.0116	3.866	858
S2	79	195	58	172	71	0.258	0.0023	1.114	905
S3	126	175	66	185	76	0.258	0.0047	0.733	856
S4	172	175	87	181	85	0.255	0.004	0.067	708
S5	76	207	57	173	69	0.219	0.0008	1.779	1086
S6	112	204	66	173	58	0.17	0.0004	0.314	1252

Unit of R_x is *nm*.

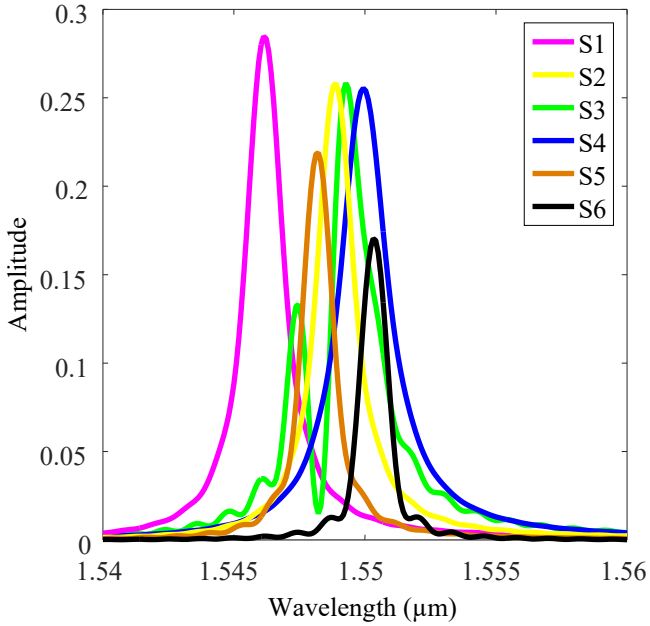

Figure 5-9 The output spectral transmission performance of the PhC filter designs of Table 5-2.

5.5 Wavelength division multiplexer (WDM) designing by using optimal filter cells

We have utilized the multi-objective approach for designing the other 5 channel of utilized WDM standard [103]. After finding the set of optimum solutions, the next step toward the WDM designing is to select a design of each channel. Hence, the similar structures in terms of Amp_c were chosen. Finally, six selected design are placed side by side to implement the desirable WDM. The characteristics of the designed WDM with optimal filter cells is shown in Table 5-3. The structure and the output spectral transmission performance are also shown in Figure 5-10 and 5-11.

Table 5-3 shows that the Amp_ss are very low. It shows that cross talk of this WDM is very low (-35.1dB) in the worst case. In addition, very low *Deviation* values of all channels shows the λ_C is located correctly. In addition, the magnitudes of Q factors are so high which indicates that the designed WDM satisfies the conventional merit factor. Overall, the substantial characteristics prove that the WDM is well designed and totally matched up with the corresponding WDM standard (ITU-T Recommendation G.694.2 [103]).

The comparative study in Figure 5-11 shows that the WDM obtained using the multi-objective approach has a higher overall performance compared to the similar designs in term of utilized WDM standard in [103] and [62]. Note that all of the three structures in this figure were

stimulated with the same input power. The advantages of the proposed method in this study, which result in having the higher performance design, are because of two reasons. The first reason is due to the use of the super defect instead of a simple defect to provide much flexibility in manipulating the guided light through the defect. The second reason is to utilize the systematic multi-objective optimization method to find the suitable design for each channel.

All in all, the multi-objective optimization technique is an easy and comprehensive method for designing the complex super defect PhC filters with a large number of structural parameters. Furthermore, this method opens up a way towards designing complicated and very high performance PhC filters, which is almost impossible to achieve by the current try and error process.

The Designed WDM in Table 5-3 requires a *1 nm* manufacturing resolution. Based on the fabrication process of photonic crystal structures which was reported in [112], [113], it can be stated that this structure is feasible to build considering the current fabrication process. To investigate the influence of some fabrication tolerances, 100 random values between [-1nm, 1nm] are added to the radiuses in 100 independent simulations. The calculated results showed that the average of Amp_cs, maximum of deviations and worst case Cross talks are still good enough to rest assure that the fabricated device works properly. The output spectral transmission performance of these simulations are shown in Figure 5-12.

Table 5-3 Calculated properties of the designed WDM with optimal filter cells.

channel #	R_1	R_2	R_3	R_4	R_5	Amp_c	Amp_s	$D(nm)$	Q
1	111	172	124	161	139	3.71	0.01	0.39	1731
2	128	166	155	163	117	5.18	0.02	0.69	1232
3	131	154	183	67	131	5.15	0.02	0.66	1413
4	172	175	87	181	85	4.81	0.13	0.09	759
5	158	168	202	205	41	6.38	0.09	0.33	761
6	197	119	143	193	87	6.2	0.02	0.02	1258

The unit of R_x is *nm*.

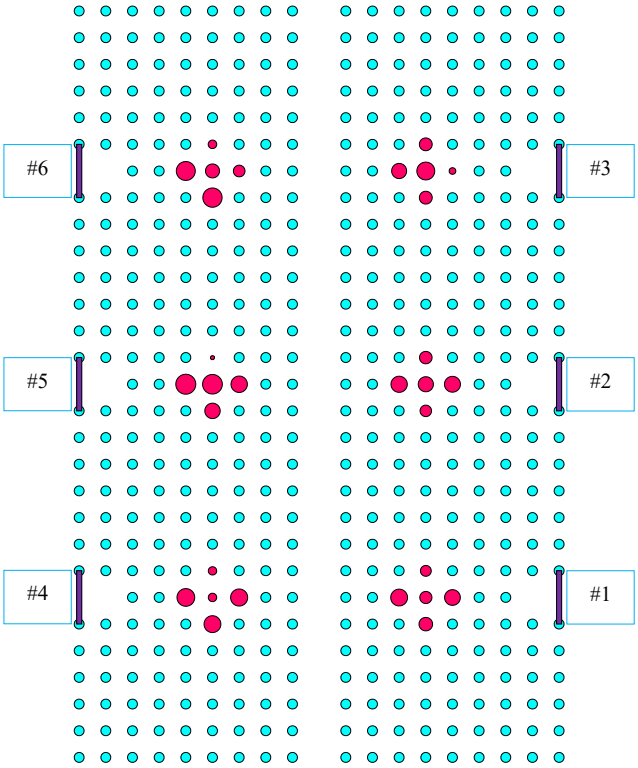

Figure 5-10 The WDM designed with optimal filter cells.

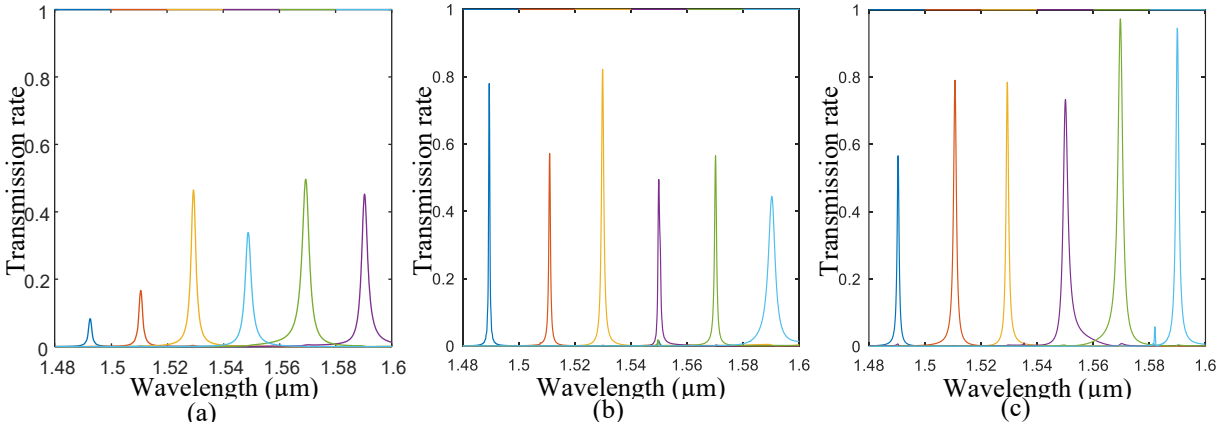

Figure 5-11 The output spectral transmission performance of the WDM structure in [103] (a), Designed WDM by the single-objective approach in [62] (b) and this work (c). Note that all structures are simulated with the same input power.

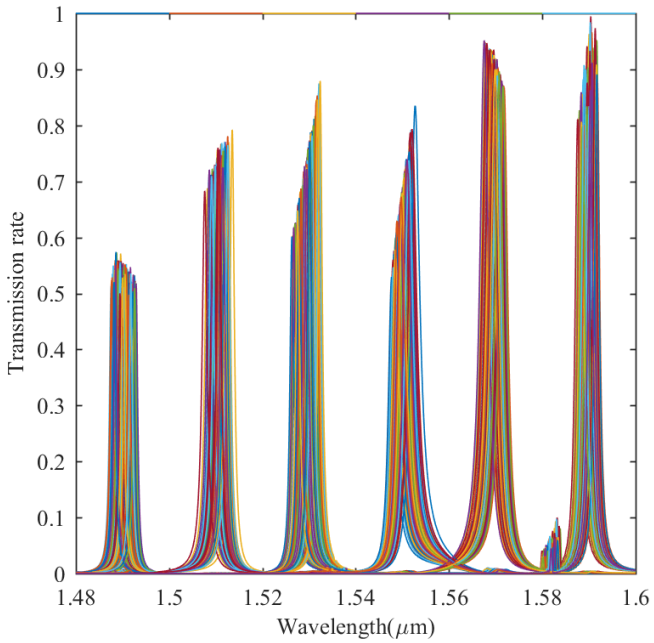

Figure 5-12 The output spectral transmission performance of the designed WDM during the 100 simulations in which the structural parameters fluctuated randomly.

5.6 Conclusion

In summary, the case study investigated showed that the proposed multi-objective framework is able to effectively design and optimize the structure of the newly introduced PhC filter in this chapter. The proposed framework is also applicable to any kind of complicated super defect PhC filters. Different structures can be formulated and designed with respect to any filter standard. This method does not require human involvement to provide an initial design to start the optimization. Moreover, there is the possibility to add any manufacturing limitation in the C module. Various multi-objective algorithms can be easily utilized to implement the optimizer module in order to achieve a wide range of optimal designs. Finally, the proposed multi-objective framework opens up an effective way for designing WDM filter cells with respect to any WDM standards.

Chapter 6: Radiation Pattern Design of Photonic Crystal LED optimized by using Multi-objective Grey Wolf Optimizer

6.1 Introduction

This chapter is based on the paper published in the Journal of Photonic Network Communications [3]. To date, Photonic Crystal (PhC) structures cover a wide range of applications in the field of optics and photonics. An interesting application of such a structure is enhancing the performance of Light-Emitting Diodes (LED). In LED devices, the generated light in the active region must be extracted from the device as much as possible. That is to say, an LED without a well-designed guiding path of generated photons does not show a significant irradiance. There are some works in the literature on increasing the Extraction Ratio (*ER*) of LEDs by using a Photonic Crystal (PhC) slab [114]–[116], in which a PhC layer is placed in the top of active regions to enhance the ER. The complex, often ill-defined relationship between the structural parameters and the device output has prevented researchers from suggesting the analytical method for designing the PhC layer. Due to the lack of an analytical method for designing PhC layer, therefore, the PhC layers have been designed manually by trial and error techniques. This drawback has been tackled and alleviated in 2015 [65], where a multi-objective artificial intelligence optimizer was used to maximize the *ER* and Purcell Factor (*PF*) of PhC LED. In fact, the process of discovering the relation between the structural parameters and the device outputs was bypassed. The results of this study showed that a multi-objective optimizer is able to find optimal designs for PhC LEDs as far as *ER* and *PF* are concerned.

Although by the aforementioned approach PhC LEDs can be designed, another issue is not considered; the radiation pattern of final optimal designs shows a dissipate distribution of light intensity. Hence, optimization with considering just *ER* and *PF* does not ensure controlling the shape of the radiation pattern. This motivated our attempt to propose an optimization framework for shaping the radiation pattern for specific applications in this work. The rest of this chapter is organized as follows:

Section 6.2 explains the PhC structure and related issues which should be considered during the designing process. In Section 6.3, the problem formulation for the radiation pattern shaping of PhC LEDs is described. The results of optimization on the case study PhC LED are provided in Section 6.4. Finally, Section 6.5 concludes the work.

6.2 PhC LED Structure and Related Issues:

The case study (see Figure 6-1) investigated here is the green PhC LED (520*nm*). In order to increase the flexibility of the structure to guide the generated light, it is necessary to have a large number of structural parameters. Therefore, we have considered each section independent with a unique structural parameter. The reason why we considered a symmetrical structure is that we want to design an LED in which the output radiation pattern has a symmetrical form. So, the symmetrical structure provides such a desired output. In addition, by using a symmetrical device, just half of the device can be simulated. It significantly reduces the simulation time and speeds up the optimization process.

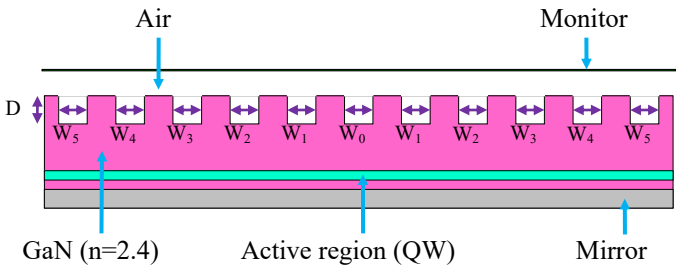

Figure 6-1 1D PhC LED structure which is utilized as a case study. The thickness of the top, active region, and bottom layer are 0.85, 0.7, and 0.15 μm.

The PhC layer of the case study consists of seven independent structural parameters ($W_{0\text{-}5}$ and Depth). It is worth mentioning that most of PhC LED designs use equal values of W_0-W_5, but the modeling method of this chapter considered a situation where W_0-W_5 are different. The reason why we considered such situation is that in order to increase the flexibility of the structure to guide the generated light, it is necessary to have a large number of structural parameters which can be tuned separately. In other words, we want to shape the radiation pattern. Therefore, by using equal values of W_0-W_5, there is not enough flexibility to manipulate the structural parameters and shape the radiation pattern.

The separation of the grating (*Period*) is 0.6 μm. For manipulating the light within a photonic crystal structure, the value of structural parameters must be in the same order of light wavelength. Since we want to provide a comparative study to justify the performance of the proposed method, the structure proposed in [116] is used as the case study. Generally, the separation of the grating can be defined as an independent structural parameter. Therefore, the optimization framework will find its optimal value.

The existing analytical methods for gratings in such structures are not robust enough to perform the optimization. This is mainly because the structure under study is a non-uniform and non-periodic grating. In order to simulate the unpolarized and incoherent behavior of the generated light in the active region, eleven incoherent dipole sources are considered within the active region [117], [118]. They are placed directly below the grating. The results of three coherent FDTD simulations in the three orthogonal directions for each dipole are incoherently combined together. Therefore, the eleven sets of results which correspond to eleven dipoles are incoherently combined together. By doing so, the intrinsic behavior of the incoherent generated light in the active region will be simulated. Therefore, the light source which is utilized to simulate the LED is a narrow bandwidth Gaussian pulse centered on the wavelength of 520nm. This light source corresponds to the generated green light of PhC LED. Basically, simulations have been done for a wide range of wavelengths, whereas the analysis of the LED has been done for the visible wavelength range (400-700 nm). Note that a homogeneous refractive index is assumed in the LED. In addition, the condition of the bottom boundary is Perfect Electric Conductor (PEC) to model the mirror, and the rest are Perfectly Matched Layer (PML).

The radiation pattern of the three sample cases is shown in Figure 6-2. As mentioned before, optimization with considering just ER and PF does not provide any control to shape the radiation pattern. Therefore, the process of formulating the device designing problem is provided in the next section.

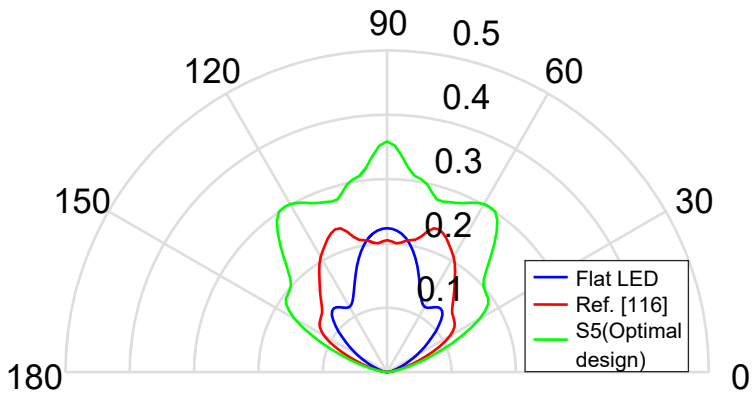

Figure 6-2 Radiation pattern of three designs of the structure which is shown in Figure 6-1. The flat LED ($W_{0\text{-}5}$ and $Depth=0$), structure propose in [116], and optimal design (S5) in [65].

6.3 Problem formulation for the radiation pattern shaping:

The problem formulation is divided into three main phases: variable identification, constraint identification, and optimizer phase. As its name implies, the variable identification phase finds the structural parameters of the PhC layer of the LED. The constraint identification phase identifies the constraints applied to the range of the structural parameters and the fabrication limitations. The optimizer phase consists of two sections: multi-objective cost (objective) function and multi-objective optimizer. The first aim of radiation pattern shaping is focusing the intensity of LED light on a narrow-angle range. Therefore, there are two objectives to be optimized. The intensity of the radiated light in the range of θ degree must be maximized, while the intensity of the radiated light outside the range of θ degree must be minimized simultaneously. After defining the multi-objective cost function, the multi-objective optimizer will be utilized to find optimal designs. In this chapter, the Multi-Objective version of Gray Wolf Optimizer (MOGWO) will be utilized to shape the PhC LED radiation pattern [24]. Therefore, the problem formulation for the case study which is shown in Figure 6-1 is as follows.

$$Variables: \vec{x} = [x_1, x_2, x_3, x_4, x_5, x_6, x_7] = [W_0, W_1, W_2, W_3, W_4, W_5, Depth]$$
$$Objectives: Maximize(Avg_C), Minimize(Avg_S)$$

Where:

$$Avg_C = \frac{1}{\theta}\int_{\frac{\pi}{2}-\frac{\theta}{2}}^{\frac{\pi}{2}+\frac{\theta}{2}} I(\alpha)\, d\alpha :$$
$$(The\ average\ intensity\ of\ center)$$
$$Avg_S = \frac{1}{\frac{\pi}{2}-\frac{\theta}{2}}\int_{0}^{\frac{\pi}{2}-\frac{\theta}{2}} I(\alpha)\, d\alpha + \frac{1}{\frac{\pi}{2}-\frac{\theta}{2}}\int_{\frac{\pi}{2}+\frac{\theta}{2}}^{\pi} I(\alpha)\, d\alpha : \quad (6\text{-}1)$$
$$(The\ average\ intensity\ of\ side)$$
$$I(\alpha): The\ intensity\ of\ radiated\ led\ light\ from\ the\ PhC\ layer$$
$$Variable\ range: 0 \le x_{1-7} \le 600\ nm$$

The optimizer considers the problem as a black box and checks some combinations of the variables to find the optimal designs. For the optimizer, a wide range of optimizers can also be utilized [89], [119], [120].

In the literature, the use of artificial intelligence techniques for designing PhC devices has been also examined. Some of the seminal works are: PhC filters are designed [2], [62], PhC liquid sensors are optimized [6], large mode area PhC fibers are optimized [4], Quality factor of a PhC cavity is maximized [104]–[106], [121]–[125] , bend loss of a PhC waveguide is minimized [107], a PhC notch-filter is designed [108], and slow light characteristic of PhC waveguides is optimized [66]–[71], [126], [127]. Also, waveguide-based LP_{01}–LP_{0m} mode converters are designed with similar approach [5].

In the next section, the results of six optimization scenarios on the PhC LED case study are provided.

6.4 Results and discussion:

The problem of shaping the radiation pattern of a PhC LED is solved in six scenarios as follows:

Scenario 1:

The MOGWO with 60 artificial gray wolves, archive size of 100, and the 80 iterations is utilized. For the first scenario, we have considered $\theta = \frac{\pi}{3}$ and *Period*=0.6 μm. Therefore, after 4800 simulations MOGWO found 69 optimal solutions as shown in Figure 6-3. Note that there is not a single solution for multi-objective problems. Instead, the answer of such a problem is a set of optimal solutions representing the best tradeoffs between the objectives. Therefore, MOGWO found the set of optimum solutions. In Figure 6-3, each point corresponds to an evaluated PhC LED design. The Pareto optimal solutions (red dots) are the best designs found during the optimization. The properties and radiation patterns of the highlighted designs of Figure 6-3 are shown in Table 6-1 and Figure 6-4.

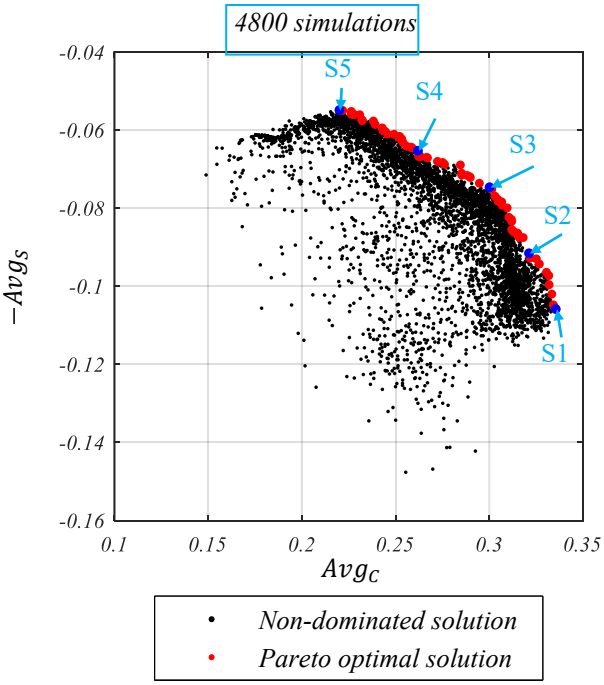

Figure 6-3 Search history of MOGWO after 4800 simulations (scenario 1: $\theta = \frac{\pi}{3}$).

Table 6-1 The characteristics of the highlighted PhC LED designs of Figure 6-3 (scenario 1).

Label	D	W_0	W_1	W_2	W_3	W_4	W_5	Avg_C	$-Avg_S$
S1	267	0	188	242	330	310	350	0.335	-0.106
S2	193	0	258	314	380	350	336	0.321	-0.092
S3	124	0	330	59	591	509	141	0.3	-0.075
S4	102	0	343	0	540	517	47	0.262	-0.065
S5	52	0	456	0	502	600	39	0.22	-0.055

Unit of width$_x$ (Wx) and depth (D) are nanometers.

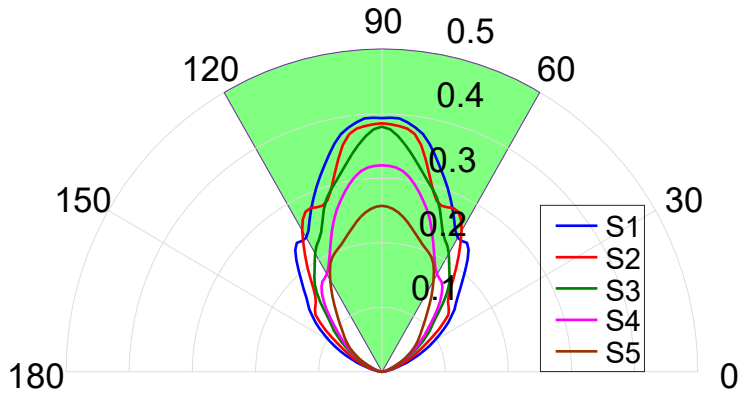

Figure 6-4 Radiation pattern of the highlighted PhC LED designs of Figure 6-3 (scenario 1).

Scenario 2:

For the next scenario, we decrease the θ to $\theta = \frac{\pi}{6}$. After 4800 simulations MOGWO found 57 optimal designs. The search history of this scenario is shown in Figure 6-5 and the properties and radiation patterns of some highlighted designs are provided in Table 6-2 and Figure 6-6.

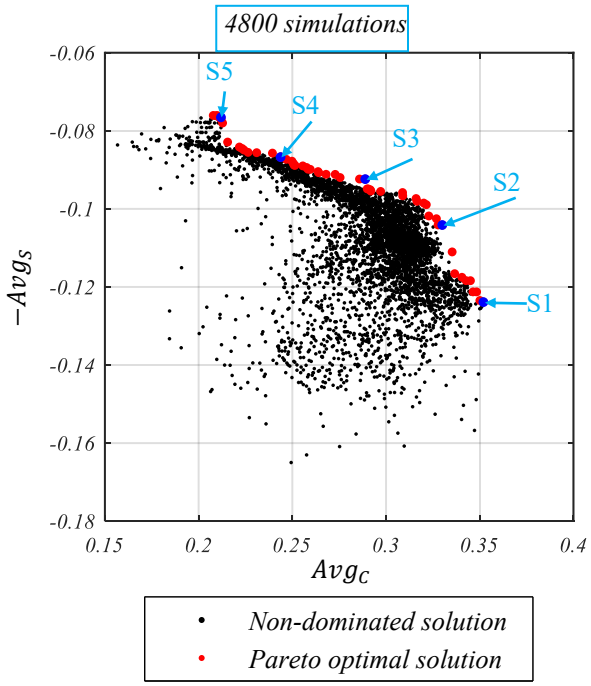

Figure 6-5 Search history of MOGWO after 4800 simulations (scenario 2: $\theta = \frac{\pi}{6}$).

Table 6-2 The characteristics of the highlighted PhC LED designs of Figure 6-5 (scenario 2).

Label	D	W_0	W_1	W_2	W_3	W_4	W_5	Avg_C	$-Avg_S$
S1	200	186	301	209	312	334	214	0.352	-0.124
S2	107	0	487	404	107	350	366	0.33	-0.104
S3	93	46	531	430	20	459	423	0.289	-0.092
S4	47	0	551	426	62	432	343	0.244	-0.087
S5	5	2	500	409	116	422	319	0.212	-0.077

Unit of width$_x$ (Wx) and depth (D) are nanometers.

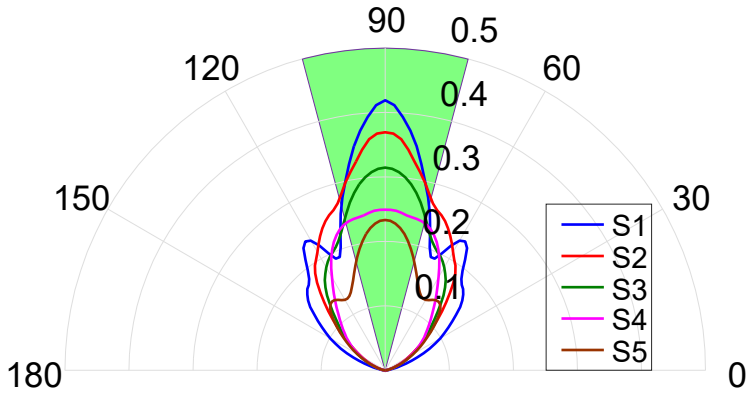

Figure 6-6 Radiation pattern of the highlighted PhC LED designs of Figure. 6-6 (scenario 2).

Scenario 3:

In addition to radiation pattern focusing, the uniformity of the radiated light within the θ angle is also very important for application of reading lamp. For this application, we changed the second cost function. Hence, a new merit factor is defined as $Deviation = \max(I(\alpha)) - \min(I(\alpha))$ within the range of $\frac{\pi}{2} - \frac{\theta}{2} \leq \alpha \leq \frac{\pi}{2} + \frac{\theta}{2}$. After 4800 simulations, MOGWO found 36 optimal PhC LED designs. The search history of this scenario for $\theta = \frac{\pi}{3}$ is shown in Figure 6-7 and the characteristics and radiation patterns of some highlighted designs are provided in Table 6-3 and Figure 6-8.

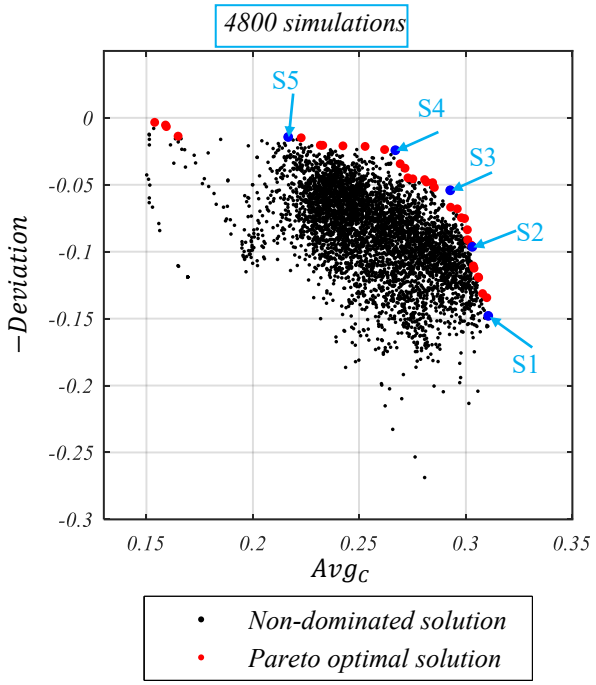

Figure 6-7 Search history of MOGWO after 4800 simulations for uniform radiation intensity in $\theta = \frac{\pi}{3}$ (scenario 3).

Table 6-3 The characteristics of the highlighted PhC LED designs of Figure 6-7 (scenario 3).

Label	D	W_0	W_1	W_2	W_3	W_4	W_5	Avg_C	$-Deviation$
S1	306	473	70	379	211	362	476	0.31	-0.148
S2	305	474	110	338	213	324	472	0.303	-0.096
S3	313	456	118	334	181	294	392	0.293	-0.054
S4	304	378	188	292	271	225	284	0.267	-0.024
S5	388	512	468	286	414	386	254	0.217	-0.014

Unit of width$_x$ (Wx) and depth (D) are nanometers.

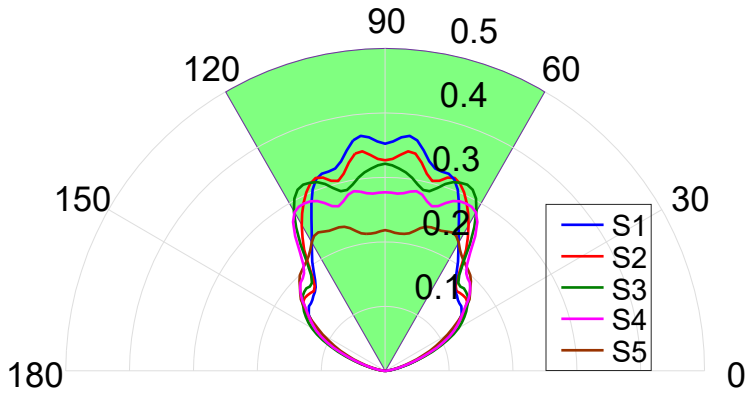

Figure 6-8 Radiation pattern of the highlighted PhC LED designs of Figure 6-7 (scenario 3).

To see the effect of variation of the grating separation, this parameter is also considered as an independent variable (*Period*). Therefore, we have repeated the three previous scenarios as follows:

Scenario 4:

As it was mentioned before, for manipulating the light within a photonic crystal structure, the value of structural parameters must be in the same order of light wavelength. Therefore, we consider the range of 0.1 to 1μm for the *Period*. This range is large enough to provide a wide range of choices for the optimizer. Hence the optimizer decides which value(s) will provide a higher output performance. We have repeated the scenario 1 in which we want to maximize the Avg_c and minimize the Avg_s with the $\theta = \frac{\pi}{3}$. The variables and their ranges are as follows:

$$\begin{aligned} Variables: \vec{x} &= [x_1, x_2, x_3, x_4, x_5, x_6, x_7, x_8] \\ &= \left[Period, \frac{W_0}{Period}, \frac{W_1}{Period}, \frac{W_2}{Period}, \frac{W_3}{Period}, \frac{W_4}{Period}, \frac{W_5}{Period}, Depth\right] \\ Variable\ range: & \ 100 \le x_1 \le 1000\ nm, \\ & \ 0 \le x_{2-7} \le 1, \\ & \ 0 \le x_8 \le 600\ nm \end{aligned} \quad (6\text{-}2)$$

Note that we consider normalized values ($\frac{W_{0-5}}{Period}$) to provide the size of the grooves.

MOGWO found 38 optimal designs as shown in Figure 6-9. In this figure, the Pareto optimal solutions of the previous optimization with constant *Period*=0.6 μm are also depicted for comparison. It is evident that the results of involving *Period* in the optimization show much higher performances with respect to defined merit factors (Avg_c and Avg_s). The properties and radiation patterns of some highlighted designs of Figure 6-9 are provided in Table 6-4 and Figure 6-10.

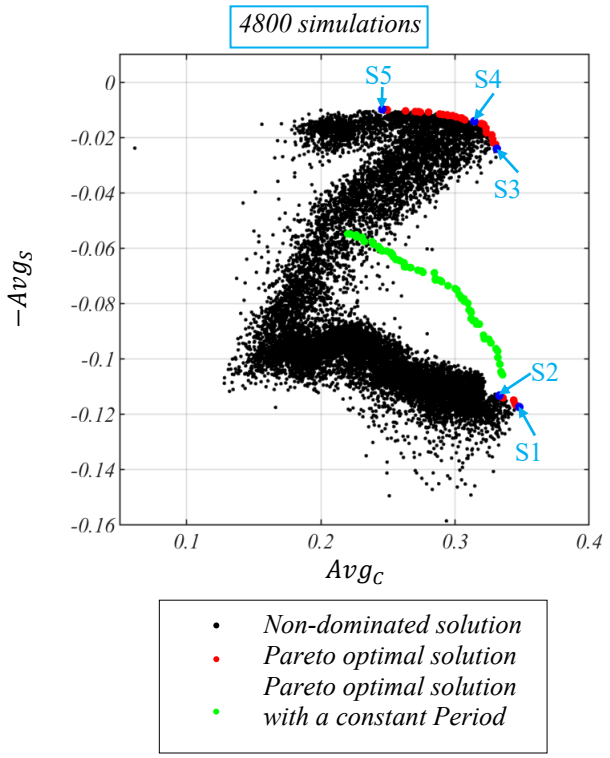

Figure 6-9 Search history of MOGWO after 4800 simulations (scenario 4: $\theta = \frac{\pi}{3}$).

Table 6-4 The characteristics of the highlighted PhC LED designs of Figure 6-9 (scenario 4).

Label	D	W_0	W_1	W_2	W_3	W_4	W_5	$Period$	Avg_C	$-Avg_S$
S1	278	775	238	388	548	558	422	817	0.348	-0.118
S2	268	790	234	391	539	583	389	806	0.333	-0.113
S3	462	27	46	59	134	112	71	167	0.331	-0.024
S4	354	50	41	68	104	107	73	153	0.314	-0.014
S5	346	70	42	69	84	71	81	133	0.246	-0.01

Unit of width$_x$ (Wx), depth (D), and *Period* are nanometers.

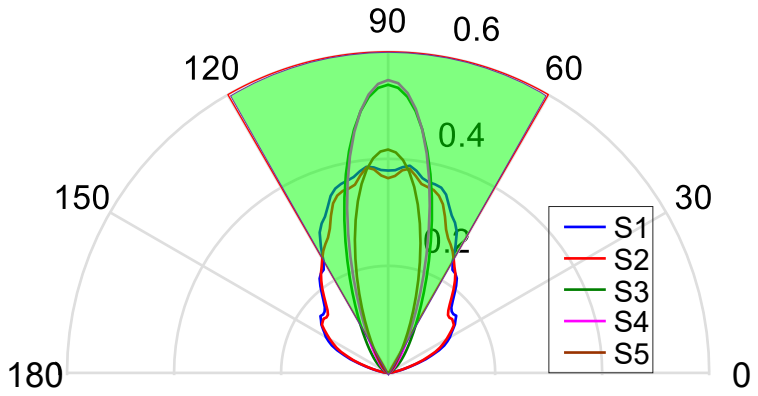

Figure 6-10 Radiation pattern of the highlighted PhC LED designs of Figure *6-9* (scenario 4).

Scenario 5:

In this scenario, the θ is decreased to $\theta = \frac{\pi}{6}$. After 4800 simulations, MOGWO found 100 optimal designs. The search history of this scenario is shown in Figure 6-11. Also, the Pareto optimal solutions of the previous optimization (scenario 2) with a constant *Period*=0.6 μm are illustrated in this figure for comparison. A similar observation is made here: considering *Period* in the optimization process provides more flexible PhC LED structure. Therefore, by finding the proper values for the whole structural parameters, very high performance devices will be obtained. The properties and radiation patterns of some highlighted designs of this optimization are provided in Table 6-5 and Figure 6-12.

The search history of Figure 6-11 shows that *Period* is a significant parameter when we want to shape the radiation pattern. More interestingly, this parameter is important for focusing the light in a narrow-angle range.

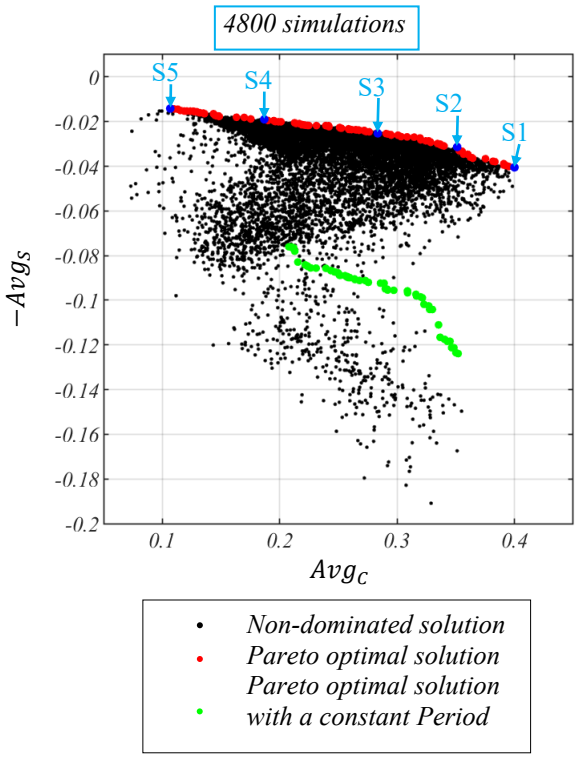

Figure 6-11 Search history of MOGWO after 4800 simulations (scenario 5: $\theta = \frac{\pi}{6}$).

Table 6-5 The characteristics of the highlighted PhC LED designs of Figure 6-11 (scenario 5).

Label	D	W_0	W_1	W_2	W_3	W_4	W_5	$Period$	Avg_C	$-Avg_S$
S1	268	105	54	123	144	94	60	170	0.4	-0.04
S2	234	101	42	80	116	60	39	140	0.351	-0.031
S3	209	110	25	60	110	43	16	126	0.284	-0.025
S4	212	107	49	38	73	16	2	112	0.187	-0.019
S5	195	100	56	22	56	4	0	100	0.107	-0.014

Unit of width$_x$ (Wx), depth (D), and $Period$ are nanometers.

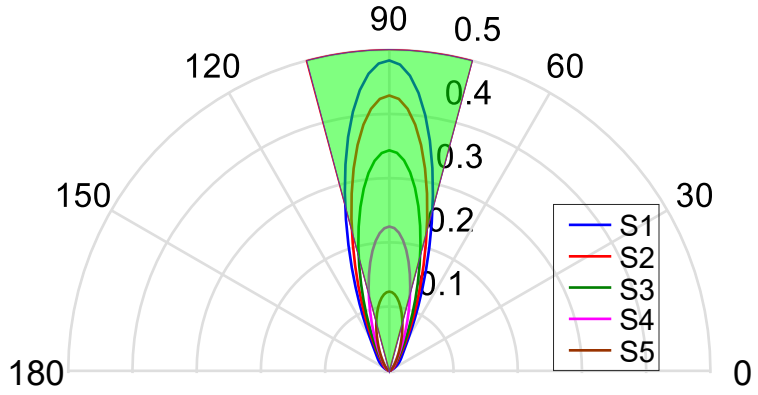

Figure 6-12 Radiation pattern of the highlighted PhC LED designs of Figure 6-11 (scenario 5).

Scenario 6:

As it was mentioned before, in addition to radiation pattern focusing, the uniformity of the

radiated light within the θ angle is also very important for some applications. Therefore, we consider Avg_c and *Deviation* as the merit factors of PhC LEDs. After employing MOGOW and 4800 simulations, 21 optimal designs were found. The search history of this scenario is shown in Figure 6-13. The Pareto optimal solutions of the previous optimization (scenario 3) with a constant *Period*=0.6 μm are also visualized in this figure. The comparative study shows that the results of having *Period* as independent structural parameters provide optimal designs with much higher performances. The characteristics and radiation patterns of some highlighted designs of Figure 6-13 are shown in Table 6-6 and Figure 6-14.

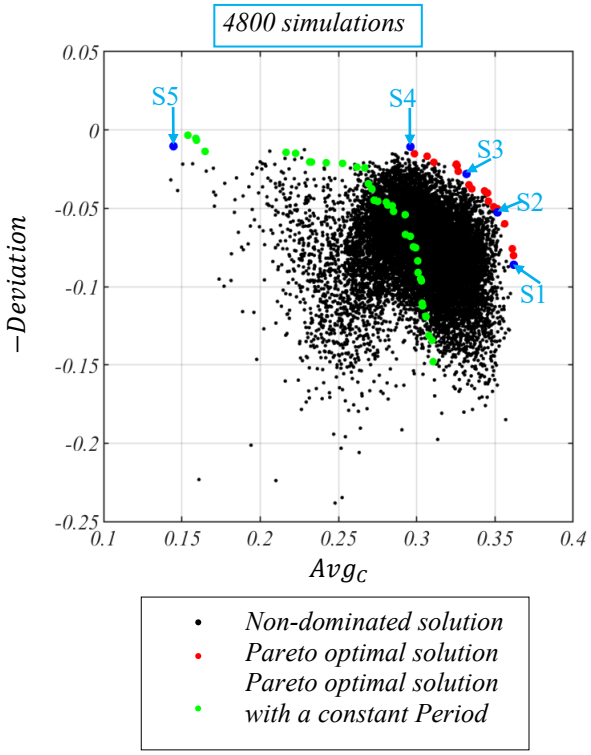

Figure 6-13 Search history of MOGWO after 4800 simulations for uniform radiation intensity in $\theta = \frac{\pi}{3}$ (scenario 6).

Table 6-6 The characteristics of the highlighted PhC LED designs of Figure 6-13 (scenario 6).

Label	D	W_0	W_1	W_2	W_3	W_4	W_5	*Period*	Avg_C	$-Deviation$
S1	522	57	701	33	600	172	693	1000	0.362	-0.086
S2	517	20	772	20	686	204	734	1000	0.352	-0.053
S3	550	55	739	114	634	253	615	997	0.332	-0.028
S4	549	341	381	161	353	181	502	781	0.296	-0.011
S5	518	192	42	96	53	82	183	233	0.145	-0.01

Unit of width$_x$ (Wx), depth (D), and *Period* are nanometers.

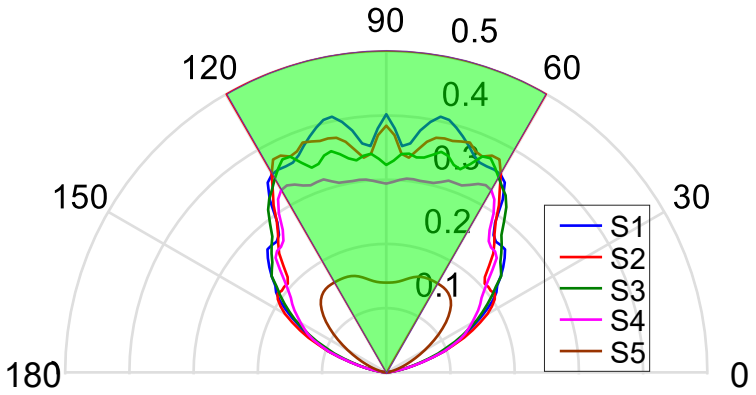

Figure 6-14 Radiation pattern of the highlighted PhC LED designs of Figure 6-13 (scenario 6).

The results in the six scenarios show the effectiveness of the proposed method to shape the radiation pattern of PhC LEDs. The behavior of the two objectives indicates that these objectives are in conflict. Increasing the one culminates in decreasing the other. As a result, solving the problem by considering two independent objectives is an effective way to find the designs in which a trade-off is being established between the objectives. Note that there is not a single solution for multi-objective problems. Alternatively, a set of optimum solutions is the answer to multi-objective problems. Moreover, these substantial achievements are obtained by just tuning the variables. The fabrication process is not changed, and additional PhC layers are not added to the structure.

In order to extend the proposed approach to two-dimensional PhC LEDs, the spherical coordinate system should be utilized instead of the polar coordinate system for radiation patterns. The average of radiation intensity will be calculated with respect to two angles (θ, φ). Although two-dimensional PhC LEDs are more common, the simulation time increases by 2–3 orders of magnitude in two-dimensional structures. Fortunately, current CPUs are powerful enough to perform such optimization.

6.5 Post processing on Pareto optimal designs:

After the optimization process in all scenarios, the final result is a set of optimal solutions called Pareto optimal solutions. We need to choose one of the optimal designs which establishes the best tradeoff between the output merit factors. If there are no criteria for the merit factors, we can use a combination of the merit factors (O) as a new merit factor ($O = \frac{Avg_C}{Avg_S}$ or $O = \frac{Avg_C}{Deviation}$). Therefore the best design in terms of O factore is a design which shows highest O factor.

In another case, there might be a set of criteria for one or both of the output merit factors. For example, considering $Avg_S < M$ where M is a constant value, we should remove the solutions in the Pareto optimal solution set that do not sasisfy this criterion. After that, we select a design that shows the highest Avg_C. For more details about decision makings techniques and practices, interested readers are referred to [6].

6.6 Conclusion

In summary, the results show that the proposed method could be utilized to shape the radiation pattern of any PhC LEDs for specific applications. The results are obtained by just employing MOGWO to tune the structural parameters. No extra complexity in terms of the fabrication process and the shape of the PhC layer is added to the PhC LEDs. It is worth mentioning that a

pre-defined PhC LED design is not required to embark on the optimization. We just defined the objectives corresponded to a specific application. Then, a multi-objective optimizer is employed to find a wide range of optimal designs providing many choices for LED designers to attain a well-matched design for the specific application.

Chapter 7: Conclusion and Future Works

7.1 Conclusion:

The case studies investigated in this thesis have shown that the AI optimizers are able to effectively optimize the design (involving physical structures and material compositions) of several different newly introduced optical devices. Therefore, this shows that a wide range of optical devices (useful for diverse applications) can be formulated and designed.

This approach for solving the problem of optical devices design does not require human involvement, neither to provide a starting initial design nor to guide the optimization process. Various single- and multi-objective algorithms can be easily utilized to implement the optimizer module in order to achieve a wide range of optimal designs. Finally, the proposed optimization frameworks for designing optical devices open up an effective way of developing a new generation of optical devices.

7.2 Research Contributions

7.2.1 Design optimization of orbital angular momentum fibers

Optical data communication based on the orbital angular momentum (OAM) of light is a recently proposed method to enhance the transmission capacity of optical fibers. This requires a new type of optical fibers, the main part of the optical communication system, to be designed. Typically, these fibers have a ring-shaped refractive index profile. We aim to find an optimized cross-section refractive index profile for an OAM fiber in which the number of supported OAM modes (channels), mode purity, and the effective refractive index separation of OAM modes to other fibers modes are maximized. However, the complexity of the relationship between structural parameters and optical transmission properties of these fibers has resulted in the lack of a comprehensive analytical method to design them. In this thesis, we have investigated the process of designing OAM fibers and proposed a framework to design such fibers by using artificial intelligence optimizers. It is worth mentioning here that this problem is intrinsically a multi-objective optimization problem and the actual solution for such problems is not unique and leads to a set of optimum solutions. Therefore, at the end of the optimization process, a wide range of optimal designs have been obtained in which a trade-off is established in each of the solutions. We solved this problem with the multi-objective Grey wolf optimizer (GWO) and compared the results with that of the single-objective GWO. The framework can easily find many optimal designs that support more than 20 OAM modes. The obtained results show that the proposed method is comprehensive and can optimize the structure of any OAM fibers. No human involvement, simplicity, and being straightforward are the main advantages of the proposed framework.

7.2.2 Optimization frameworks for designing photonic crystal filters

We have proposed a framework for multi-objective optimization of photonic crystal (PhC) filters. In this framework, the Multi-Objective Gray Wolf Optimizer has been utilized to automatically find the optimal designs. The proposed method is able to design any kind of PhC filter. As a case study, a new structure of super defect PhC filter for application in the wavelength division multiplexer (WDM) was designed using the framework. The results show that the proposed framework is comprehensive and able to find a significantly wide range of optimal designs for general and specific application such as WDM with respect to each defined WDM standard.

7.2.3 Radiation pattern design of photonic crystal LED

We have proposed an effective method for shaping the radiation pattern intensity of Photonic Crystal (PhC) Light-Emitting Diodes (LED). In this method, the process of shaping the radiation pattern intensity is first formulated as a multi-objective problem. The Multi-Objective Gray Wolf Optimizer (MOGWO), is then utilized to find a set of optimal designs. The proposed shaping method aims to focus the intensity of light in a narrow-angle range and provide uniform radiated light in this range. The proposed method is also described and applied to a case study. The results show that the method proposed is beneficial and could be utilized to design any kind of PhC LEDs. As the lack of analytical method prevents researchers form finding optimal designs, this method is a shortcut to systematically shape the radiated intensity of PhC LED light.

7.3 Future work

- Optical data communication based on the OAM of light provides high capacity data communication. This interesting research topic needs to be investigated in detail in order to reach a mature level of advancement to be applied in the practical systems. Generation, modulation, and transmission of OAM modes with minimal dispersion, as well as detection and demultiplexing of OAM mode, are topics in the field of optical MDM where a significant amount of work is being done, and where more exploration is required.
- Considering fabrication uncertainties during the optimization of optical devices, using the constraint module.
- Robust optimization can be very important in some complicated photonic structures like photonic crystal fibers, where small changes in the size of an element can lead to huge changes in the characteristics of the fiber. For such cases, applying robustness parameters to the objective list can significantly improve the convergence and reliability of the final designs.
- In this thesis, we have mainly focused on the steady-state operation of optical devices. Evaluating the dynamic response of active and passive optical components is extremely crucial for assessing device capabilities at high speeds.
- Fabrication of the optimized devices and experimental validations are two fundamental pillars for asserting the reliability of the optimization frameworks. Post-fabrication re-optimization will be required in cases where the expected results from the optimal design do not match well with experimental data.

Appendix A: Optimal Design of Large Mode Area Photonic Crystal Using The Multi objective Gray Wolf Optimizer

A.1 Introduction

This appendix is based on the paper published in the Journal of Journal of Lightwave Technology [4]. High power fiber lasers and amplifiers have been the subject of enormous researches during the last decades. Nowadays, industrial fiber lasers with the output power up to 100 kW are available [128]. However, the maximum achievable power is limited by the nonlinearity and optical damages arisen from high power density. By increasing the mode area in such fibers, the power density decreases and consequently the onset of the nonlinear effects increases significantly [129]–[131]. On the other hand, in order to obtain a high beam quality and power stability, the single-mode operation of the large mode area (LMA) fiber should be guaranteed [132]–[134].

In order to increase the mode area of conventional LMA optical fibers, it is required to increase the core radius of the fiber. Enhancing the mode area with the increase of core size results in the appearance of higher-order modes (HOMs) and subsequently the multimode operation of LMA fiber [135], [136]. Having a low contrast between the core and cladding indices is necessary for single-mode operation. However, fabrication of conventional LMA fibers with a very low numerical aperture (NA) is a challenging process. Moreover, LMA fibers are often coiled to fabricate smaller devices. Conventional LMA optical fibers with low NA are very sensitive to bending and it is difficult to achieve low bending loss and LMA simultaneously [131], [137], [138].

It is possible to have a good compromise between the large mode field area and the single-mode operation using photonic crystal fibers (PCFs). The effective refractive index of the cladding region and the NA of the PCFs are tailored by varying the diameter of the air-holes and the hole-pitch (the center-to-center spacing between two adjacent air-holes). These variations can lead to an increase in the size of the core region, enhancement of the loss of the higher-order modes, and the decrease of the fundamental mode loss. Therefore, the single-mode operation of LMA-PCFs can be achieved [139]–[142]. However, in PCFs with symmetric structures the bending loss is significant and the mode area experiences a large reduction in the bent state. It has been proven that non-symmetric designs shows superior performance on HOM suppression, potentially enabling to increase the threshold for appearance of mode instabilities [143]. It is worth noting that although all-solid LMA leakage channel fibers (LCFs) have a high mode area and a simpler fabrication process, their FM loss is higher than air-hole PCFs [144].

M. Napierała et al. reported an asymmetric LMA-PCF structure with single-mode operation based on removing two additional air-holes in the cladding region, where the structure was optimized with a few degrees of freedom [145]. In order to obtain the best possible design of an LMA-PCF, all degrees of freedom could be taken into account, i.e. the diameters of all air-holes as well as the structure pitch. However, finding a relation between the structural parameters of the LMA-PCFs and the output performance is difficult and needs much skills and efforts. Moreover, due to a large number of input parameters, it is impossible to achieve an optimal structure using trial and error methods. Therefore, employing systematic approaches such as optimization techniques and artificial intelligence would be required to find the optimum structures.

In this chapter, we utilize the Multi-Objective Gray Wolf Optimizer (MOGWO) to maximize the effective mode area (EMA) and the bending loss of HOMs, while minimizing the

fundamental mode (FM) loss to maintain the single mode operation in the bent state. The chapter is organized as follows. In Section A.2, the PCF structure is introduced and the method of analysis is explained in details. The multi-objective optimization framework for designing the LMA-PCF is described in Section A.3. In Section A.4, the optimal results are reported and discussed. Finally, the chapter is concluded and summarized in Section A.5.

A.2 Theoretical Background

The three-dimensional schematic of the investigated LMA-PCF is shown in Figure A-1. As seen from the figure, the fiber is in a circular bent state with a bending radius of R, where the wave propagates in the φ direction. The eigenvalue equation for the electric field is obtained from the vector Helmholtz equation [17]

$$\nabla \times (\nabla \times E) - {k_0}^2 n^2 E = 0 \tag{A-1}$$

where E is the electric field vector, k_0 is the wavenumber in the free space, and n is the refractive index.

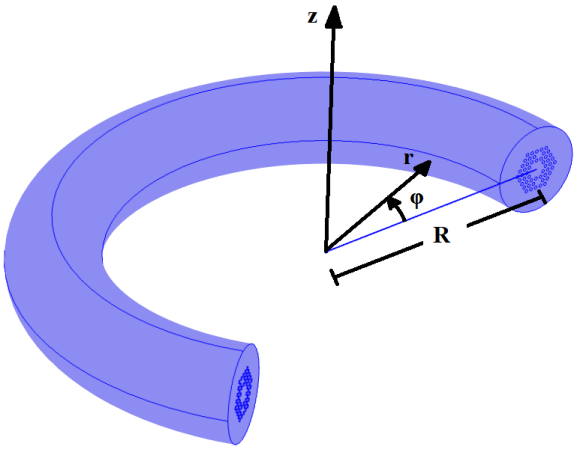

Figure A-1 Three-dimensional schematic of the bent LMA-PCF.

The cross-section of the proposed LMA-PCF structure is shown in Figure A-2. The air-holes are arranged in a hexagonal lattice with seven missing air-holes in the core region. Furthermore, two air-holes have been removed from the cladding region to improve the index-matched coupling between the core and cladding modes and consequently increasing the loss of HOMs [145]. The core is surrounded by three rings of air-holes to ensure good confinement of the light in the core. As seen in Figure A-2, the parameters r_1 to r_{29} represent the radii of air-holes and Λ denotes the air-hole pitch. It should be noted that the structure is symmetric along the z-direction. The background material is silica with the refractive index of 1.45 at λ=1.064 μm wavelength [146]. It is assumed that besides ytterbium doping, the core is co-doped with other rare earth elements and the refractive index is preserved to the level of undoped silica [145]. We have used the finite element method (FEM) combined with the perfectly matched layer (PML) boundary condition to calculate the eigenvalues and the mode profiles. The EMA of the FM, the bending loss of the HOMs, and the FM loss are considered as the optimization objectives.

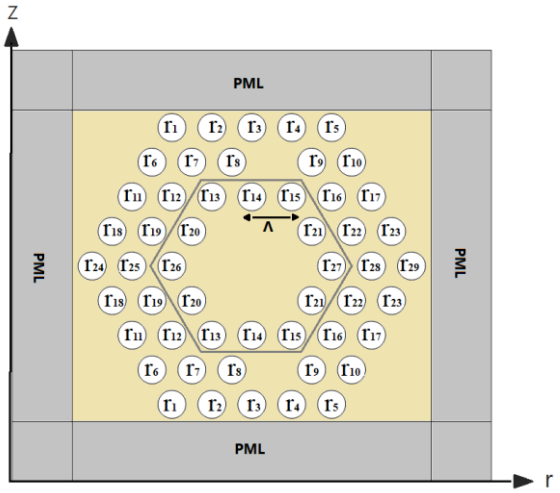

Figure A-2 Two-dimensional model of the bent LMA-PCF. The hexagonal shape with a side length of 2.5 Λ is the boundary between the doped and undoped regions.

Bending loss

The bending loss of modes (dB/m) can be calculated using the imaginary part of the propagation constant as [147]

$$L = 8.686 k_0 \, Im(n_{\text{eff}}) \tag{A-2}$$

where Im(β)Im(neff)Im(n_{eff}) is the imaginary part of the effective refractive index of the propagating mode, and k_0 is the free space wavenumber in 1/m.

Effective mode area (EMA)

The EMA of the propagating mode in the PCF structure can be calculated using [21]

$$A_{\text{eff}} = \frac{(\iint |E|^2 dzdr)^2}{\iint |E|^4 dzdr} \tag{A-3}$$

One of the major challenges in the optimization of the LMA-PCF structure is to recognize the order of the modes. One solution would be the use of effective index which is not very useful for the bent fiber which contains both cladding and core modes [148]. In this work, an image processing technique has been employed to recognize the mode order based on the electric field distribution of the propagating modes [149].

A.3 Multi-objective Optimization Framework

In order to optimize the LMA-PCF structure, the MOGWO is utilized for maximizing the EMA and the bending loss of the HOMs (L_H) while minimizing the FM loss (L_F), where L_H is the lowest bending loss among all HOMs. In this optimization problem, there are three conflicting objectives to be optimized and the constraints to be fulfilled. Such a multi-objective problem does not have a single optimal solution. Instead, a set of optimum solutions known as the Pareto-optimal set is the answer to such problems. The multi-objective optimization algorithm considers multiple merit factors and finds a wide range of optimal designs. It is worth mentioning here that combining merit factors in order to solve the problem using the single-objective optimization approach causes finding only one member of the Pareto-optimal set [6]. Therefore, the multi-

objective optimization is the best way to solve this problem. The main parts of this framework are shown in Figure A-3. As seen in this figure, the framework is composed of three major components including the parameter module (PM), the constraint module (CM), and the optimizer module (OM). First, the structural parameters and limitations are defined in the PM and CM and are then fed into the OM. Finally, the OM moves towards the optimal solutions based on the MOGWO algorithm.

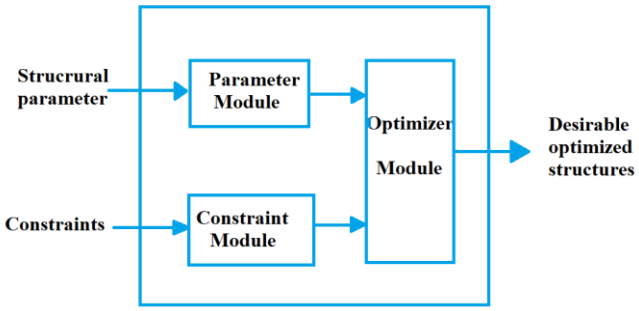

Figure A-3 The proposed multi-objective framework for designing the LMA-PCF.

Parameter Module (PM)

The PM defines and selects the structural parameters. The diameters of the air-holes and the hole-pitch are the structural parameters. Due to the symmetry of the structure along the z-axis, there are 29 air-holes with independent diameters defined as the input parameters. By including the hole-pitch, there would be 30 input parameters in the PM, as follows

$$PM = \left[\frac{r_1}{\Lambda}, \frac{r_2}{\Lambda}, \ldots, \frac{r_{28}}{\Lambda}, \frac{r_{29}}{\Lambda}, \Lambda\right] \tag{A-4}$$

Constraint Module (CM)

This module contains the range of structural parameters and other device limitations during the optimization process. Therefore, there are two groups of constraints. The first group is the range of parameters (CM_1) which expresses the manufacturing and bending limitations. In this regard, we assume that the radii of all air-holes are limited to the range of 0.1Λ -0.4Λ. Exceeding beyond the upper limit may lead to an overlap between adjacent air-holes while decreasing beyond the lower limit is hard to achieve. The second group of the constraints expresses the limitations on the outputs CM_2, CM_3, and CM_4. The optimal structures are assumed to have EMA> 600 μm^2, L_H > 8 dB/m, and L_F <0.02 dB/m.

$$\begin{aligned}
&CM = [CM_1, CM_2, CM_3, CM_4],\\
&CM_1: 0.1 < \frac{r_1}{\Lambda}, \frac{r_2}{\Lambda}, \ldots, \frac{r_{28}}{\Lambda}, \frac{r_{29}}{\Lambda} < 0.4,\\
&16(\mu m) < \Lambda < 19(\mu m)\\
&CM_2: L_F < 0.02\left(\frac{dB}{m}\right),\\
&CM_3: L_H > 8\left(\frac{dB}{m}\right)\\
&CM_4: EMA > 600(\mu m^2)
\end{aligned} \tag{A-5}$$

These constraints are chosen based on the original structure which was reported in [145], which

guarantees that all of the members of the Pareto front show better performance compared to the previous work.

Optimizer Module (OM)

In this module, the optimizer and the optimization objectives are defined. To implement the optimizer, a wide range of multi-objective optimizers can be employed [22], [89], [90]. We choose MOGWO which mimics the leadership and hunting behavior of grey wolves in nature [21], [24]. Because of having a large number of structural parameters, the search space is huge and has many local optimums. The MOGWO has the mechanism to avoid trapping in the local optimums.

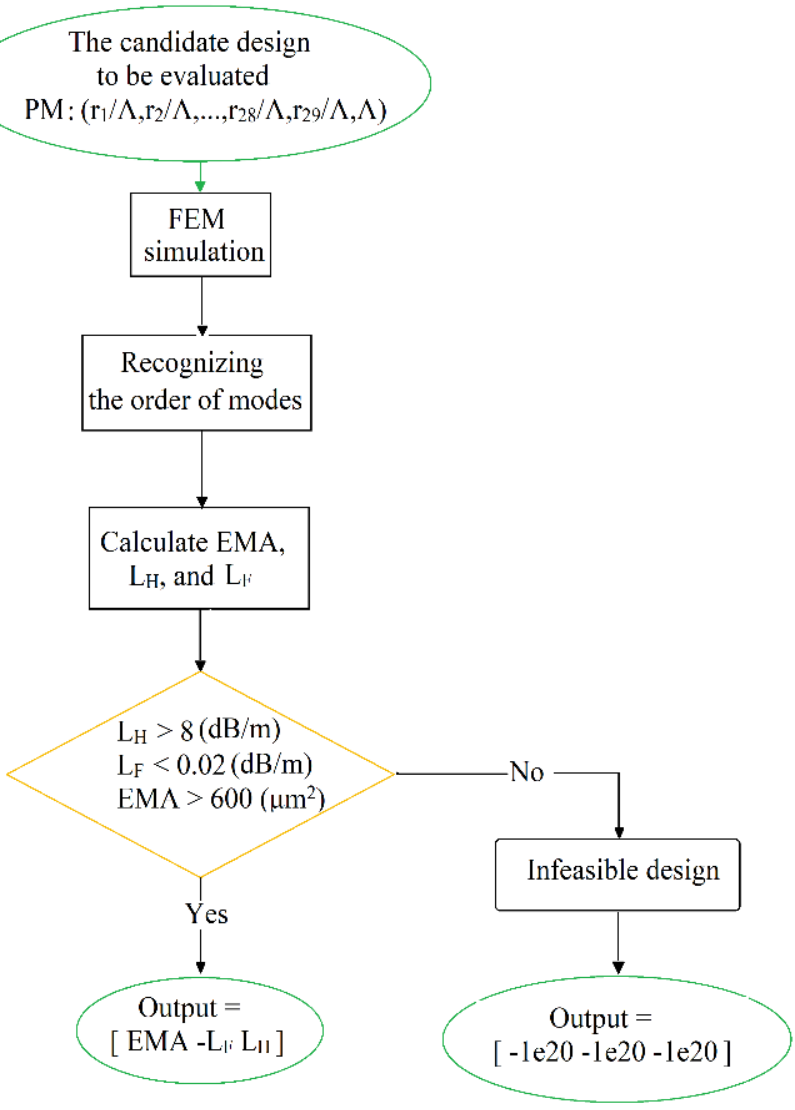

Figure A-4 Flowchart for the calculation of LMA-PCF merit factors.

The flowchart of calculating the merit factors is shown in Figure A-4. The FEM simulation is performed for the defined structure. Then the order of modes is recognized using image processing techniques. After that, the EMA and the LF are calculated for the fundamental mode and the LH is evaluated for the HOM with the lowest loss. Therefore, the optimizer considers the

problem as a black box, in which the input is composed of the structural parameters and the output is a collection of the merit factors. For the candidate designs in which the constraints do not satisfy, a low negative value of -1e20 will be assigned to the objectives. By doing so, the optimizer can understand that such candidate designs are not feasible and consequently neglect them during the optimization process.

Table A-1 Properties of optimum structures designed by MOGWO which are marked in Figure A-4

	1	2	3	4	5	6	7	8	9	10	11	12	13	14	15	16
r_1/Λ	0.27	0.26	0.22	0.22	0.27	0.25	0.26	0.25	0.25	0.25	0.24	0.21	0.23	0.25	0.19	0.24
r_2/Λ	0.20	0.18	0.18	0.16	0.18	0.16	0.16	0.16	0.18	0.18	0.15	0.13	0.18	0.18	0.11	0.16
r_3/Λ	0.37	0.35	0.37	0.33	0.33	0.37	0.36	0.36	0.36	0.34	0.36	0.31	0.37	0.34	0.31	0.34
r_4/Λ	0.38	0.38	0.34	0.36	0.34	0.31	0.36	0.35	0.37	0.34	0.33	0.33	0.33	0.34	0.29	0.35
r_5/Λ	0.22	0.21	0.19	0.22	0.22	0.19	0.19	0.21	0.21	0.22	0.21	0.18	0.19	0.20	0.18	0.20
r_6/Λ	0.16	0.18	0.15	0.19	0.16	0.18	0.14	0.19	0.16	0.17	0.18	0.17	0.15	0.16	0.22	0.16
r_7/Λ	0.23	0.23	0.25	0.21	0.21	0.23	0.24	0.23	0.26	0.21	0.23	0.24	0.26	0.23	0.25	0.23
r_8/Λ	0.35	0.35	0.37	0.35	0.37	0.36	0.40	0.37	0.36	0.37	0.39	0.37	0.36	0.37	0.40	0.36
r_9/Λ	0.13	0.14	0.13	0.13	0.14	0.13	0.10	0.12	0.12	0.14	0.11	0.12	0.12	0.12	0.11	0.11
r_{10}/Λ	0.21	0.24	0.25	0.25	0.24	0.26	0.27	0.25	0.23	0.23	0.25	0.23	0.25	0.25	0.25	0.25
r_{11}/Λ	0.29	0.28	0.25	0.29	0.29	0.30	0.31	0.32	0.29	0.29	0.31	0.33	0.26	0.28	0.32	0.28
r_{12}/Λ	0.29	0.24	0.24	0.22	0.23	0.26	0.25	0.26	0.25	0.23	0.27	0.29	0.23	0.24	0.31	0.25
r_{13}/Λ	0.19	0.17	0.16	0.17	0.17	0.17	0.13	0.14	0.16	0.17	0.13	0.12	0.17	0.16	0.14	0.16
r_{14}/Λ	0.25	0.26	0.26	0.25	0.25	0.24	0.26	0.25	0.26	0.25	0.23	0.23	0.25	0.25	0.20	0.24
r_{15}/Λ	0.17	0.19	0.19	0.20	0.20	0.18	0.20	0.19	0.19	0.20	0.17	0.14	0.20	0.19	0.12	0.18
r_{16}/Λ	0.26	0.27	0.29	0.24	0.26	0.29	0.29	0.28	0.28	0.26	0.29	0.32	0.29	0.27	0.30	0.27
r_{17}/Λ	0.30	0.31	0.28	0.34	0.31	0.31	0.28	0.32	0.29	0.31	0.28	0.30	0.27	0.27	0.31	0.28
r_{18}/Λ	0.30	0.30	0.35	0.35	0.32	0.34	0.34	0.35	0.31	0.32	0.34	0.30	0.35	0.34	0.29	0.35
r_{19}/Λ	0.26	0.27	0.26	0.28	0.27	0.26	0.23	0.25	0.30	0.27	0.25	0.23	0.25	0.25	0.26	0.24
r_{20}/Λ	0.22	0.20	0.21	0.22	0.19	0.21	0.18	0.19	0.23	0.20	0.22	0.22	0.22	0.22	0.24	0.22
r_{21}/Λ	0.17	0.18	0.20	0.18	0.19	0.16	0.16	0.15	0.16	0.19	0.14	0.10	0.18	0.17	0.10	0.17
r_{22}/Λ	0.24	0.27	0.24	0.28	0.24	0.25	0.25	0.24	0.23	0.24	0.25	0.21	0.24	0.26	0.20	0.25
r_{23}/Λ	0.29	0.31	0.34	0.33	0.33	0.30	0.33	0.32	0.30	0.33	0.32	0.35	0.34	0.32	0.32	0.32
r_{24}/Λ	0.21	0.21	0.21	0.23	0.21	0.22	0.22	0.22	0.21	0.20	0.24	0.24	0.21	0.20	0.21	0.20
r_{25}/Λ	0.18	0.20	0.15	0.19	0.20	0.20	0.18	0.20	0.20	0.20	0.18	0.19	0.15	0.18	0.17	0.18
r_{26}/Λ	0.24	0.22	0.23	0.25	0.22	0.22	0.23	0.21	0.23	0.22	0.22	0.26	0.23	0.21	0.28	0.22
r_{27}/Λ	0.28	0.29	0.31	0.31	0.29	0.31	0.31	0.32	0.30	0.29	0.31	0.31	0.31	0.29	0.32	0.29
r_{28}/Λ	0.28	0.28	0.27	0.30	0.29	0.29	0.25	0.29	0.28	0.29	0.28	0.28	0.26	0.27	0.31	0.26
r_{29}/Λ	0.26	0.27	0.24	0.26	0.28	0.27	0.27	0.28	0.26	0.28	0.27	0.28	0.24	0.26	0.28	0.27
$\Lambda(\mu m)$	18.1	18.5	18.1	18.4	18.4	18.5	18.5	18.5	18.4	18.4	18.6	18.6	18	18.3	18.4	18.2
$EMA\ (\mu m^2)$	679	678	669	680	667	703	702	706	694	666	728	803	673	680	**828**	688
$L_F\ (10^{-4}$ $dB/m)$	44.7	10.0	6.01	6.86	7.16	11.1	15.3	10.9	45.3	7.60	26.3	52.0	**5.84**	17.6	112	24.6
$L_H\ (dB/m)$	**98.5**	23.7	18.5	20	27.4	14.4	42.3	10.7	81.1	29.5	31.9	8.85	11.1	65.7	9.33	62.2

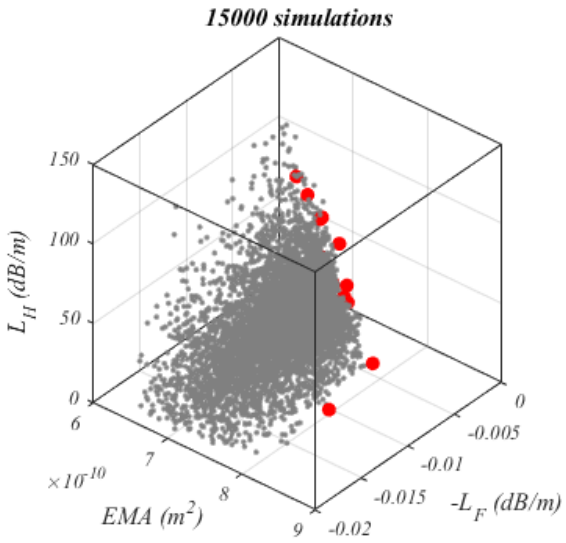

Figure A-5 Search history of the multi-objective optimization.

A.4 Results and Discussion

As mentioned before, the conflicting nature of merit factors has made the problem multi-objective. Therefore, the optimizer selects the optimum designs among different possible structures. We employ the MOGWO with 60 artificial grey wolves and maximum of 250 iterations. A complete simulation run took approximately four weeks on a server with 40 cores and 256 GB of RAM. The optimization search history is shown in Figure A-5, where 16 selected optimal designs are marked with red filled circles. The optimization method has found 16 optimal designs, which their properties and their output characteristics are depicted in Table A-1. The best structures are bolded in terms of the EMA, the L_H, and the L_F. These structures are the optimal designs that have well confinement of FM, improved EMA and very lossy HOMs. The EMA for this bending radius is acceptable and can be improved by a factor of 1.26 compared to the design reported in [145]. Furthermore, the bending loss of the HOMs (the FM) can be increased (decreased) by a factor of 7 (17). In order to calculate the L_H, the cladding modes with no electric field inside the core region are neglected and only those that have an electric field component in the core region are taken into account. According to the market demand, all of these optimal designs are desirable and no one is better than the others. The column #1 in Table A-1 shows the values of the structural parameters for the optimal design with the highest HOM loss. However, the FM loss of this structure is among the highest losses and also the EMA is not as high as many other optimal designs. Column #13 in Table A-1 illustrates the values of structural parameters for the optimal design with the lowest FM loss. For this case, the EMA of the fiber is one of the lowest among all structures, which implies that the optical mode is confined inside the core region and the scattering loss due to the propagation inside the cladding region is minimal. In other words, there is a trade-off between the EMA and the FM loss. As shown in column #15 of Table A-1, this structure has the highest EMA and FM loss among all optimal structures. The large FM loss is a result of spreading the FM over an area larger than the core region, which has led to a decrease in the FM confinement and an increase in the scattering loss.

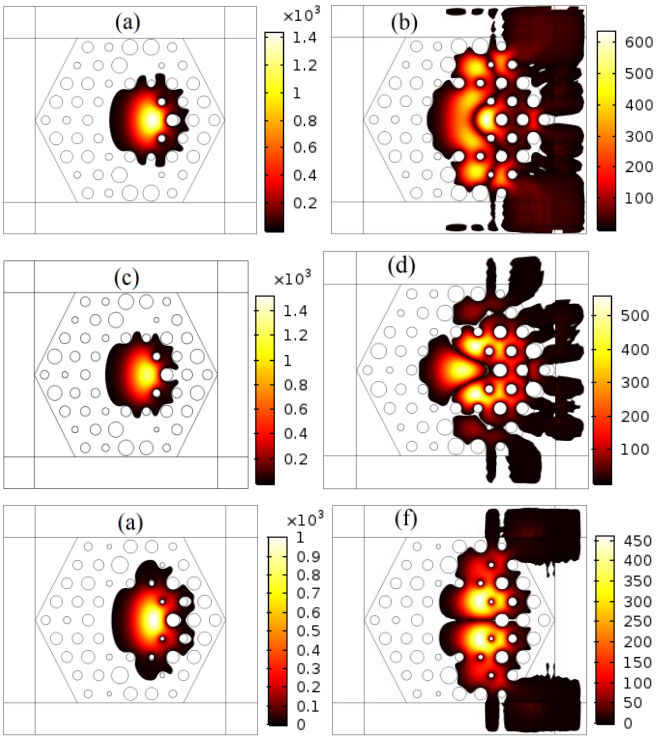

Figure A-6 Field distribution for the (a) FM of design #1 (b) HOM of design #1 (c) FM of design #13 (d) HOM of design #13 (e) FM of design #15 (f) HOM of design #15. All simulations are performed for λ=1.064 μm.

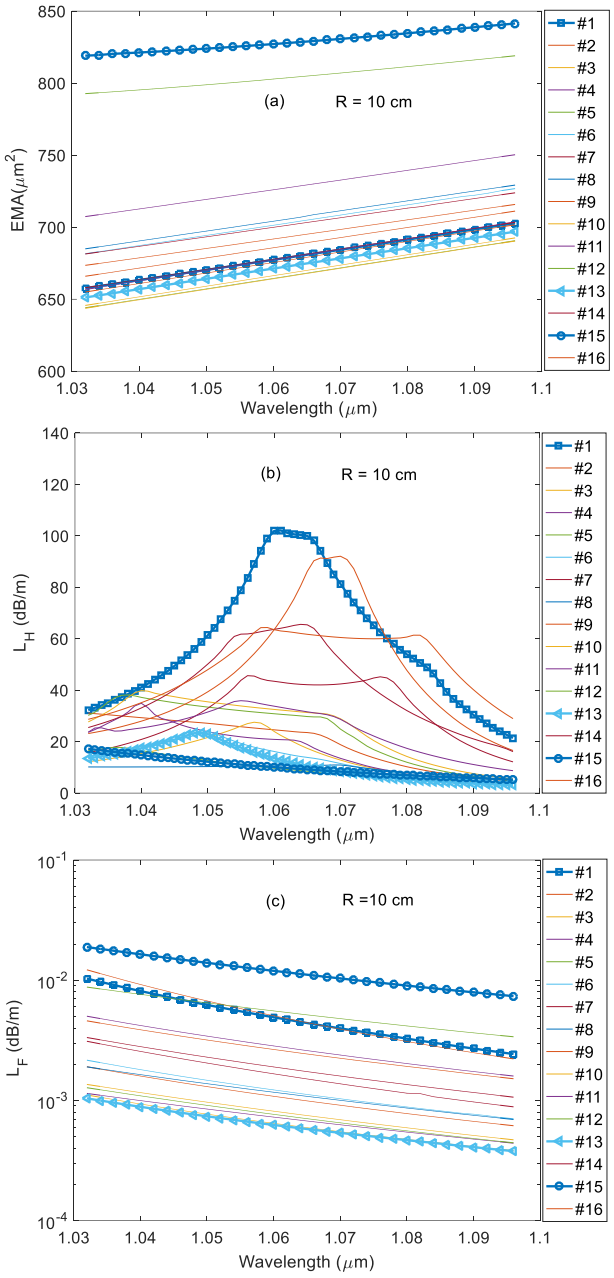

Figure A-7 Wavelength dependence of the (a) effective mode area, (b) higher order mode loss, and (c) fundamental mode loss.

Figure A-6 illustrates the mode profile of the FM and the lowest-loss HOM in three LMA-PCF structures, i.e. #1, #13, and #15. In these profiles, the mode amplitudes are truncated at -40 dB relative to its maximum value. A comparison between Figure A-6(a), (c), and (e) reveals that the structure #15 (which has the highest EMA) has the lowest maximum electric field strength inside the core region and the highest leakage into the cladding region. Therefore, the FM loss for this structure is higher than that in other two structures. Furthermore, as can be seen in Figure A-6(b), 6(d), and 6(f), because of efficient leakage of the HOM profiles into the cladding region, the structure #1 has the highest HOM loss compared to all other optimal structures. The wavelength dependence of the L_F, the L_H and the EMA are illustrated in Figure A-7. As seen in Figure

A-7(a), the EMA increases with increasing the wavelength. This behavior is a result of decreased in-plane wavenumber at higher wavelengths. Figure A-7(b) shows that almost in all optimal designs the maximum values of the L_H occur around the design wavelength of 1.064 μm. One can see that the structure #1 which has the maximum L_H among all the optimal designs, shows the highest sensitivity to the wavelength. On the other hand, as seen in Figure A-7(c), the L_F decreases with increasing the wavelength in the bent state. This behavior is a result of better confinement of the FM at larger wavelengths. A comparison between the FM profiles shown in Figure A-8(a), (c), and (e) reveals that, as the wavelength of the input light increases the mode profile tends to move towards the center of the fiber core. Consequently, the bending loss decreases as a result of decreasing the scattering loss at larger wavelengths. As can be seen in Figure A-8(b), (d), and (f), the HOMs with the lowest losses are associated with the second order modes. However, while the lowest HOM loss at the wavelength of 1.032 μm is associated to the $LP_{11\text{-odd}}$ mode, the HOM with the lowest loss at the wavelengths of 1.064 μm and 2.5 μm correspond to the $LP_{11\text{-even}}$ mode. A comparison between the FM loss at the bent and straight states is demonstrated in Figure A-9. As seen in this figure, in contrary to the bent state, for the straight fiber the FM loss increases at larger wavelengths. This behavior is a result of the penetration of the mode profile into the cladding region rather than moving towards the core fiber. This result is in agreement with the results reported in [150].

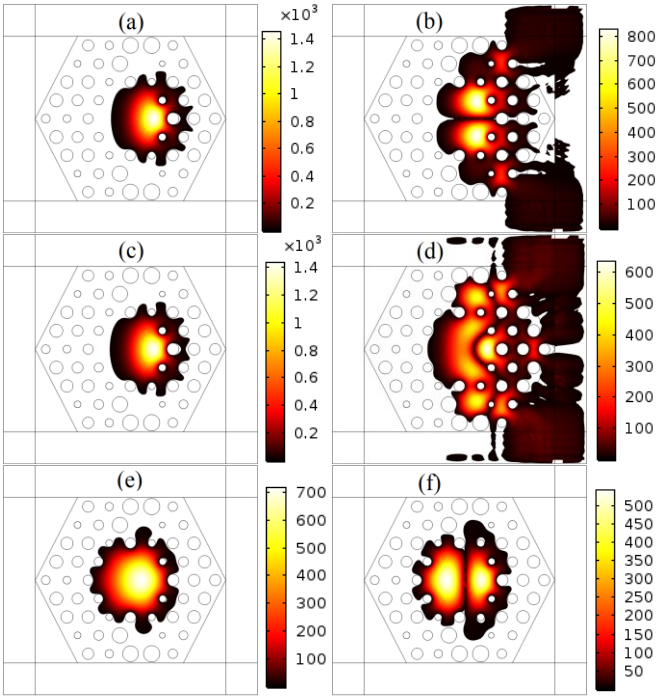

Figure A-8 Field distribution in design #1 for the (a) FM at λ=1.032 μm (b) HOM at λ=1.032 μm (c) FM at λ=1.064 μm (d) HOM at λ=1.064 μm (e) FM at λ=2.5 μm (f) HOM at λ=2.5 μm.

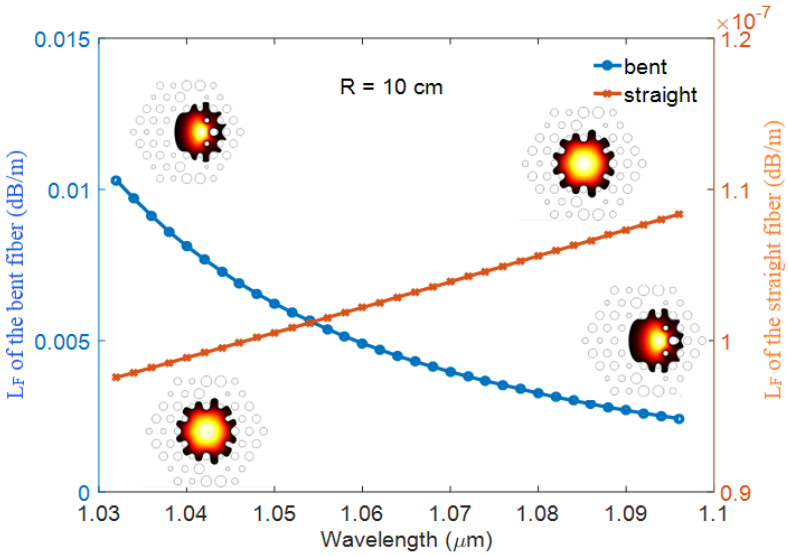

Figure A-9 The wavelength dependence of the FM loss for the optimal design #1 at the bent and straight states.

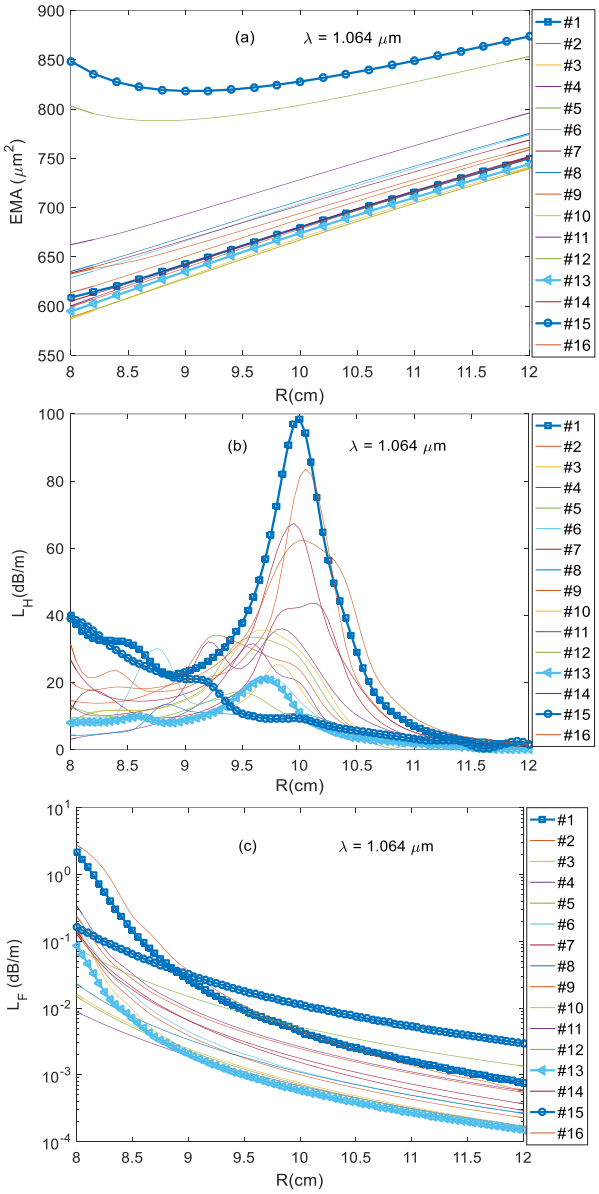

Figure A-10 The dependence of the (a) effective mode area, (b) higher order mode loss, and (c) fundamental mode loss on the bending radius.

Variations of the bending loss and the EMA versus the bending radius are illustrated in Figure A-10. As stated before, all structures that were optimized in this chapter were designed for the bending radius of 10 cm and are not necessarily optimal for other radii. As seen in Figure A-10(a), although the EMA enhances with increasing the radius for almost all optimal structures, in two cases namely structures #12 and #15, the EMA increases as the bending radius decreases below 9 cm. In these two structures, the FM field is drawn to the cladding region with decreasing the bending radius. Furthermore, Figure A-10(b) illustrates that the L_F decreases with increasing the bending radius. This result is in complete agreement with the simulation results reported in [18]. The dependence of the L_H on the bending radius is shown in Figure A-10(c). This figure reveals that the L_H is very sensitive to the bending radius. We can see that the L_H in almost all optimal structures has been maximized at the bending radius of 10 cm. On the other hand, the L_H in the optimal structure #1 is very sensitive to the bending radius. Meanwhile, a few designs like

the structure #15 have a low sensitivity to the bending radius. Consequently, based on the desired application, the optimal design could be selected among structures with the lowest sensitivity. It is worth mentioning that it is possible to prepare complex preform designs using laser drilling technology combined with the three-dimensional printing of doped fused silica glass [151], [152]. However, the characteristics of the optimized PCFs may undergo changes due to statistical structural fabrication-induced imperfections. The effects of the fluctuations in the size of the air-holes can be taken into account using a statistical analysis [153]. It should be noted that the refractive index of the silica changes due to the stress-optical effect (photo-elasticity) caused by the local strain in the bent PCF. Accordingly, the effect of the photo-elastic phenomena can be modeled by an effective bending radius varying between 1.28 R to 1.40 R [154], [155]. This means that the optimal performance of the PCF designed for the bending radius of 10 cm, will be achieved in the range of 7.1 to 7.8 cm.

A.5 Conclusion

In summary, a multi-objective optimization framework was proposed for designing single-mode LMA-PCFs. For this purpose, the MOGWO was utilized to maximize the EMA and the bending loss of HOMs while minimizing the FM loss. The simulation results demonstrated that the proposed multi-objective framework can effectively design and optimize the structure of LMA-PCFs. Sixteen optimal structures were designed that can be selected based on the desired applications. No initial design was required to start the optimization process. Furthermore, manufacturing limitations were included in the constraints module (CM). This framework enabled us to improve the EMA by a factor of 1.26 compared to the non-optimal design. Moreover, the bending loss of the HOMs (the FM) was increased (decreased) by a factor of 7 (17). The proposed framework is a general method for the design and optimization of optical fibers and can optimize any kind of PCFs for any type of application.

Appendix B: Design Optimization of a Waveguide-Based LP_{01} to LP_{0m} Mode Converter

B.1 Introduction

This appendix is based on the paper published in the Journal of Electronics Letters [5]. Space division multiplexing (SDM) has been proposed to overcome the capacity limitations of optical networks based on standard single mode fiber (SMF). It uses the orthogonal guided optical modes of few mode fibers to carry different optical signals, i.e., one mode corresponding to one optical channel. The high order of these modes is usually obtained from converting the fundamental mode [156].

Mode conversion can be achieved either using free-space or waveguide-based optics. Free-space mode conversion is based on matching the spatial profile from an input mode to an output mode using a phase mask or spatial light modulator such as liquid crystal on silicon (LCOS) [157]. This type of conversion includes phase plates, beam splitters, mirrors, and lenses. Therefore, it results in bulky structures with high insertion losses. Free-space based mode converters could be deployed in almost any wavelength window since they are wavelength insensitive.

Mode converter structures based on fibers or waveguides could be realized through a variety of techniques, such as grating, coupling, tapers, lanterns, photonic crystal fibers, etc.[157]–[161]. These converters are obtained by matching the propagation constant from the input mode to the (desired) output mode by altering the physical characteristics of the fiber or the waveguide such as its cross-section area or its refractive index.

In [162], a mode converter was proposed to convert LP_{01} to LP_{11} based on long-period fiber grating (LPFG). The converter was designed for the C-band and an insertion loss of 1.5 *dB* and an extinction ratio of 22 *dB* at 1550 *nm* are achieved. However, the converter can operate in a narrow bandwidth of 13 *nm* centered at 1551 *nm*. The work in [163] presented an LP_{01} to LP_{02} mode converter based on multimode interference (MMI) in a fiber and it was realized by interconnecting a single mode fiber (SMF) with a few-mode fiber (FMF) using a multimode fiber (MMF). The extinction ratio and loss of the mode converter are 55 *dB* and 1.8 *dB* respectively at 1550 *nm*.

Directional couplers can also be used to convert and multiplex different spatial modes [164]. Furthermore, couplers can be cascaded to convert and multiplex more modes such as the one illustrated in [165] for converting and multiplexing LP_{01}, LP_{11}, LP_{21} and LP_{02} with low insertion loss. Couplers can also be designed using Silica-based planar lightwave circuits (PLC) [161], [166]. Conversion using couplers is achieved through matching the effective index of one mode in one waveguide to the other mode in the other waveguide. Y-junctions and optical lanterns are other fiber structures to realize mode converters [166].

Structures based on waveguides for mode converters and multiplexers result in high mode conversion efficiency [167] and they are compact in footprint. However, they are in general wavelength dependent.

A mode converter based on a waveguide can be optimized by optimizing some of the structural parameters, and high mode conversion efficiency (i.e. low insertion loss) and high extinction ratio (i.e. high mode purity) are achieved. Another issue that should not be ignored is the feasibility of the device to be fabricated. There is a set of fabrication rules that should be

considered during the design/optimization process [168]. The more structural parameters are included, the more difficult the design/optimization process is, and also a larger degree of freedom can be achieved in design. Other researchers in this field, usually try to manipulate the structural parameters by some try and error simulations to find out the relations between the structural parameters and the device output merit factors [169]. Therefore, the process and human involvement are tedious, and also the final design will mostly be far from the optimal structure.

In this chapter, firstly, we propose a waveguide-based mode converter using two-stage taper structure that converts the fundamental LP_{01} mode to LP_{0m} (m=2, 3, …, 7) mode. Secondly, to solve the problem of finding the optimal design, we shall utilize an artificial intelligence optimizer called Grey Wolf Optimizer (GWO) to find the optimal structural parameters (physical dimensions) [21].

B.2 Mode Converter Structure and Related Definitions:

The proposed mode converter structure is based on the circular waveguide and is shown in Figure B-1. It consists of two-stage taper. The first stage has two sections: a tapered section (L_1) and a non-tapered section (L_2). The tapered section has a starting diameter r_1 and an ending diameter r_2. The second non-tapered section has a diameter r_2. The core of this first section has a refractive index n_1, and the cladding has a refractive index n_2. The second stage (L_3-L_4-L_5) is obtained by inserting a double-tapered inner core (tapered at both sides). This inner core has a refractive index n_2 and consists of three sections. The first section L_3 starts with a zero diameter and is tapered to an ending diameter r_3. This first section is followed by a non-tapered section L_4. Then, another tapered section of length L_5 follows, where its diameter is tapered from r_3 to zero.

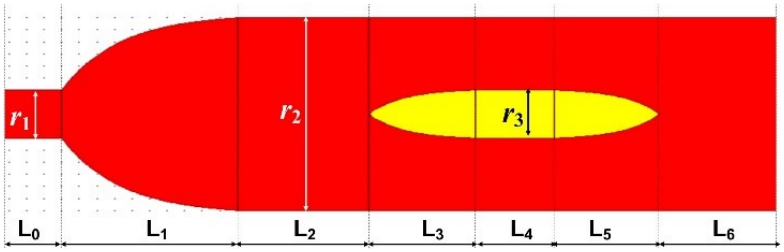

Figure B-1 Schematic diagram of the proposed mode converter.

For the mode converter to work, the power of the fundamental mode (LP_{01}) is injected at the left of the first stage (left of L_0 section). The diameter of this section (r_1) is chosen to couple easily to a single mode fiber (SMF) with a minimum coupling loss. By careful tuning of the parameters of this stage (mainly r_2, L_1, and L_2), the power transfer can be forced to occur mostly from LP_{01} to the desired LP_{0m}. However, other non-desired modes (especially those LP_{0k}, $k \neq m$) can still have a significant portion of power at the end of this stage. The second stage of the converter is then used to further enhance the desired mode conversion and reduce the conversion to other non-desired modes. The second stage has four parameters that can be tuned to obtain a high conversion efficiency from LP_{01} to the desired LP_{0m} (or low insertion loss of the desired LP_{0m} mode) and a high extinction ratio (high mode purity of the desired mode and low residual powers from the other non-desirable modes). Therefore, there are seven parameters (two diameters r_2 and r_3 and five lengths L_1 to L_5) that could be tuned for a target LP_{0m} mode.

Finding the optimal parameters for a particular LP_{0m} mode will be formulated as an optimization problem, where the objective function to minimize is the mode insertion loss subject to a set of constraints representing the fabrication limitations. These requirements are the

minimum physical dimensions required for fabrication using 3D femtosecond laser inscription. The optimization problem formulation is discussed in the next section.

B.3 Proposed optimization method:

Problem formulation refers to the process of formulating the device designing problem to make an objective function for an artificial intelligence optimizer. For mode converter, we consider the structural parameters as the input of objective function and the Insertion Loss (*IL*) as the output of the function. The problem formulation is given by:

$$
\begin{aligned}
&Variables: \vec{x} = [L_1, L_2, L_3, L_4, L_5, r_1, r_2, r_3] \\
&Objecitve: Minimizing\ Insertion\ Loss = P_{in}/P_{0m}^{out} \\
&Variable\ range: \\
&Min(\vec{x}) = [100\ \ 0\ 50\ 0\ 50\ 8\ 20\ 0] \\
&Max(\vec{x}) = [3000\ 1500\ 2000\ 1500\ 2000\ 12\ 250\ 100]
\end{aligned}
\tag{B-1}
$$

These minimum and maximum values are obtained after discussion with the fabrication team and are in the unit of μm [168]. Note that the *IL* of mode LP_{0m} is computed as follows: $IL = P_{in}/P_{0m}^{out}$, where P_{in} is the normalized input power (in the fundamental LP_{01} mode) injected at the left of the converter and P_{0m}^{out} is the normalized power in mode LP_{0m} at the output of the converter.

B.4 Results and discussion:

To optimize the structural parameters of the device, the GWO with 60 artificial gray wolves and maximum iteration of 250 is utilized. This algorithm simulates the social behavior and leadership of grey wolves in nature and proves its performance in several fields of engineering [21]. The convergence curve for each optimization is shown in Figure B-2. In addition, the obtained optimum structural parameters for each mode converter is shown in Table B-1. The obtained results show that the proposed method is very efficient and comprehensive in finding the best value of the structural parameters. Also, the comparative study shows that there are significant improvements in the *IL*. For example, the obtained LP_{01} to LP_{02} mode converter provides an improvement of more than 50% in *IL* compared to the one presented in [170].

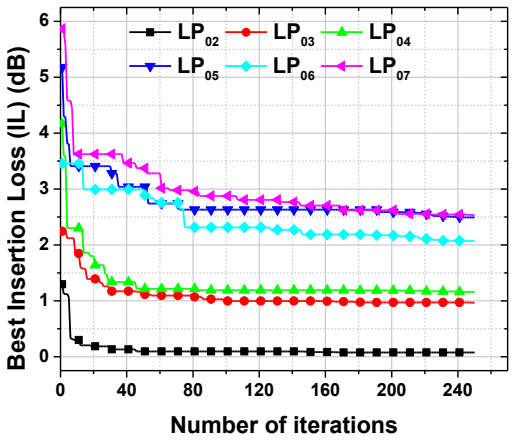

Figure B-2 GWO convergence curves for each LP_{01} to LP_{0m} converter.

Table B-1 Obtained optimal structural parameters for the mode converters.

LP_{01} to	L_1	L_2	L_3	L_4	L_5	r_1	r_2	r_3	IL (at 1550nm)
LP_{02}	1179	114	167	95	1337	10	82	11	0.1
LP_{03}	1359	3	418	4	1833	12	115	15	1
LP_{04}	2898	373	105	1244	2000	12	80	71	1.2
LP_{05}	121	763	1424	300	542	12	147	47	2.5
LP_{06}	1414	388	557	53	589	12	163	100	2
LP_{07}	2482	26	100	290	917	12	213	92	2.5

All dimension parameters are in the unit of μm.

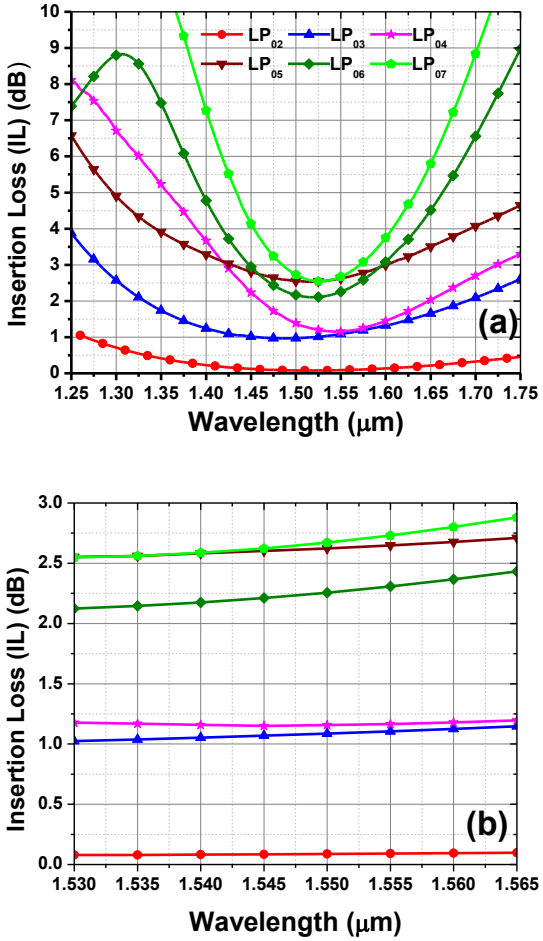

Figure B-3 Insertion loss (IL) of LP_{0m} modes at the output of mode converter (a) over a broadband, and (b) over the C-band.

Figure B-3 shows the IL of the several LP_{0m} modes. Figure B-3(a) indicates that the obtained mode converters can operate over a broad bandwidth. For instance, LP_{01}-LP_{02} mode converter can be used over the O-, E-, S-, C- and L-bands for an IL less than 1 dB. The same bandwidth can be obtained for the LP_{01}-LP_{03} mode converter with a maximum IL of 3.5 dB. More interestingly, Figure B-3(b) demonstrates that all the designed mode converters could span the C-band (from 1530 to 1565 nm) with an IL not exceeding 3 dB.

B.5 Conclusion

In this chapter, we have presented an optimization algorithm based on utilizing artificial intelligence techniques to design mode converter structures automatically. As a case study, a mode converter structure has been designed to convert LP_{01} to LP_{0m} (m=2, …, 7). The obtained mode converters can operate in a broad bandwidth. The optimization takes into consideration the fabrication limitation of the devices by respecting a set of fabrication rules in terms of minimum dimensions. The results have revealed the optimization approach is effective in designing such complex devices. It has also been shown that the obtained device insertion loss outperforms similar structures by a factor of 50%. In addition, the optimizer allows the designers to optimize complex structures with multiple merit factors.

Appendix C: Optimization Framework for Designing Photonic Crystal Sensors

C.1 Introduction

This appendix is based on the paper published in the Journal of Journal of Applied Optics [6]. To date, Photonic Crystal (PhC) devices have become popular because they cover a wide range of applications. PhC structures show bandgaps in their spectral transmission performance. By creating defects in the PhC lattice, some leaky modes will be generated in the bandgap region. In other words, these leaky modes provide the opportunity to manipulate the transmitted light [14].

The use of a leaky mode to implement optical filters is one of the most standard applications of PhC structures. This leaky mode provides a very narrow bandpass filter that could be used in a wide range of applications. In this chapter, a PhC sensor, based on the optical filtering operation of a PhC structure, is designed with the proposed optimization method. In such structures, a PhC slab with some air holes is usually considered as the sensing device. Hence, sensing operation is performed by filling the air holes with the designated material and measuring the wavelength shift in the output spectrum of the filter [171].

The main problem inherent with the use of such devices is how to model the internal propagation light. In other words, finding an analytical equation describing the relationship between the structural parameters and the device output performance is usually very challenging, and in many cases it is impossible. The complexity of the relationship between the structural parameters and the device output performance prevents researchers from proposing analytic methods to design such devices.

The typical method utilized in this field to design such devices is trial and error; that is, the structural parameters are manipulated, then the behavior of the device is observed, and these observations are used to estimate the approximate relation between the structural parameters and the device output. This method requires a huge amount of human involvement with tedious non-systematic efforts. Moreover, the finally designed device is usually far from the optimal one. The trial and error process have been followed in many works in the field of PhC devices [93]–[95], [97], [98], [172]. Many PhC filter structures, such as PhC cavity [102], PhC ring resonator [99]–[101], and defect-mode based PhC filter [103], have been designed by this approach. More specifically, PhC liquid sensors that we aim to concentrate on here have been designed manually, which leads to be far from the optimal designs [173], [174].

To solve the problem of the lack of an automatic and comprehensive method for designing PhC devices, use of artificial intelligence techniques has been proposed. Up to date, the Quality factor (Q) of PhC cavity has been maximized by genetic algorithms [104]–[106]. In ref.[108], PhC notch-filter has been designed by the particle swarm optimization algorithm. The bend loss of PhC waveguide has been minimized by use of a genetic algorithm [107]. The Extraction ratio and Purcell factor of PhC LEDs have been maximized using a multi-objective grey wolf optimizer [65]. Furthermore, the slow light properties of PhC waveguides have been optimized using similar optimization algorithms [66]–[72].

Recently, comprehensive frameworks for designing PhC filters have been proposed [2], [62]. In these frameworks, the optimal designs have sharp, well-tuned, and low crosstalk output completely, suitable for all filter applications. However, for the application of PhC sensors based on PhC filters, the sensitivity of the sensors must be evaluated and considered in addition to other

merit factors. Therefore, in this chapter we upgrade the multi-objective optimization framework for the application of PhC sensor design, in which the sensitivity will be maximized as well as other merit factors. In the rest of the chapter, the process of this framework is explained with an example of designing a PhC liquid sensor.

C.2 PhC Sensor Structure and Related Issues

The proposed structure of liquid sensor is shown in Figure C-1. The structure consists of a silicon slab with some holes in it to form a waveguide and a cavity section. The cavity is made by eight holes. The light will enter the device from the left side. The device has optical filtering characteristic and the spectral transmission characteristic can be examined at the right side output. Filling the holes with Oil (n=1.45) or water (n=1.33) will result in a shift in the output spectral transmission performance. This is the principle for utilizing this structure as a liquid sensor [173], [174].

Before designing the cavity section, it is necessary to design the photonic crystal lattice to have the largest photonic band gap as a large photonic bandgap provides a wider working wavelength window to design filters. In order to calculate the photonic bandgap of the PhC lattice, the 2D Plane Wave Expansion (PWE) with a slab equivalent index method is utilized [175]. We consider a Silicon-On-Insulator (SOI) slab with 400 *nm* thickness of silicon slab, which corresponds to a slab equivalent index of 3.18 for a Transverse Electric (TE) polarized mode [176]. In addition, we consider that the holes are normally filled with Oil (n=1.45) [173]. By sweeping the filling factor ($f=r/a$, where a is the lattice constant and r is the hole radius) from 0 to 0.5, we conclude that at f = 0.41, the largest photonic bandgap will be achieved. However, we consider f=0.375 which provides a large enough bandgap and a more mechanically rigid PhC slab. In addition, the central normalized frequency of the photonic bandgap is set 0.389. Therefore, the lattice constant is $a = 0.280 \cdot 1550 = 433\ nm$.

The idea of realizing a filter by modifying a PhC lattice comes from the fact that introducing defects in PhC lattice causes leaky modes in the photonic bandgap. These leaky modes provide an opportunity to utilize the structure as a narrow bandpass filter. In other words, the leaky mode guides a narrow band of spectrum. Therefore, such structures can be utilized as narrow bandpass filters. To tune the leaky mode, it is necessary to modify the defect structure. In our case, we use holes as a defect region to create the leaky modes.

The more holes involved in defect region, the more flexible the PhC sensor structure is, and the more complex and difficult designing such structures becomes. Here, we consider eight holes as the defect region to manipulate the guided light, which is large enough to provide sufficient flexibility in the design and to show our approach.

In order to evaluate the performance of the device, the output spectral transmission performance is calculated by a 2D FDTD simulation for TE-polarization. As a sample case study, the output of the device is shown in Figure C-2. To design a PhC sensor, four merit factors must be considered:

- Amp_c: Maximum amplitude of the output in the main band.
- Amp_s: Maximum amplitude of the output in the sidebands.
- *Deviation*: The deviation of the central wavelength of the output peak (λ_c) to the defined central wavelength of the channel (λ_O) ($Deviation = |\lambda_{c1} - \lambda_O|$).
- *Sensitivity:* the ratio of change in the central wavelength of the output peak (λ_c) divided

by change in the refractive index of the filed holes ($Sensitivity = \left|\frac{\lambda_{c2}-\lambda_{c1}}{n_2-n_1}\right|$).

The first three factors are three of which are directly related to the performance of the filtering operation [2], [62], while the sensitivity is a criterion specific to a sensor. The above five parameters of Amp_c, Amp_s, λ_O, λ_{c1}, and λ_{c2} are illustrated in Figure C-2.

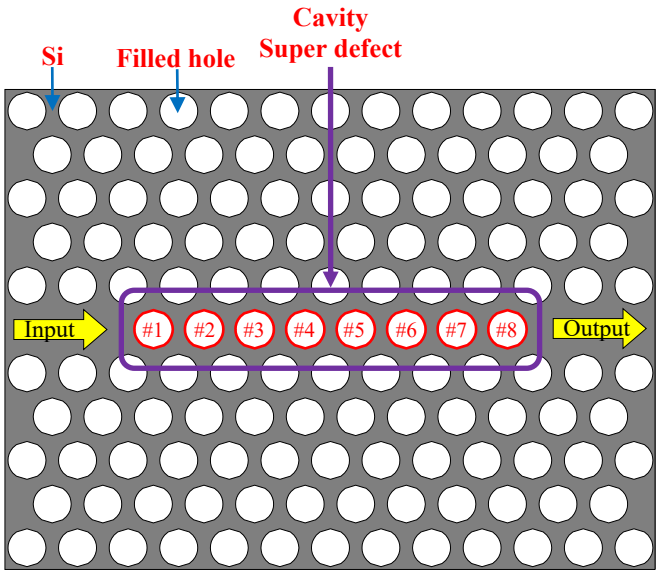

Figure C-1 Proposed PhC liquid sensor. Eight holes are used to form the super defect region.

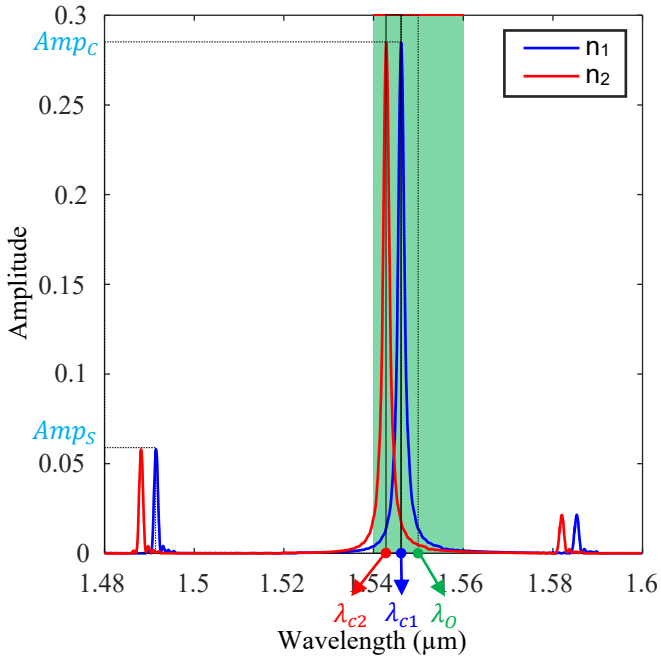

Figure C-2 Output spectral transmission performance of an example of a PhC liquid sensor.

C.3 Multi-objective optimization frameworks for designing PhC Sensors

As mentioned before, it is very difficult to find analytical methods; we can sweep the search space or utilize an optimizer algorithm to find the best possible designs. If a design shows high *Ampc* and *Sensitivity* with low *Amps* and *Deviation*, it means that it is a well-designed PhC sensor. Therefore, the multi-objective optimizer looks for the designs in which *Ampc* and *Sensitivity* are

maximized while Amp_s and *Deviation* are minimized. The framework can be divided in three main modules: Parameters Module, Constraints Module and Optimizer Module, illustrated by Figure C-3.

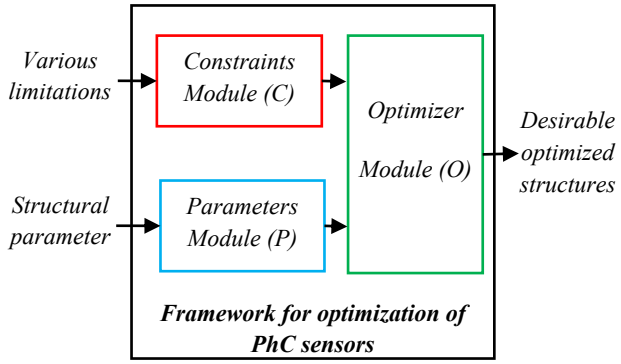

Figure C-3 Proposed multi-objective optimization framework for designing PhC sensors.

A. Parameters Module (P)

In this module, the structural parameters must be defined and handled. Therefore, the best values for the structural parameters will be found. The P module for the proposed PhC sensor (Figure C-1) is given by:

$$P: \vec{x} = \left[\frac{R_1}{a}, \frac{R_2}{a}, \frac{R_3}{a}, \frac{R_4}{a}, \frac{R_5}{a}, \frac{R_6}{a}, \frac{R_7}{a}, \frac{R_8}{a}\right] \tag{C-1}$$

B. Constraints Module (C)

All of the issues that must be considered during the PhC sensor design are considered in this module. For this case study, two groups of constraints are considered to address the issues. The first group (C_1) is related to the parameters ranges. In addition, any manufacturing limitations could be added to this group. The second group (C_2) is for checking the validity of the filtering operation of the device. The C module for the proposed PhC sensor (Figure C-1) is given by:

$$\begin{gathered} C = [C_1, C_2], \\ C_1: 0 \le \frac{R_1}{a}, \dots, \frac{R_8}{a} \le 0.5, \\ C_2: Amp_{c1} > Amp_{s1}\ , \\ Amp_{c2} > Amp_{s2} \end{gathered} \tag{C-2}$$

The index of 1 and 2 of the C_2 section indicates the number of the device simulation.

C. Optimizer Module (O)

Objective functions and an optimizer should be identified for this module: in order to solve the problem with single objective optimization approach, a new merit factor, a combination of the previous merit factors, is defined as:

$$Objective = Amp_{C1} + Sensitivity + \frac{1}{Amp_S + Deviation} \tag{C-3}$$

The single objective optimizer will try to maximize this parameter. As the Objective is maximized, a higher performance PhC sensor design is achieved. Solving the problem as a single

objective problem results in losing many decent designs since the actual answer to multi-objective problem is a set of optimal solutions.

The objectives for the multi-objective optimization approach are Amp_c, Amp_s, *Deviation*, and *Sensitivity*. The optimizer should find the PhC sensor structures in which Amp_c and *Sensitivity* are maximized while Amp_s and *Deviation* are minimized. Several single- and multi-objective optimization algorithms can be used for the optimizer [22], [89], [90]. We choose the Single- and Multi-Objective Grey Wolf Optimizer (SOGWO and MOGWO) algorithm for the optimizer [21], [24], [91]. This algorithm mimics the social behavior and leadership of grey wolves in nature. This algorithm proved its performance in several fields of engineering. The main motivation to choose Grey Wolf Optimizer is the high local optima avoidance, since the problem that is investigated in this work has a large number of variables, resulting in a very difficult task to explore the search space with many local solutions [92].

It is worth mentioning here that there is no single solution for multi-objective problems due to the nature of such problems. A set of optimal solutions (Pareto-optimal set) is the answer to multi-objective problems. They represent the best trade-offs between the objectives [73].

A flow chart of how to calculate the merit factors is shown in Figure C-4. The reason why $-Amp_{s1}$ and $-deviation_1$ are considered is that the multi-objective optimizer tries to maximize the outputs of the objective function. By considering the negative value of an output, the direction of the behavior is changed. For Amp_{s1} and $deviation_1$, minimization is required; alternatively, for the negative $-Amp_{s1}$ and $-deviation_1$, maximization is required. Overall, all of the outputs behave in the same direction.

A candidate design, which does not satisfy the conditions that mean a valid filter device cannot be made, is what we call infeasible design. Hence, for such a design the outputs of the objective function must be a set of values, which are much worse than that of the normal valid designs. In this case, we consider Output=-100 for the single objective optimization approach and Output=[-100 -100 -100 -100] for the multi-objective optimization approach. In order to calculate the merit factors, two simulations are required (one with oil as the external medium and one with another liquid). For infeasible designs, we bypass the second simulation, since it does not provide any valuable information.

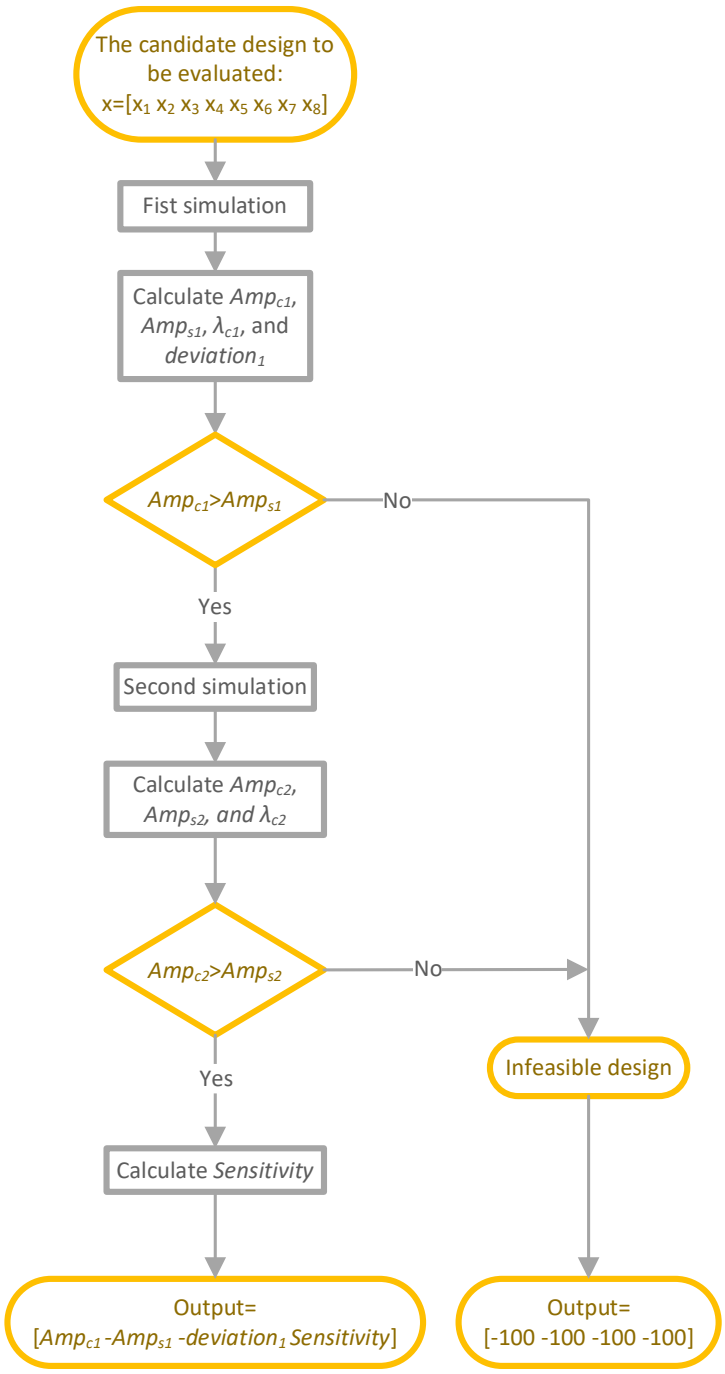

Figure C-4 Flowchart for the calculation of merit factors (the objective function of multi-objective optimization approach).

C.4 Results and discussion

After setting up each module, the framework is ready to optimize the proposed PhC sensor. Basically, the optimizer checks different possible combination of the structural parameter values to achieve high-performance design(s).

Single-objective optimization approach:

In order to perform the single-optimization, we have utilized SOGWO with 60 artificial grey

wolves and maximum iteration of 400 to approximate the global optimum. The optimizer just considers the Objective function as $Objective = Amp_{C1} + Sensitivity + \frac{1}{Amp_S + Deviation}$ and manipulates the structural parameters until the best value of the Objective is found. The results of single-objective optimization approach are shown as a convergence curves in Figure C-5. SOGWO, Particle Swarm Optimization (PSO) [18], [19], and Genetic Algorithm (GA) [20] were utilized to optimize this problem. The comparative study shows that SOGWO gives better results than the others. Therefore, the results of SOGWO with iterations are shown in Table C-1, and correspondingly the output spectral transmission performance of the obtained designed filter is given in Figure C-6. It is seen that the transmission spectrum performance is better and better with the increase of iterations. It is also shown that single-objective optimization is not the best way to solve this problem. This motivates us to solve the problem with multi-objective optimization approach.

Table C-1 Properties of obtained structures with single-objective optimization by SOGWO

Iter	R_1	R_2	R_3	R_4	R_5	R_6	R_7	R_8	Amp_C	$-Amp_S$	-D(nm)	Sen	Obj
1	63	105	154	178	199	32	150	99	0.0003	-0.0001	-0.53	0.285	1.6
3	217	156	175	186	118	3	134	77	0	0	-0.38	0.613	2.1
7	120	164	103	53	0	110	0	27	0.0134	-0.0113	-0.3	0.172	3
20	170	137	26	217	94	131	25	5	0.0788	-0.0052	-0.15	0.277	6.1
22	217	154	0	188	201	68	31	0	0.0721	-0.0018	-0.15	0.24	6.3
24	202	128	27	217	106	217	58	6	0.001	0	-0.15	0.255	6.4
33	162	89	84	217	90	77	40	41	0.0537	-0.0249	-0.08	0.27	9.7
50	217	10	8	180	50	143	46	33	0.0325	-0.0267	0	0.247	37.1
147	217	127	13	150	25	187	51	30	0.0288	-0.0124	0	0.21	80.7
283	214	128	10	134	34	196	62	22	0.0389	-0.0108	0	0.217	92.6
287	217	136	9	139	38	183	71	23	0.035	-0.0099	0	0.217	100.8
308	217	129	8	126	34	203	73	30	0.0495	-0.0093	0	0.217	107.2
337	213	129	8	120	36	208	73	27	0.055	-0.0089	0	0.217	111.8
341	217	140	9	130	35	193	74	22	0.0435	-0.0086	0	0.21	116.4
354	217	139	9	128	35	197	74	22	0.0461	-0.0084	0	0.217	118.5
370	210	148	9	120	36	200	74	22	0.0486	-0.0079	0	0.202	125.8
374	211	148	9	120	37	198	75	22	0.0487	-0.0079	0	0.21	125.9
379	213	141	10	118	35	205	75	22	0.0528	-0.0077	0	0.202	130.1
387	212	144	9	118	35	204	75	22	0.0522	-0.0076	0	0.202	130.5
388	207	143	9	117	36	205	75	21	0.0534	-0.0076	0	0.202	131.1
390	209	143	9	117	36	204	75	22	0.0535	-0.0076	0	0.21	131.2
393	210	144	9	116	36	204	76	22	0.0542	-0.0074	0	0.202	134.9
394	215	146	9	116	36	203	77	22	0.0538	-0.0073	0	0.202	137.3
397	214	145	9	118	36	202	78	22	0.0545	-0.0072	0	0.202	138.5
398	212	145	9	117	36	203	78	22	0.0553	-0.0072	0	0.202	139.3

The unit of R_x is *nm*.

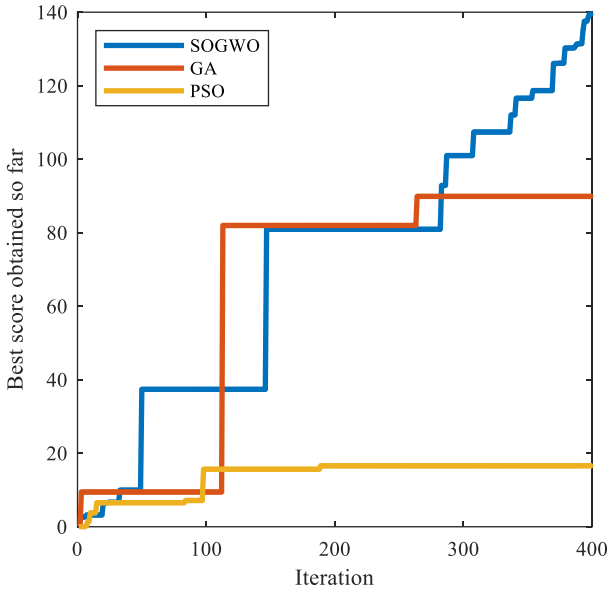

Figure C-5 Convergence curve of single-objective optimization approach.

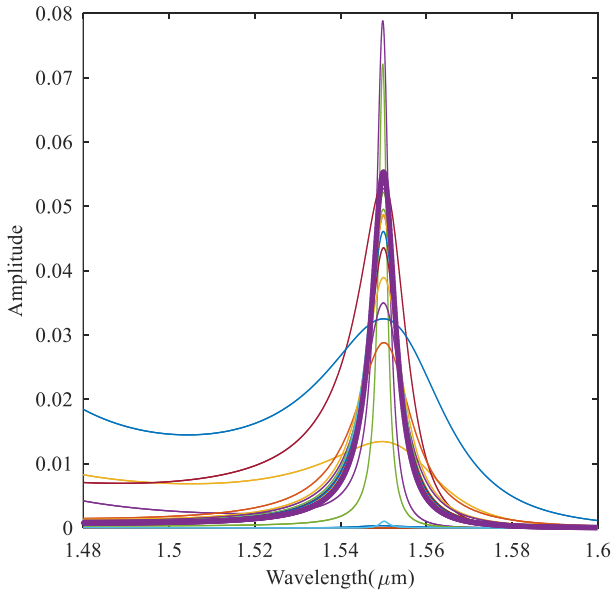

Figure C-6 Output spectral transmission performance of the PhC sensor designs of Table C-1. The purple/thick curve indicates the spectrum at the end of optimization, the best design with singe-objective optimization approach.

Multi-objective optimization approach:

The Amp_c, Amp_s. Deviation, and *Sensitivity* show a conflicting behavior. Therefore, it means that this problem is intrinsically multi-objective. Since there is no single solution for such problem, solving the problem with just single objective optimization approach, in which the combined result of merit factors is considered, causes to find only a member of the set of optimum solutions.

Since the output of the many designs in the search space does not satisfy the condition *of* $Amp_{c1}>Amp_{s1}$, second simulation has been bypassed, significantly decreasing the total run time of the optimization.

Finally, the optimization ends up with 100 optimal designs. Since calculating the four merit factors requires two simulations, the second simulation is done to calculate the Sensitivity. Therefore, in order to simplify the plot, the output spectral transmission performance for the first simulation of the optimal designs are depicted in Figure C-7. The best and the worst designs with respect to each of the merit factors are shown in Figure C-8. As it can be seen, the range of optimal designs is so wide. As it is already mentioned, all of the solution of the Pareto-optimal set are optimal and no one is better than the others. Hence, we need to choose a design in which the best trade-off has been established between the merit factors. To select a design from the set of optimal designs, firstly, we omit the designs in which the Amp_{c1} of them are very low as they transmit a low portion of optical power. Secondly, we omit the designs in which the ratio=Amp_{c1}/ Amp_{s1} is very low. Designs with a ratio lower than 40 have been omitted. Therefore, 33 optimal designs remain, which are shown in Table C-2. The output spectral transmission performance of the first simulation of the remaining 33 designs is depicted in Figure C-9 and zoom-in in Figure C-10.

Among the few remaining optimal designs, the design that provides the highest sensitivity is the best choice for liquid sensor application, i.e. structure #1 in Table C-2. The output spectral transmission performances of the selected design (i.e. structure #1) and the physical geometry of the device are shown in Figure C-11 and 12 respectively. It is also seen that a slight change of filling material refractive index results in a clear shift of output transmission spectrum. In addition, the simulation results for a design of filling the holes with Oil (n=1.45) and water (n=1.33) are shown in Figure C-13, and it is observed that a big shift in the output spectral transmission performance is achieved. The comparison between the designed sensor in this work and the similar works reported, the performance of this work based on the newly defined merit factors is much better than that of the similar works reported [173], [174].

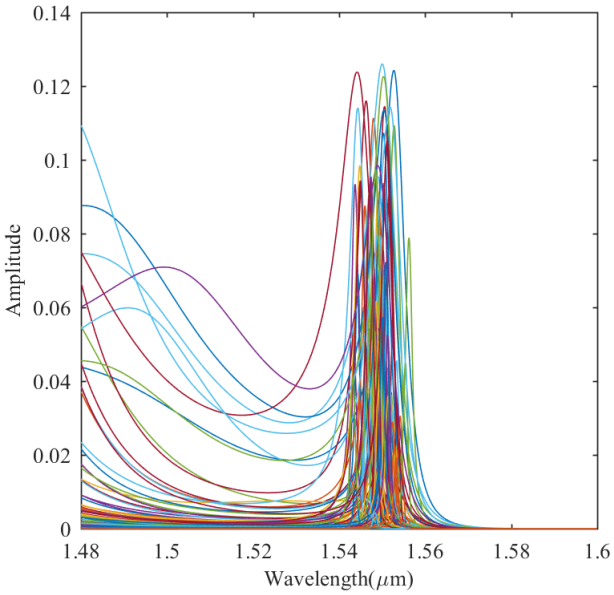

Figure C-7 Output spectral transmission performance of the 100 optimal PhC liquid sensor by first simulation.

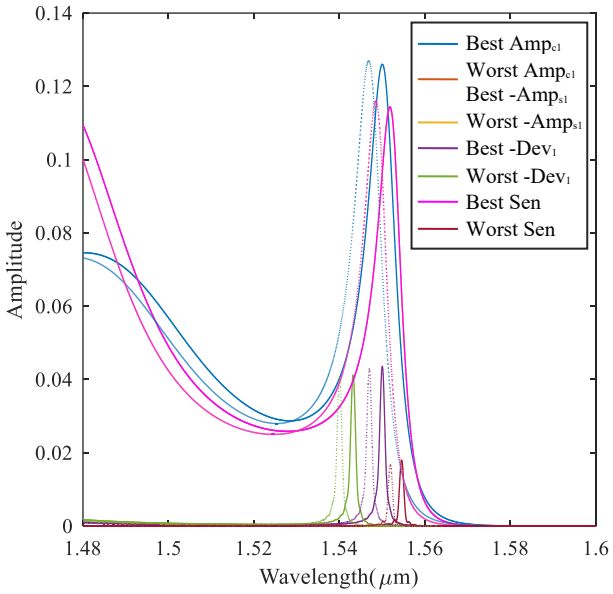

Figure C-8 Best and worst designs with respect to each of the merit factors.

Table C-2 Properties of optimum structures designed by multi-objective optimization approach.

No.	R_1	R_2	R_3	R_4	R_5	R_6	R_7	R_8	Amp_c	$-Amp_s$	$-D(nm)$	Sen
1	162	144	98	104	142	138	69	88	0.0756	-0.0017	-2.02	0.314
2	173	149	100	98	141	150	84	98	0.048	-0.0008	-0.75	0.307
3	158	137	105	97	143	148	75	92	0.0756	-0.0016	-0.22	0.307
4	171	156	96	103	137	151	72	84	0.0511	-0.0008	-2.25	0.306
5	174	145	112	94	132	168	89	89	0.0331	-0.0006	-3.07	0.306
6	176	154	102	94	136	163	75	99	0.0305	-0.0004	-4.22	0.301
7	179	157	102	96	131	167	75	99	0.0246	-0.0004	-3.69	0.301
8	167	144	101	94	150	155	79	98	0.0456	-0.0006	-3.39	0.301
9	161	138	103	94	156	159	72	111	0.0526	-0.0006	-1.28	0.3
10	171	135	95	108	141	157	57	72	0.0436	-0.0011	0	0.3
11	151	168	79	112	147	137	76	97	0.0678	-0.0008	-0.53	0.3
12	164	156	93	102	149	142	85	75	0.0537	-0.0008	-1.72	0.299
13	151	151	99	99	151	137	85	82	0.0747	-0.0014	-1.95	0.299
14	178	154	103	95	146	171	72	87	0.0346	-0.0004	-3.67	0.298
15	167	156	93	98	146	152	73	97	0.0451	-0.0005	-5.43	0.294
16	173	143	107	84	158	162	65	82	0.0341	-0.0003	-3.54	0.294
17	177	174	98	91	146	151	81	101	0.0228	-0.0003	-2.86	0.293
18	162	144	97	95	159	167	63	99	0.0289	-0.0003	-2.41	0.293
19	166	152	104	85	164	162	72	107	0.0363	-0.0002	-2.18	0.293
20	173	160	101	94	144	152	74	95	0.0342	-0.0004	-1.05	0.293
21	161	164	80	112	145	140	59	74	0.0567	-0.0008	-0.38	0.292
22	160	157	83	110	148	138	68	84	0.0574	-0.0008	-0.08	0.292
23	159	170	76	116	144	132	73	78	0.0676	-0.001	-0.08	0.292
24	170	153	89	107	147	146	59	88	0.0511	-0.0005	-0.67	0.292
25	174	164	94	96	156	155	65	89	0.0361	-0.0003	-1.43	0.292
26	178	163	108	85	151	162	77	98	0.0212	-0.0002	-1.43	0.292
27	173	164	77	119	139	137	65	84	0.0616	-0.0008	-1.43	0.292
28	181	165	115	80	150	160	61	68	0.0124	-0.0001	-1.58	0.292
29	172	166	97	89	155	169	75	116	0.0193	-0.0002	-3.23	0.286
30	172	163	98	87	164	161	75	83	0.0208	-0.0002	-3.08	0.286
31	195	155	108	81	162	173	55	82	0.0184	-0.0001	-0.23	0.285
32	183	165	94	96	153	163	63	96	0.0305	-0.0002	-1.13	0.284
33	192	184	77	95	179	165	42	103	0.018	-0.0001	-4.52	0.264

The unit of R_x is *nm*.

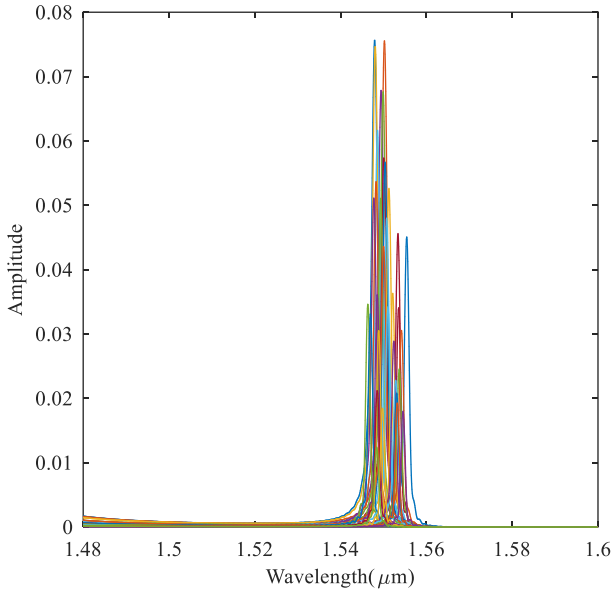

Figure C-9 Output spectral transmission performance of the optimal PhC liquid sensors of Table C-2 by first simulation.

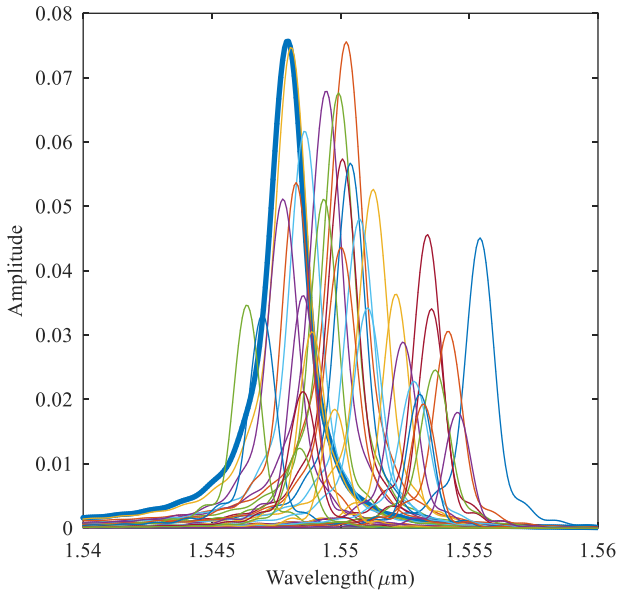

Figure C-10 Zoom-in output spectral transmission performance of the optimal PhC liquid sensors of Table C-2 by first simulation. The thick curve indicates the design has higher sensitivity than the others.

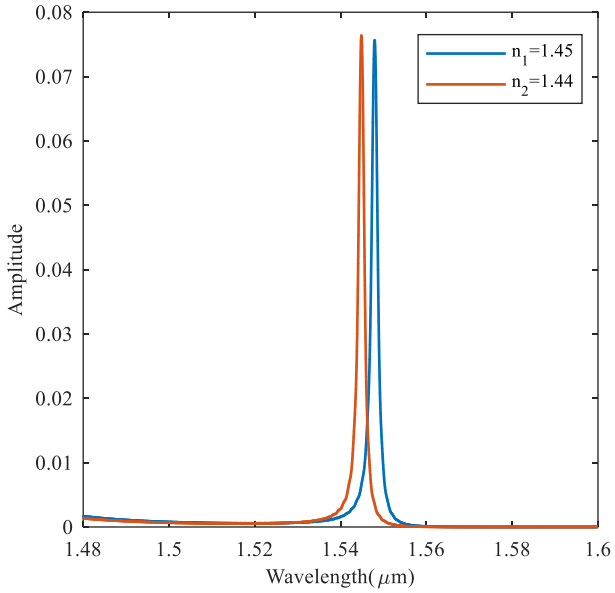

Figure C-11 Output spectral transmission performance of the selected optimal PhC liquid sensor by two simulations with different filler materials.

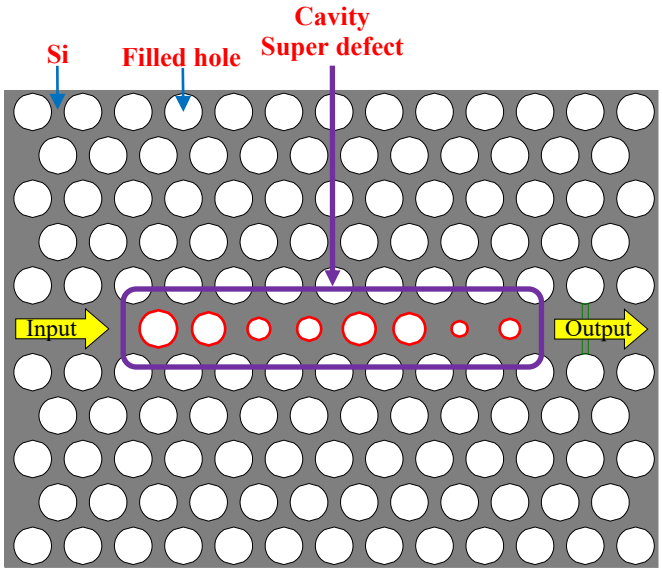

Figure C-12 Physical geometry of the obtained PhC liquid sensor.

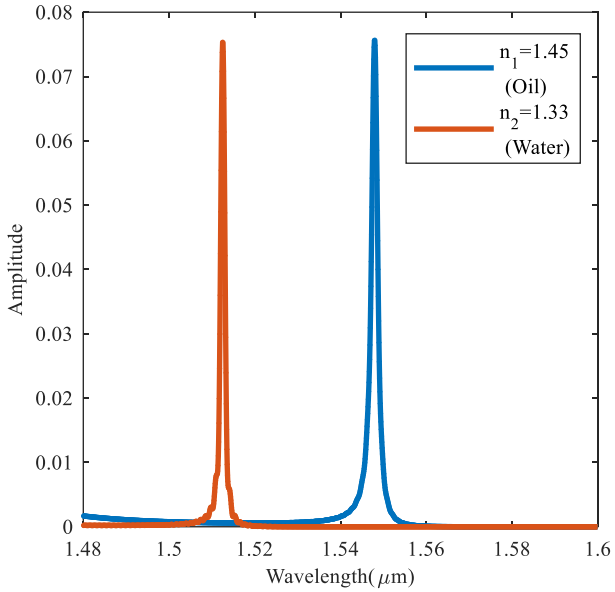

Figure C-13 Output spectral transmission performance of the selected optimal PhC liquid sensor in real application.

The method proposed in this study, which is able to automatically find a high-performance design, has two main advantages. First, using a large defect with several free parameters provides much flexibility in manipulating the guided light through the defect. Second, using a systematic multi-objective optimization method allows finding a wide range of optimal designs without human involvement.

To summarize, the multi-objective optimization technique is a straightforward and comprehensive method for designing complex super-defect PhC liquid sensors with a large number of structural parameters. Moreover, this method opens up a way towards designing new and very high-performance PhC Sensors, which work based on the wavelength shift in the output of the PhC filters.

The designed PhC liquid sensor requires *1 nm* manufacturing resolution. Considering the fabrication process of PhC structures reported in [112], [113], this structure should be feasible to build.

C.5 Conclusion

In summary, the case study investigated here has shown that the proposed multi-objective framework can effectively design and optimize the structure of a newly introduced PhC liquid sensor. The proposed framework can design any complicated super-defect PhC sensors. Several structures can be designed with respect to any application. No initial design and human involvement are required to start the optimization process. Moreover, any manufacturing limitation can be added in the constraints module. Various multi-objective algorithms can be easily used in optimizer module to achieve the optimal designs. Finally, the proposed multi-objective framework opens up an effective way for designing very high-performance PhC sensors.

References

[1] S. M. Mirjalili, H. Taleb, M. Z. Kabir, and P. Bianucci, "Design optimization of orbital angular momentum fibers using the gray wolf optimizer," *Appl. Opt.*, vol. 59, no. 20, pp. 6181–6190, 2020, doi: 10.1364/AO.391731.

[2] S. M. Mirjalili, B. Merikhi, S. Z. Mirjalili, M. Zoghi, and S. Mirjalili, "Multi-objective versus single-objective optimization frameworks for designing photonic crystal filters," *Appl. Opt.*, vol. 56, no. 34, pp. 9444–9451, 2017, doi: 10.1364/AO.56.009444.

[3] B. Merikhi, S. M. Mirjalili, M. Zoghi, S. Z. Mirjalili, and S. Mirjalili, "Radiation pattern design of photonic crystal LED optimized by using multi-objective grey wolf optimizer," *Photonic Netw. Commun.*, vol. 38, no. 1, pp. 167–176, 2019, doi: 10.1007/s11107-019-00843-1.

[4] K. Rashidi, S. M. Mirjalili, H. Taleb, and D. Fathi, "Optimal Design of Large Mode Area Photonic Crystal Fibers Using Multi-Objective Gray Wolf Optimization Technique," *J. Light. Technol.*, vol. 36, no. 23, pp. 5626–5632, 2018, doi: 10.1109/JLT.2018.2877925.

[5] H. Mellah, S. M. Mirjalili, and X. Zhang, "Design Optimization of Waveguide-Based LP 01 to LP 0m Mode Converter by using artificial intelligence technique," *Electron. Lett.*, vol. 54, no. 11, pp. 703–705, 2018, doi: 10.1049/el.2018.0466.

[6] M. J. Safdari, S. M. Mirjalili, P. Bianucci, and X. Zhang, "Multi-objective optimization framework for designing photonic crystal sensors," *Appl. Opt.*, vol. 57, no. 8, pp. 1950–1957, 2018, doi: 10.1364/AO.57.001950.

[7] H. Murata, "Advanced photonic devices for 5G network in dense user environment," *Summer Top. Meet. Ser. SUM 2017*, pp. 91–92, 2017, doi: 10.1109/PHOSST.2017.8012665.

[8] L. A. Rusch, M. Rad, K. Allahverdyan, I. Fazal, and E. Bernier, "Carrying Data on the Orbital Angular Momentum of Light," *IEEE Commun. Mag.*, vol. 56, no. 2, pp. 219–224, 2018, doi: 10.1109/MCOM.2018.1700058.

[9] L. Wang *et al.*, "Linearly polarized vector modes: enabling MIMO-free mode-division multiplexing," *Opt. Express*, vol. 25, no. 10, p. 11736, 2017, doi: 10.1364/OE.25.011736.

[10] C. Brunet, B. Ung, P. A. Bélanger, Y. Messaddeq, S. LaRochelle, and L. A. Rusch, "Vector mode analysis of ring-core fibers: Design tools for spatial division multiplexing," *J. Light. Technol.*, vol. 32, no. 23, pp. 4046–4057, 2014, doi: 10.1109/JLT.2014.2361432.

[11] "'Twisted light' carries 2.5 terabits of data per second," *BBC NEWS*, 2012. https://www.bbc.com/news/science-environment-18551284.

[12] Y. Yan *et al.*, "High-capacity millimetre-wave communications with orbital angular momentum multiplexing," *Nat. Commun.*, vol. 5, pp. 1–9, 2014, doi: 10.1038/ncomms5876.

[13] "NTT successfully demonstrates 100 Gbps wireless transmission using a new principle (OAM multiplexing) as a world's first," *NTT Press Releases*, 2018. https://www.ntt.co.jp/news2018/1805e/180515a.html.

[14] B. Troia, A. Paolicelli, F. De Leonardis, and V. M. N. Passaro, "Photonic crystals for optical sensing: A review," in *Advances in Photonic Crystals*, InTech, 2013.

[15] J. C. Maxwell, "VIII. A dynamical theory of the electromagnetic field," *Philos. Trans. R. Soc. London*, no. 155, pp. 459–512, 1865.

[16] A. W. Snyder and J. Love, *Optical waveguide theory*. Springer Science & Business Media, 2012.

[17] M. J. Adams, "An Introduction to Optical Waveguides," *IEEE J. Quantum Electron.*, vol.

18, no. 11, p. 1984, 1982, doi: 10.1109/JQE.1982.1071465.
[18] J. Kennedy and R. Eberhart, "Particle swarm optimization," *Proc. ICNN'95 - Int. Conf. Neural Networks*, vol. 4, pp. 1942–1948, 1995, doi: 10.1109/ICNN.1995.488968.
[19] R. Eberhart and J. Kennedy, "A new optimizer using particle swarm theory," *MHS'95. Proc. Sixth Int. Symp. Micro Mach. Hum. Sci.*, pp. 39–43, 1995, doi: 10.1109/MHS.1995.494215.
[20] L. D. Davis and M. Mitchell, "Handbook of Genetic Algorithms," *VAN NOSTRAND REINHOLD*, vol. 15, no. 1, pp. 4–6, 1991, doi: 10.1109/LCOMM.2010.102810.101700.
[21] S. Mirjalili, S. M. Mirjalili, and A. Lewis, "Grey Wolf Optimizer," *Adv. Eng. Softw.*, vol. 69, pp. 46–61, Mar. 2014, doi: 10.1016/j.advengsoft.2013.12.007.
[22] S. Mirjalili, A. H. Gandomi, S. Z. Mirjalili, S. Saremi, H. Faris, and S. M. Mirjalili, "Salp Swarm Algorithm: A bio-inspired optimizer for engineering design problems," *Adv. Eng. Softw.*, vol. 114, pp. 163–191, 2017, doi: 10.1016/j.advengsoft.2017.07.002.
[23] S. Mirjalili and S. M. Mirjalili, "Nature-Inspired Optimizers." http://www.alimirjalili.com/Projects.html.
[24] S. Mirjalili, S. Saremi, S. M. Mirjalili, and L. dos S. Coelho, "Multi-objective grey wolf optimizer: A novel algorithm for multi-criterion optimization," *Expert Syst. Appl.*, vol. 47, pp. 106–119, Apr. 2016, doi: http://dx.doi.org/10.1016/j.eswa.2015.10.039.
[25] L. D. Mech, "Alpha status, dominance, and division of labor in wolf packs," *Can. J. Zool.*, vol. 77, no. 8, pp. 1196–1203, 1999.
[26] C. Muro, R. Escobedo, L. Spector, and R. P. Coppinger, "Wolf-pack (Canis lupus) hunting strategies emerge from simple rules in computational simulations," *Behav. Processes*, vol. 88, no. 3, pp. 192–197, 2011.
[27] L. P. Madin, "Aspects of jet propulsion in salps," *Can. J. Zool.*, vol. 68, no. 4, pp. 765–777, 1990, doi: 10.1139/z90-111.
[28] P. A. Anderson and Q. Bone, "Communication between individuals in salp chains. II. Physiology," *Proc. R. Soc. London. Ser. B. Biol. Sci.*, vol. 210, no. 1181, pp. 559–574, 1980, doi: 10.1098/rspb.1980.0153.
[29] V. Andersen and P. Nival, "A model of the population dynamics of salps in coastal waters of the Ligurian Sea," *J. Plankton Res.*, vol. 8, no. 6, pp. 1091–1110, 1986, doi: 10.1093/plankt/8.6.1091.
[30] N. Henschke, J. A. Smith, J. D. Everett, and I. M. Suthers, "Population drivers of a Thalia democratica swarm: Insights from population modelling," *J. Plankton Res.*, vol. 37, no. 5, pp. 1074–1087, 2014, doi: 10.1093/plankt/fbv024.
[31] D. H. Wolpert and W. G. Macready, "No free lunch theorems for optimization," *IEEE Trans. Evol. Comput.*, vol. 1, no. 1, pp. 67–82, 1997, doi: 10.1109/4235.585893.
[32] C. A. C. Coello, G. T. Pulido, and M. S. Lechuga, "Handling Multiple Objectives With Particle Swarm Optimization," *Ieee Trans. Evol. Comput.*, vol. 8, no. 3, pp. 256–279, 2004, doi: 10.1109/TEVC.2004.826067.
[33] J. H. Chang, A. Corsi, L. A. Rusch, and S. LaRochelle, "Design Analysis of OAM Fibers Using Particle Swarm Optimization Algorithm," *J. Light. Technol.*, vol. 38, no. 4, pp. 846–856, 2020, doi: 10.1109/JLT.2019.2945870.
[34] D. J. Richardson, J. M. Fini, and L. E. Nelson, "Space-division multiplexing in optical fibres," *Nat. Photonics*, vol. 7, no. 5, pp. 354–362, 2013, doi: 10.1038/nphoton.2013.94.
[35] A. Al Amin, A. Li, S. Chen, X. Chen, G. Gao, and W. Shieh, "Dual-LP_11 mode 4x4 MIMO-OFDM transmission over a two-mode fiber," *Opt. Express*, 2011, doi: 10.1364/oe.19.016672.

[36] S. Randel *et al.*, "6×56-Gb/s mode-division multiplexed transmission over 33-km few-mode fiber enabled by 6×6 MIMO equalization," *Opt. Express*, 2011, doi: 10.1364/oe.19.016697.
[37] N. Bai *et al.*, "Mode-division multiplexed transmission with inline few-mode fiber amplifier," *Opt. Express*, 2012, doi: 10.1364/oe.20.002668.
[38] J. van Weerdenburg *et al.*, "10 Spatial mode transmission using low differential mode delay 6-LP fiber using all-fiber photonic lanterns," *Opt. Express*, 2015, doi: 10.1364/oe.23.024759.
[39] J. Van Weerdenburg *et al.*, "138 Tbit/s Transmission over 650 km Graded-Index 6-Mode Fiber," 2017, doi: 10.1109/ECOC.2017.8346085.
[40] N. K. Fontaine *et al.*, "30×30 MIMO transmission over 15 spatial modes," 2015, doi: 10.1364/ofc.2015.th5c.1.
[41] R. Ryf *et al.*, "23 Tbit/s transmission over 17-km conventional 50-μm graded-index multimode fiber," 2014, doi: 10.1109/OFC.2014.6887221.
[42] D. Soma, Y. Wakayama, K. Igarashi, and T. Tsuritani, "Partial MIMO-based 10-mode-multiplexed transmission over 81km weakly-coupled few-mode fiber," 2017, doi: 10.1364/OFC.2017.M2D.4.
[43] N. Bozinovic *et al.*, "Terabit-scale orbital angular momentum mode division multiplexing in fibers," *Science (80-.).*, 2013, doi: 10.1126/science.1237861.
[44] H. Huang *et al.*, "Mode division multiplexing using an orbital angular momentum mode sorter and MIMO-DSP over a graded-index few-mode optical fibre," *Sci. Rep.*, vol. 5, no. September, pp. 1–7, 2015, doi: 10.1038/srep14931.
[45] Y. Yue *et al.*, "Mode properties and propagation effects of optical orbital angular momentum (OAM) modes in a ring fiber," *IEEE Photonics J.*, 2012, doi: 10.1109/JPHOT.2012.2192474.
[46] P. Boffi, P. Martelli, A. Gatto, and M. Martinelli, "Mode-division multiplexing in fibre-optic communications based on orbital angular momentum," *J. Opt. (United Kingdom)*, 2013, doi: 10.1088/2040-8978/15/7/075403.
[47] R. M. Nejad *et al.*, "Mode Division Multiplexing Using Orbital Angular Momentum Modes over 1.4-km Ring Core Fiber," *J. Light. Technol.*, vol. 34, no. 18, pp. 4252–4258, 2016, doi: 10.1109/JLT.2016.2594698.
[48] F. Feng, X. Jin, D. O'Brien, F. P. Payne, and T. D. Wilkinson, "Mode-group multiplexed transmission using OAM modes over 1 km ring-core fiber without MIMO processing," 2017.
[49] D. L. Andrews, *Structured Light and Its Applications*. Academic Press, 2008.
[50] C. Brunet, B. Ung, L. Wang, Y. Messaddeq, S. LaRochelle, and L. A. Rusch, "Design of a family of ring-core fibers for OAM transmission studies," *Opt. Express*, vol. 23, no. 8, p. 10553, 2015, doi: 10.1364/OE.23.010553.
[51] B. Ung, P. Vaity, L. Wang, Y. Messaddeq, L. A. Rusch, and S. LaRochelle, "Few-mode fiber with inverse-parabolic graded-index profile for transmission of OAM-carrying modes," *Opt. Express*, vol. 22, no. 15, p. 18044, 2014, doi: 10.1364/oe.22.018044.
[52] G. Zhu *et al.*, "Scalable mode division multiplexed transmission over a 10-km ring-core fiber using high-order orbital angular momentum modes," *Opt. Express*, 2018, doi: 10.1364/oe.26.000594.
[53] W. Tian, H. Zhang, X. Zhang, L. Xi, W. Zhang, and X. Tang, "Optical Fiber Technology A circular photonic crystal fiber supporting 26 OAM modes," *Opt. Fiber Technol.*, vol. 30, pp. 184–189, 2016, doi: 10.1016/j.yofte.2016.07.009.

[54] S. Li and J. Wang, “A compact trench-assisted multi-orbital-angular-momentum multi-ring fiber for ultrahigh-density space-division multiplexing (19 rings × 22 modes),” *Sci. Rep.*, 2014, doi: 10.1038/srep03853.
[55] S. Ramachandran and P. Kristensen, “Optical vortices in fiber,” *Nanophotonics*, vol. 2, no. 5–6, pp. 455–474, 2013, doi: 10.1515/nanoph-2013-0047.
[56] C. Brunet, P. Vaity, Y. Messaddeq, S. LaRochelle, and L. A. Rusch, “Design, fabrication and validation of an OAM fiber supporting 36 states,” *Opt. Express*, vol. 22, no. 21, p. 26117, 2014, doi: 10.1364/OE.22.026117.
[57] P. Gregg, P. Kristensen, and S. Ramachandran, “Conservation of orbital angular momentum in air-core optical fibers,” *Optica*, 2015, doi: 10.1364/optica.2.000267.
[58] P. Gregg, P. Kristensen, A. Rubano, S. Golowich, L. Marrucci, and S. Ramachandran, “Spin-orbit coupled, non-integer OAM fibers: Unlocking a new eigenbasis for transmitting 24 uncoupled modes,” 2016, doi: 10.1364/cleo_at.2016.jth4c.7.
[59] P. Gregg, P. Kristensen, and S. Ramachandran, “134km OAM state propagation by recirculating fiber loop,” *Opt. Express*, 2016, doi: 10.1364/oe.24.018938.
[60] K. Ingerslev *et al.*, “12 mode, WDM, MIMO-free orbital angular momentum transmission,” *Opt. Express*, 2018, doi: 10.1364/oe.26.020225.
[61] S. Vatani, H. Taleb, S. M. Mirjalili, and M. K. Moravvej-Farshi, “Optimal Design of Mid-Infrared Reflective Optical Modulators Based on Electrically Tunable Metasurface,” in *2020 28th Iranian Conference on Electrical Engineering (ICEE)*, 2020, pp. 1–4, doi: 10.1109/ICEE50131.2020.9260883.
[62] S. M. Mirjalili and S. Z. Mirjalili, “Single-objective optimization framework for designing photonic crystal filters,” *Neural Comput. Appl.*, vol. 28, no. 6, pp. 1463–1469, Jun. 2017, doi: 10.1007/s00521-015-2147-x.
[63] S. Z. Mirjalili, S. M. Mirjalili, S. Saremi, and S. Mirjalili, “Whale Optimization Algorithm: Theory, Literature Review, and Application in Designing Photonic Crystal Filters,” in *Nature-Inspired Optimizers: Theories, Literature Reviews and Applications*, S. Mirjalili, J. Song Dong, and A. Lewis, Eds. Cham: Springer International Publishing, 2020, pp. 219–238.
[64] S. M. Mirjalili, S. Z. Mirjalili, S. Saremi, and S. Mirjalili, “Sine Cosine Algorithm: Theory, Literature Review, and Application in Designing Bend Photonic Crystal Waveguides,” in *Nature-Inspired Optimizers: Theories, Literature Reviews and Applications*, S. Mirjalili, J. Song Dong, and A. Lewis, Eds. Cham: Springer International Publishing, 2020, pp. 201–217.
[65] S. M. Mirjalili, S. Mirjalili, and S. Z. Mirjalili, “How to design photonic crystal LEDs with artificial intelligence techniques,” *Electron. Lett.*, vol. 51, no. 18, pp. 1437–1439, 2015, doi: 10.1049/el.2015.1679.
[66] S. M. Mirjalili and S. Z. Mirjalili, “Asymmetric Oval-Shaped-Hole Photonic Crystal Waveguide design by Artificial Intelligence Optimizers,” *IEEE J. Sel. Top. Quantum Electron.*, vol. 22, no. 2, p. 4900407, 2016, doi: 10.1109/JSTQE.2015.2469760.
[67] S. M. Mirjalili and S. Z. Mirjalili, “Full Optimizer for Designing Photonic Crystal Waveguides: IMoMIR framework,” *IEEE Photonics Technol. Lett.*, vol. 27, no. 16, pp. 1776–1779, 2015, doi: 10.1109/LPT.2015.2443073.
[68] S. M. Mirjalili, “SoMIR framework for designing high-NDBP photonic crystal waveguides,” *Appl. Opt.*, vol. 53, no. 18, pp. 3945–3953, 2014, doi: 10.1364/AO.53.003945.
[69] S. M. Mirjalili, S. Mirjalili, and A. Lewis, “A Novel Multi-Objective Optimization

Framework for Designing Photonic Crystal Waveguides," *Photonics Technol. Lett. IEEE*, vol. 26, no. 2, pp. 146–149, 2014, doi: 10.1109/LPT.2013.2290318.

[70] S. Saremi, S. M. Mirjalili, and S. Mirjalili, "Unit Cell Topology Optimization of Line Defect Photonic Crystal Waveguide," *Procedia Technol.*, vol. 12, pp. 174–179, Jan. 2014, doi: 10.1016/j.protcy.2013.12.472.

[71] S. M. Mirjalili, K. Abedi, and S. Mirjalili, "Optical buffer performance enhancement using Particle Swarm Optimization in Ring-Shape-Hole Photonic Crystal Waveguide," *Opt. - Int. J. Light Electron Opt.*, vol. 124, no. 23, pp. 5989–5993, Dec. 2013, doi: 10.1016/j.ijleo.2013.04.114.

[72] S. M. Mirjalili, K. Abedi, and S. Mirjalili, "Light property and optical buffer performance enhancement using particle swarm optimization in oblique ring-shape-hole photonic crystal waveguide," in *Photonics Global Conference (PGC)*, 2012, pp. 1–4, doi: 10.1109/PGC.2012.6457997.

[73] S. M. Mirjalili, S. Mirjalili, A. Lewis, and K. Abedi, "A tri-objective Particle Swarm Optimizer for designing line defect Photonic Crystal Waveguides," *Photonics Nanostructures - Fundam. Appl.*, vol. 12, no. 2, pp. 152–163, Apr. 2014, doi: 10.1016/j.photonics.2013.11.001.

[74] S. M. Mirjalili, "Ellipse-ring-shaped-hole photonic crystal waveguide," *Opt. - Int. J. Light Electron Opt.*, vol. 126, no. 1, pp. 56–60, Jan. 2015, doi: 10.1016/j.ijleo.2014.07.123.

[75] S. M. Mirjalili and S. Mirjalili, "Oval-Shaped-Hole Photonic Crystal Waveguide Design by MoMIR Framework," *Photonics Technol. Lett. IEEE*, vol. 26, no. 24, pp. 2446–2449, 2014, doi: 10.1109/LPT.2014.2302478.

[76] S. M. Mirjalili and S. Z. Mirjalili, "Issues when designing hypoellipse photonic crystal waveguides," *Infrared Phys. Technol.*, vol. 69, pp. 62–67, 2015, doi: 10.1016/j.infrared.2015.01.003.

[77] H. Li, G. Ren, Y. Gao, Y. Lian, M. Cao, and S. Jian, "Particle swarm optimization of single-mode trench-assisted bend-insensitive fibers," *IEEE Photonics Technol. Lett.*, 2015, doi: 10.1109/LPT.2015.2421032.

[78] A. Mowla and N. Granpayeh, "Optimum design of a hybrid erbium-doped fiber amplifier/fiber Raman amplifier using particle swarm optimization," *Appl. Opt.*, 2009, doi: 10.1364/AO.48.000979.

[79] S. Baskar, R. T. Zheng, A. Alphones, N. Q. Ngo, and P. N. Suganthan, "Particle swarm optimization for the design of low-dispersion fiber Bragg gratings," *IEEE Photonics Technol. Lett.*, 2005, doi: 10.1109/LPT.2004.840924.

[80] A. Corsi, J. H. Chang, L. A. Rusch, and S. Larochelle, "Design of highly elliptical core ten-mode fiber for space division multiplexing with 2 × 2 MIMO," *IEEE Photonics J.*, vol. 11, no. 2, pp. 1–10, 2019, doi: 10.1109/JPHOT.2019.2900197.

[81] R. Maruyama, N. Kuwaki, S. Matsuo, and M. Ohashi, "Relationship between Mode Coupling and Fiber Characteristics in Few-Mode Fibers Analyzed Using Impulse Response Measurements Technique," *J. Light. Technol.*, vol. 35, no. 4, pp. 650–657, 2017, doi: 10.1109/JLT.2016.2609002.

[82] R. M. Nejad, L. Wang, J. Lin, S. Larochelle, and L. A. Rusch, "The Impact of Modal Interactions on Receiver Complexity in OAM Fibers," *J. Light. Technol.*, 2017, doi: 10.1109/JLT.2017.2751248.

[83] T. Matsui, K. Nakajima, and C. Fukai, "Applicability of photonic crystal fiber with uniform air-hole structure to high-speed and wide-band transmission over conventional telecommunication bands," *J. Light. Technol.*, 2009, doi: 10.1109/JLT.2009.2030901.

[84] Y. Huang *et al.*, "Generation of Broadband High-Purity Dual-Mode OAM Beams Using A Four-Feed Patch Antenna: Theory and Implementation," *Sci. Rep.*, vol. 9, no. 1, pp. 1–10, 2019, doi: 10.1038/s41598-019-49377-6.
[85] S. Ramachandran, P. Gregg, P. Kristensen, and S. E. Golowich, "On the scalability of ring fiber designs for OAM multiplexing," *Opt. Express*, 2015, doi: 10.1364/oe.23.003721.
[86] S. Golowich, "Asymptotic theory of strong spin–orbit coupling in optical fiber," *Opt. Lett.*, vol. 39, no. 1, pp. 92–95, 2014, doi: 10.1364/OL.39.000092.
[87] P. J. Winzer, A. H. Gnauck, A. Konczykowska, F. Jorge, and J. Y. Dupuy, "Penalties from in-band crosstalk for advanced optical modulation formats," 2011, doi: 10.1364/ecoc.2011.tu.5.b.7.
[88] S. Saremi, S. M. Mirjalili, and S. Mirjalili, "Chaotic Krill Herd Optimization Algorithm," *Procedia Technol.*, vol. 12, pp. 180–185, Jan. 2014, doi: 10.1016/j.protcy.2013.12.473.
[89] C. A. Coello Coello and M. S. Lechuga, "MOPSO: A proposal for multiple objective particle swarm optimization," in *Evolutionary Computation, 2002. CEC'02. Proceedings of the 2002 Congress on*, 2002, vol. 2, pp. 1051–1056.
[90] S. Mirjalili, S. M. Mirjalili, and A. Hatamlou, "Multi-Verse Optimizer: a nature-inspired algorithm for global optimization," *Neural Comput. Appl.*, vol. 27, no. 2, pp. 495–513, 2016, doi: 10.1007/s00521-015-1870-7.
[91] S. Saremi, S. Z. Mirjalili, and S. M. Mirjalili, "Evolutionary population dynamics and grey wolf optimizer," *Neural Comput. Appl.*, vol. 26, no. 5, pp. 1257–1263, 2015, doi: 10.1007/s00521-014-1806-7.
[92] H. Faris, I. Aljarah, M. A. Al-Betar, and S. Mirjalili, "Grey wolf optimizer: a review of recent variants and applications," *Neural Comput. Appl.*, vol. 30, no. 2, pp. 413–435, Jul. 2018, doi: 10.1007/s00521-017-3272-5.
[93] M. Fu *et al.*, "Finely engineered slow light photonic crystal waveguides for efficient wideband wavelength-independent higher-order temporal solitons," *Appl. Opt.*, vol. 55, no. 14, pp. 3740–3745, 2016, doi: 10.1364/AO.55.003740.
[94] H. Sharifi, S. M. Hamidi, and K. Navi, "A new design procedure for all-optical photonic crystal logic gates and functions based on threshold logic," *Opt. Commun.*, vol. 370, pp. 231–238, 2016, doi: 10.1016/j.optcom.2016.03.020.
[95] M. Djavid and M. S. Abrishamian, "Multi-channel drop filters using photonic crystal ring resonators," *Optik - International Journal for Light and Electron Optics*, vol. 123, no. 2. Elsevier GmbH., pp. 167–170, 2012, doi: 10.1016/j.ijleo.2011.04.001.
[96] M. Y. Mahmoud, G. Bassou, and A. Taalbi, "resonator," *Opt. - Int. J. Light Electron Opt.*, pp. 10–13, 2012, doi: 10.1016/j.ijleo.2012.08.072.
[97] S. Robinson and R. Nakkeeran, "Two dimensional Photonic Crystal Ring Resonator based Add Drop Filter for CWDM systems," *Opt. - Int. J. Light Electron Opt.*, vol. 124, no. 18, pp. 3430–3435, 2013, doi: 10.1016/j.ijleo.2012.10.038.
[98] A. Rostami, F. Nazari, H. A. Banaei, and A. Bahrami, "A novel proposal for DWDM demultiplexer design using modified-T photonic crystal structure," *Photonics Nanostructures - Fundam. Appl.*, vol. 8, no. 1, pp. 14–22, 2010, doi: 10.1016/j.photonics.2009.12.002.
[99] M. Djavid, F. Monifi, a. Ghaffari, and M. S. Abrishamian, "Heterostructure wavelength division demultiplexers using photonic crystal ring resonators," *Opt. Commun.*, vol. 281, no. 15–16, pp. 4028–4032, Aug. 2008, doi: 10.1016/j.optcom.2008.04.045.
[100] F. Mehdizadeh, H. Alipour-Banaei, and S. Serajmohammadi, "Channel-drop filter based on a photonic crystal ring resonator," *J. Opt.*, vol. 15, no. 7, p. 075401, Jul. 2013, doi:

10.1088/2040-8978/15/7/075401.
[101] H. Alipour-Banaei, F. Mehdizadeh, and M. Hassangholizadeh-Kashtiban, “A new proposal for PCRR-based channel drop filter using elliptical rings,” *Phys. E Low-dimensional Syst. Nanostructures*, vol. 56, pp. 211–215, Feb. 2014, doi: 10.1016/j.physe.2013.07.018.
[102] H. Alipour-Banaei and F. Mehdizadeh, “Significant role of photonic crystal resonant cavities in WDM and DWDM communication tunable filters,” *Opt. - Int. J. Light Electron Opt.*, vol. 124, no. 17, pp. 2639–2644, Sep. 2013, doi: 10.1016/j.ijleo.2012.07.029.
[103] C.-W. Kuo, C.-F. Chang, M.-H. Chen, S.-Y. Chen, and Y.-D. Wu, “A new approach of planar multi-channel wavelength division multiplexing system using asymmetric super-cell photonic crystal structures,” *Opt. Express*, vol. 15, pp. 198–206, 2007, doi: 10.1364/OE.15.000198.
[104] U. P. Dharanipathy, M. Minkov, M. Tonin, V. Savona, and R. Houdré, “High-Q silicon photonic crystal cavity for enhanced optical nonlinearities,” *Appl. Phys. Lett.*, vol. 105, no. 10, p. 101101, 2014, doi: 10.1063/1.4894441.
[105] N. V. Triviño *et al.*, “Gallium nitride L3 photonic crystal cavities with an average quality factor of 16 900 in the near infrared,” *Appl. Phys. Lett.*, vol. 105, no. 23, p. 231119, 2014, doi: 10.1063/1.4903861.
[106] M. Minkov and V. Savona, “Automated optimization of photonic crystal slab cavities.,” *Sci. Rep.*, vol. 4, p. 5124, 2014, doi: 10.1038/srep05124.
[107] L. Jiang, H. Wu, W. Jia, and X. Li, “Optimization of low-loss and wide-band sharp photonic crystal waveguide bends using the genetic algorithm,” *Opt. - Int. J. Light Electron Opt.*, vol. 124, no. 14, pp. 1721–1725, Aug. 2013, doi: 10.1016/j.ijleo.2012.06.005.
[108] M. Djavid, S. A. Mirtaheri, and M. S. Abrishamian, “Photonic crystal notch-filter design using particle swarm optimization theory and finite-difference time-domain analysis,” *J. Opt. Soc. Am. B*, vol. 26, no. 4, pp. 849–853, 2009, doi: 10.1364/JOSAB.26.000849.
[109] S. Mirjalili, S. M. Mirjalili, and X. S. Yang, “Binary bat algorithm,” *Neural Comput. Appl.*, vol. 25, no. 3–4, pp. 663–681, 2014, doi: 10.1007/s00521-013-1525-5.
[110] M. Qiu, “Effective index method for heterostructure-slab-waveguide-based two-dimensional photonic crystals,” *Appl. Phys. Lett.*, vol. 81, no. 7, pp. 1163–1165, 2002, doi: 10.1063/1.1500774.
[111] S. A. Schulz, A. H. K. Park, I. De Leon, J. Upham, and R. W. Boyd, “Beyond the effective index method: improved accuracy for 2D simulations of photonic crystal waveguides,” *J. Opt.*, vol. 17, no. 7, p. 075006, 2015, doi: 10.1088/2040-8978/17/7/075006.
[112] M. Notomi, T. Tanabe, A. Shinya, E. Kuramochi, and H. Taniyama, “On-Chip All-Optical Switching and Memory by Silicon Photonic Crystal Nanocavities,” *Advances in Optical Technologies*, vol. 2008. pp. 1–10, 2008, doi: 10.1155/2008/568936.
[113] L. O’Faolain, T. P. White, D. O’Brien, X. Yuan, M. D. Settle, and T. F. Krauss, “Dependence of extrinsic loss on group velocity in photonic crystal waveguides.,” *Opt. Express*, vol. 15, no. 20, pp. 13129–13138, 2007, doi: 10.1364/OE.15.013129.
[114] P. A. Shields, M. D. B. Charlton, T. Lee, M. E. Zoorob, D. W. E. Allsopp, and W. N. Wang, “Enhanced Light Extraction by Photonic Quasi-Crystals in GaN Blue LEDs,” *IEEE J. Sel. Top. Quantum Electron.*, vol. 15, no. 4, pp. 1269–1274, 2009.
[115] X. Wu *et al.*, “Porous Light-Emitting Diodes With Patterned Sapphire Substrates Realized by High-Voltage Self-Growth and Soft UV Nanoimprint Processes,” *J. Light. Technol.*, vol. 32, no. 2, pp. 326–332, 2014, doi: 10.1109/jlt.2013.2293142.
[116] C. Wiesmann, K. Bergenek, N. Linder, and U. T. Schwarz, “Analysis of the emission

characteristics of photonic crystal LEDs," in *Proc. of SPIE, Photonic Crystal Materials and Devices VIII*, 2008, vol. 6989, pp. 69890L-69890L–9, doi: 10.1117/12.780572.
[117] H. Benisty, R. Stanley, and M. Mayer, "Method of source terms for dipole emission modification in modes of arbitrary planar structures," *J. Opt. Soc. Am. A*, vol. 15, no. 5, p. 1192, 2007, doi: 10.1364/josaa.15.001192.
[118] C. Wiesmann, "Nano-structured LEDs – Light Extraction Mechanisms and Applications," 2009.
[119] K. Deb, S. Agrawal, A. Pratap, and T. Meyarivan, "A fast elitist non-dominated sorting genetic algorithm for multi-objective optimization: NSGA-II," in *International Conference on Parallel Problem Solving From Nature*, 2000, pp. 849–858.
[120] C. A. C. Coello, G. B. Lamont, and D. A. Van Veldhuizen, *Evolutionary Algorithms for Solving Multi-Objective Problems*, vol. 5. Springer, 2007.
[121] M. S. Mohamed *et al.*, "Efficient continuous-wave nonlinear frequency conversion in high-Q gallium nitride photonic crystal cavities on silicon," *APL Photonics*, vol. 2, no. 3, p. 031301, 2017, doi: 10.1063/1.4974311.
[122] M. Minkov, V. Savona, and D. Gerace, "Photonic crystal slab cavity simultaneously optimized for ultra-high Q / v and vertical radiation coupling," *Appl. Phys. Lett.*, vol. 111, no. 13, p. 131104, 2017, doi: 10.1063/1.4991416.
[123] Y. Lai *et al.*, "Genetically designed L3 photonic crystal nanocavities with measured quality factor exceeding one million," *Appl. Phys. Lett.*, vol. 104, no. 24, p. 241101, 2014, doi: 10.1063/1.4882860.
[124] M. Minkov and V. Savona, "A compact, integrated silicon device for the generation of spectrally filtered, pair-correlated photons," *J. Opt.*, vol. 18, no. 5, p. 54012, 2016, doi: 10.1088/2040-8978/18/5/054012.
[125] N. V. Triviño *et al.*, "GaN L3 Photonic Crystal Cavities With an Average Quality Factor in Excess of 16000 in the Near Infrared," *2015 Conf. Lasers Electro-Optics*, vol. 1, no. 111, pp. 5–6, 2015, doi: 10.1364/CLEO_QELS.2015.FF1C.5.
[126] M. Minkov and V. Savona, "Automated Optimization of Photonic Crystals for Broadband Slow Light and Ultra-High-Q Cavities," *Front. Opt. Sci. 2015*, vol. 5124, no. 2014, p. 241101, 2015.
[127] M. Minkov and V. Savona, "Wide-band slow light in compact photonic crystal coupled-cavity waveguides," *Optica*, vol. 2, no. 7, pp. 631–634, 2015, doi: 10.1364/OPTICA.2.000631.
[128] E. A. Shcherbakov, V. V. Fomin, A. A. Abramov, A. A. Ferin, D. V. Mochalov, and V. P. Gapontsev, "Industrial grade 100 kW power CW fiber laser," *Opt. InfoBase Conf. Pap.*, 2013, doi: 10.1364/assl.2013.ath4a.2.
[129] Y. Tsuchida, K. Saitoh, and M. Koshiba, "Design of single-moded holey fibers with large-mode-area and low bending losses: the significance of the ring-core region," *Opt. Express*, vol. 15, no. 4, p. 1794, 2007, doi: 10.1364/oe.15.001794.
[130] M. I. Hasan, M. Selim Habib, M. Samiul Habib, and S. M. Abdur Razzak, "Highly nonlinear and highly birefringent dispersion compensating photonic crystal fiber," *Opt. Fiber Technol.*, vol. 20, no. 1, pp. 32–38, 2014, doi: 10.1016/j.yofte.2013.11.005.
[131] M. Y. Chen, Y. R. Li, J. Zhou, and Y. K. Zhang, "Design of asymmetric large-mode area optical fiber with low-bending loss," *J. Light. Technol.*, vol. 31, no. 3, pp. 476–481, 2013, doi: 10.1109/JLT.2012.2230245.
[132] G. Gu *et al.*, "Ytterbium-doped large-mode-area all-solid photonic bandgap fiber lasers," *Opt. Express*, vol. 22, no. 11, p. 13962, 2014, doi: 10.1364/oe.22.013962.

[133] T. S. Saini, A. Kumar, and R. K. Sinha, "Asymmetric large-mode-area photonic crystal fiber structure with effective single-mode operation: design and analysis," *Appl. Opt.*, vol. 55, no. 9, p. 2306, 2016, doi: 10.1364/ao.55.002306.
[134] C. Molardi, B. Sun, X. Yu, A. Cucinotta, and S. Selleri, "Polarization-Maintaining Large Mode Area Fiber Design for 2- μm Operation," *IEEE Photonics Technol. Lett.*, vol. 28, no. 22, pp. 2483–2486, 2016, doi: 10.1109/LPT.2016.2600572.
[135] L. Dong, X. Peng, and J. Li, "Leakage channel optical fibers with large effective area," *J. Opt. Soc. Am. B*, vol. 24, no. 8, p. 1689, 2007, doi: 10.1364/josab.24.001689.
[136] Xin Wang, Shuqin Lou, and Wenliang Lu, "Bending Orientation Insensitive Large Mode Area Photonic Crystal Fiber With Triangular Core," *IEEE Photonics J.*, vol. 5, no. 4, pp. 7100408–7100408, 2013, doi: 10.1109/jphot.2013.2271720.
[137] J. M. Fini, "Large mode area fiber design with asymmetric bend compensation," *Opt. InfoBase Conf. Pap.*, 2011, doi: 10.1364/oe.19.021866.
[138] M. J. Li *et al.*, "Limit of effective Area for single-mode operation in step-index large mode area laser fibers," *J. Light. Technol.*, vol. 27, no. 15, pp. 3010–3016, 2009, doi: 10.1109/JLT.2009.2020682.
[139] M. Kashiwagi, K. Saitoh, K. Takenaga, S. Tanigawa, S. Matsuo, and M. Fujimaki, "Effectively single-mode all-solid photonic bandgap fiber with large effective area and low bending loss for compact high-power all-fiber lasers," *Opt. Express*, vol. 20, no. 14, p. 15061, 2012, doi: 10.1364/oe.20.015061.
[140] J. Limpert *et al.*, "Extended single-mode photonic crystal fiber lasers," *Opt. Express*, vol. 14, no. 7, p. 2715, 2006, doi: 10.1364/oe.14.002715.
[141] X. Wang, S. Lou, and W. Lu, "Rectangle Lattice Large Mode Area Photonic Crystal Fiber for 2 μm Compact High-power Fiber Lasers," *IEEE J. Sel. Top. Quantum Electron.*, vol. 20, no. 5, 2014, doi: 10.1109/JSTQE.2014.2310707.
[142] S. Kabir, M. R. H. Khandokar, and M. A. G. Khan, "Design of triangular core LMA-PCF with low-bending loss and low non-linearity for laser application," *Opt. Laser Technol.*, vol. 81, pp. 84–89, 2016, doi: 10.1016/j.optlastec.2016.01.036.
[143] E. Coscelli *et al.*, "Analysis of the Modal Content Into Large-Mode-Area Photonic Crystal Fibers Under Heat Load," *IEEE J. Sel. Top. Quantum Electron.*, vol. 22, no. 2, 2016, doi: 10.1109/JSTQE.2015.2479156.
[144] K. Saitoh *et al.*, "Design of all-solid leakage channel fibers with large mode area and low bending loss," *Opt. Express*, vol. 17, no. 6, p. 4913, 2009, doi: 10.1364/oe.17.004913.
[145] M. Napierała, T. Nasiłowski, E. Bereś-Pawlik, F. Berghmans, J. Wójcik, and H. Thienpont, "Extremely large-mode-area photonic crystal fibre with low bending loss," *Opt. Express*, vol. 18, no. 15, p. 15408, 2010, doi: 10.1364/oe.18.015408.
[146] H. Bach and N. Neuroth, *The properties of optical glass*. Springer Science & Business Media, 1998.
[147] S. Kabir and S. M. A. Razzak, "An enhanced effective mode area fluorine doped octagonal photonic crystal fiber with extremely low loss," *Photonics Nanostructures - Fundam. Appl.*, vol. 30, pp. 1–6, 2018, doi: 10.1016/j.photonics.2018.02.002.
[148] S. L. Chuang, *Physics of Photonic Devices*. 2009.
[149] R. C. Gonzalez, R. E. Woods, and S. L. Eddins, *Digital image processing using MATLAB*. Pearson Education India, 2004.
[150] D. Ferrarini, L. Vincetti, M. Zoboli, A. Cucinotta, and S. Selleri, "Leakage properties of photonic crystal fibers," *Opt. Express*, vol. 10, no. 23, p. 1314, 2002, doi: 10.1364/oe.10.001314.

[151] R. Kotz *et al.*, “Three-Dimensional Printing of Transparent Fused silica glass,” *Nature*, vol. 544, 2017.
[152] M. Becker *et al.*, “Laser-drilled free-form silica fiber p-reforms for microstructured optical fibers,” *Opt. Fiber Technol.*, vol. 19, no. 5, pp. 482–485, 2013, doi: 10.1016/j.yofte.2013.06.001.
[153] S. Mazoyer *et al.*, “Statistical fluctuations of transmission in slow light photonic-crystal waveguides,” *Opt. Express*, vol. 18, no. 14, p. 14654, 2010, doi: 10.1364/oe.18.014654.
[154] C. Schulze *et al.*, “Mode resolved bend loss in few-mode optical fibers,” *Opt. Express*, vol. 21, no. 3, p. 3170, 2013, doi: 10.1364/oe.21.003170.
[155] J. H. Cole and R. T. Schermer, “Improved Bend Loss Formula Verified for Optical Fiber by Simulation and Experiment,” *IEEE J. Quantum Electron.*, vol. 43, no. 10, pp. 899–909, 2007.
[156] I. P. Giles, R. Chen, and V. Garcia-Munoz, “Fiber based multiplexing and demultiplexing devices for few mode fiber space division multiplexed communications,” in *OFC 2014*, 2014, pp. 1–3, doi: 10.1364/OFC.2014.Tu3D.1.
[157] J. A. Carpenter, B. J. Eggleton, and J. B. Schroeder, “LCOS Based Devices for Mode-division Multiplexing,” 2015, doi: 10.1364/OFC.2015.W1A.1.
[158] H. Qiu *et al.*, “Silicon mode multi/demultiplexer based on multimode grating-assisted couplers,” *Opt. Express*, vol. 21, no. 15, pp. 17904–17911, 2013, doi: 10.1364/OE.21.017904.
[159] J. Xing, Z. Li, X. Xiao, J. Yu, and Y. Yu, “Two-mode multiplexer and demultiplexer based on adiabatic couplers,” *Opt. Lett.*, vol. 38, no. 17, pp. 3468–3470, 2013, doi: 10.1364/OL.38.003468.
[160] K. Saitoh *et al.*, “PLC-based LP_11 mode rotator for mode-division multiplexing transmission,” *Opt. Express*, vol. 22, no. 16, p. 19117, Aug. 2014, doi: 10.1364/OE.22.019117.
[161] N. Hanzawa *et al.*, “Two-mode PLC-based mode multi/demultiplexer for mode and wavelength division multiplexed transmission,” *Opt. Express*, vol. 21, no. 22, pp. 25752–25760, 2013, doi: 10.1364/OE.21.025752.
[162] A. Li, X. Chen, A. Al Amin, J. Ye, and W. Shieh, “Space-Division Multiplexed High-Speed Superchannel Transmission Over Few-Mode Fiber,” *J. Light. Technol.*, vol. 30, no. 24, pp. 3953–3964, 2012, doi: 10.1109/JLT.2012.2206797.
[163] C. P. Tsekrekos and D. Syvridis, “All-Fiber Broadband ${\rm LP} _ {02} $ Mode Converter for Future Wavelength and Mode Division Multiplexing Systems,” *IEEE Photonics Technol. Lett.*, vol. 24, no. 18, pp. 1638–1641, 2012, doi: 10.1109/LPT.2012.2211585.
[164] D. Dai, “Silicon-based Multi-channel Mode (de)multiplexer for On-chip Optical Interconnects,” in *Advanced Photonics for Communications*, 2014, p. IM2A.2, doi: 10.1364/IPRSN.2014.IM2A.2.
[165] S. H. Chang *et al.*, “Mode division multiplexed optical transmission enabled by all–fiber mode multiplexer,” *Opt. Express*, vol. 22, no. 12, pp. 14229–14236, 2014, doi: 10.1364/OE.22.014229.
[166] D. Dai, Y. Tang, and J. E. Bowers, “Mode conversion in tapered submicron silicon ridge optical waveguides,” *Opt. Express*, vol. 20, no. 12, pp. 13425–13439, 2012, doi: 10.1364/OE.20.013425.
[167] M. Skorobogatiy *et al.*, “Quantitative characterization of higher-order mode converters in weakly multimoded fibers,” *Opt. Express*, vol. 11, no. 22, pp. 2838–2847, 2003, doi:

10.1364/OE.11.002838.
[168] H. Mellah, J.-P. Bérubé, R. Vallée, and X. Zhang, “Fabrication of a LP01 to LP02 mode converter embedded in bulk glass using femtosecond direct inscription,” *Opt. Commun.*, vol. 410, pp. 475–478, Mar. 2018, doi: 10.1016/J.OPTCOM.2017.10.054.
[169] H. Mellah, X. Zhang, and D. Shen, “Analysis of optical fiber-based LP01<--> LP02 mode converters for the O-, S-, and C-Band,” *Appl. Opt.*, vol. 54, no. 17, pp. 5568–5575, 2015, doi: 10.1364/AO.54.005568.
[170] H. Mellah, X. Zhang, and D. Shen, “LP01 to LP0m mode converters using all-fiber two-stage tapers,” *Opt. Commun.*, vol. 354, 2015, doi: 10.1016/j.optcom.2015.05.066.
[171] Y. N. Zhang, Y. Zhao, and R. Q. Lv, “A review for optical sensors based on photonic crystal cavities,” *Sensors Actuators, A Phys.*, vol. 233, pp. 374–389, 2015, doi: 10.1016/j.sna.2015.07.025.
[172] M. Youcef Mahmoud, G. Bassou, and A. Taalbi, “A new optical add–drop filter based on two-dimensional photonic crystal ring resonator,” *Opt. - Int. J. Light Electron Opt.*, vol. 124, no. 17, pp. 2864–2867, 2013, doi: 10.1016/j.ijleo.2012.08.072.
[173] Y. Liu and H. W. M. Salemink, “Sensitive All-Optical Channel-Drop Sensor in Photonic Crystals,” *J. Light. Technol.*, vol. 33, no. 17, pp. 3672–3678, 2015, doi: 10.1109/JLT.2015.2450995.
[174] Y. Liu and H. W. M. Salemink, “Photonic crystal-based all-optical on-chip sensor,” *Opt. Express*, vol. 20, no. 18, p. 19912, Aug. 2012, doi: 10.1364/OE.20.019912.
[175] S. Guo and S. Albin, “Simple plane wave implementation for photonic crystal calculations,” *Opt. Express*, vol. 11, no. 2, pp. 167–175, Jan. 2003, doi: 10.1364/OE.11.000167.
[176] A. Säynätjoki, M. Mulot, J. Ahopelto, and H. Lipsanen, “Dispersion engineering of photonic crystal waveguides with ring-shaped holes,” *Opt. Express*, vol. 15, no. 13, pp. 8323–8328, Jun. 2007, doi: 10.1364/OE.15.008323.